

# RCA REVIEW

*a technical journal*

RADIO AND ELECTRONICS  
RESEARCH • ENGINEERING

---

*Published quarterly by*

RCA LABORATORIES

*in cooperation with all subsidiaries and divisions of*  
RADIO CORPORATION OF AMERICA

---

---

VOLUME XXI

DECEMBER 1960

NUMBER 4

---

## CONTENTS

	PAGE
Amplification—Modern Trends, Techniques and Problems .....	485
L. S. NERGAARD	
The Ultra-High-Vacuum System for the C-Stellarator .....	508
K. DREYER AND J. T. MARK	
High-Frequency Varactor Diodes .....	547
C. W. MUELLER AND R. D. GOLD	
A Plug-Type Image Orthicon Target .....	558
S. A. OCHS	
Time-Averaged Effects on Charged Particles in A-C Fields .....	570
T. W. JOHNSTON	
RCA TECHNICAL PAPERS .....	611
AUTHORS .....	614
INDEX, VOLUME XXI (1960) .....	616

---

© 1961 by Radio Corporation of America

*All rights reserved*

---

RCA REVIEW is regularly abstracted and indexed by *Industrial Arts Index*, *Science Abstracts* (I.E.E.-Brit.), *Electronic Engineering Master Index*, *Chemical Abstracts*, *Proc. I.R.E.*, and *Electronic & Radio Engineer.*

# RCA REVIEW

---

## BOARD OF EDITORS

### *Chairman*

R. S. HOLMES  
*RCA Laboratories*

E. I. ANDERSON  
*RCA Victor Home Instruments*

A. A. BARCO  
*RCA Laboratories*

G. L. BEERS  
*Radio Corporation of America*

G. H. BROWN  
*Radio Corporation of America*

I. F. BYRNES  
*Industrial Electronic Products*

A. L. CONRAD  
*RCA Service Company*

E. W. ENGSTROM  
*Radio Corporation of America*

D. H. EWING  
*Radio Corporation of America*

A. N. GOLDSMITH  
*Consulting Engineer, RCA*

A. L. HAMMERSCHMIDT  
*National Broadcasting Company, Inc.*

J. HILLIER  
*RCA Laboratories*

E. A. LAPORT  
*Radio Corporation of America*

H. W. LEVERENZ  
*RCA Laboratories*

G. F. MAEDEL  
*RCA Institutes, Inc.*

W. C. MORRISON  
*Industrial Electronic Products*

H. F. OLSON  
*RCA Laboratories*

R. W. PETER  
*RCA Laboratories*

D. S. RAU  
*RCA Communications, Inc.*

D. F. SCHMIT  
*Radio Corporation of America*

G. R. SHAW  
*Electron Tube Division*

L. A. SHOTLIFF  
*RCA International Division*

S. STERNBERG  
*Astro-Electronics Division*

W. M. WEBSTER  
*RCA Laboratories*

I. WOLFF  
*Radio Corporation of America*

### *Secretary*

C. C. FOSTER  
*RCA Laboratories*

---

## REPLICATION AND TRANSLATION

Original papers published herein may be referenced or abstracted without further authorization provided proper notation concerning authors and source is included. All rights of republication, including translation into foreign languages, are reserved by RCA Review. Requests for republication and translation privileges should be addressed to *The Manager*.

# AMPLIFICATION—MODERN TRENDS, TECHNIQUES AND PROBLEMS\*

By

L. S. NERGAARD

RCA Laboratories,  
Princeton, N. J.

*Summary*—This paper reviews the characteristics of various types of small-signal amplifiers. These include traveling-wave tubes, tunnel diodes, cooled and uncooled parametric amplifiers, and masers. The type of amplifier best suited for a particular application is determined by a number of factors, among which noise considerations and frequency are the most important. Areas of usefulness for each type of amplifier are described.

In addition, there is a brief discussion of existing high-power transmitting tubes and their fundamental power limitations. It is suggested that a major breakthrough may be necessary before an order-of-magnitude improvement can be expected.

## INTRODUCTION

THE PAST FEW YEARS have seen the advent of a number of new amplifiers, many of them using solid-state phenomena to achieve remarkably low noise figures at microwave frequencies. These new amplifiers have been described in detail in the literature. This paper is in the nature of an over-all survey; it describes the new amplifiers in rather general terms, discusses their bandwidth, gain, and noise figure, compares them to put them in context, and then hazards a guess at their future role in communications.

During these same past few years, the power output of transmitting tubes has increased remarkably. This increase in power output is not the result of major innovation, as is the achievement of lower-noise-figure amplifiers, but is the result of refinement spurred by new demands for power at microwave frequencies. Because transmitting tubes are as important to communications as are low-noise amplifiers, their limitations are reviewed briefly and the present state of the art outlined. Finally, future prospects for transmitting tubes are discussed briefly.

## GAIN MECHANISMS

The achievement of power gain in any device requires some mechanism by which energy is added to the signal in a coherent manner.

---

\* Manuscript received 3 November 1960.

In all of the amplifiers discussed here, this mechanism is electronic. In the case of vacuum tubes, the electrons are "free" and move unimpeded by collisions from the electron-emitting cathode to the collector. In masers, the electrons are fixed in position and only their magnetic properties are involved in the gain mechanism. In semiconductor devices, although the electrons do move, they suffer collisions at the rate of about  $10^{12}$  per second so they have a short memory of what has gone on before. Yet in every case gain is possible.

### *Vacuum Tubes*

Consider vacuum tubes first. In vacuum tubes, the signal is impressed on an electron stream moving with a d-c velocity which may vary from point to point, as in grid-controlled tubes, or may be uniform in the interaction region, as in klystrons and traveling-wave tubes. The signal may be impressed on the stream in the form of density modulation or velocity modulation. In the latter case, fast electrons tend to overtake slower electrons so that bunches form and the stream becomes density modulated. The density modulation is tantamount to an a-c current at signal frequency. This a-c current interacts with a circuit of some kind to depress the potential below the d-c potential, the electrons are "decelerated" to a velocity less than that corresponding to the d-c velocity, and the energy lost is imparted to the circuit. Thus, part of the d-c energy of the electron stream is converted to a-c energy in the form of an enhanced signal.

How this mechanism proceeds in the case of the traveling-wave tube<sup>1</sup> is illustrated in Figure 1. The tube consists of an electron gun which launches the electron beam, a helix with input and output couplers, and an electron collector. When a signal is impressed on the helix at the input end, it propagates towards the output end and in so doing velocity modulates the electron beam. The pitch of the helix is chosen to make the velocity of propagation just a little less than the velocity of the beam. As the beam drifts, the velocity modulation is converted to density modulation. Because bunches move just a little faster than the wave on the helix, they tend to collect in those parts of the field pattern of the propagating wave where they are decelerated. The deceleration enhances the bunching and at the same time adds energy to the wave on the helix in a coherent manner, so that the helix voltage increases as shown in the center of Figure 1. The result is an amplified signal at the output end of the helix. The

---

<sup>1</sup> For a definitive discussion of traveling-wave tubes, see J. R. Pierce, *Traveling-Wave Tubes*, D. Van Nostrand Co., New York, N. Y., 1950.

behavior of the traveling-wave tube can be represented by the equivalent circuit at the bottom of Figure 1. The helix is represented by a transmission line having a loss resistance  $r$ , a series inductance  $L$ , and a shunt capacitance  $C$ , all per unit length. The electron interaction is represented by a negative conductance  $-G$  per unit length, which, if it is large enough, over-rides the resistance of the helix and gives gain. If

$$\frac{r}{\omega L} \ll 1$$

and

$$\frac{G}{\omega C} \ll 1,$$

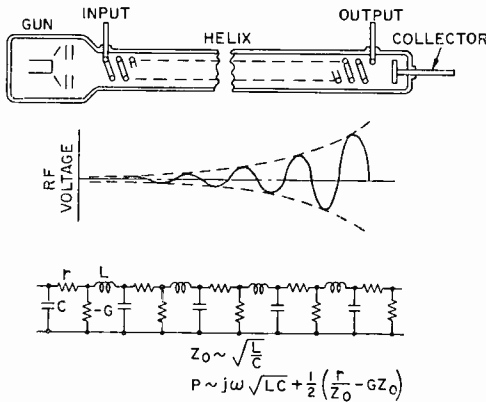


Fig. 1—Operation of the traveling-wave tube.

where  $\omega$  is the operating frequency, then the surge impedance of the transmission line is

$$Z_0 \sim \sqrt{\frac{L}{C}}, \tag{1}$$

and the propagation constant is

$$P \sim j\omega \sqrt{LC} + \frac{1}{2} \left[ \frac{r}{Z_0} - G Z_0 \right]. \tag{2}$$

Hence, a wave traveling down the transmission line grows at a rate of

$$\frac{1}{2} \left( GZ_0 - \frac{r}{Z_0} \right) \quad (3)$$

per unit length.

All of this is well-known, but it is worthwhile to review the argument to set the stage for other traveling-wave amplifiers, namely, traveling-wave masers and traveling-wave tunnel-diode and parametric amplifiers.

### Masers

As noted earlier, there is no electron motion in the maser<sup>2</sup> and these amplifiers depend on the magnetic properties of electrons. Every electron may be thought of as moving with the velocity of light in a very small circle with a radius of about  $10^{-12}$  cm. The current

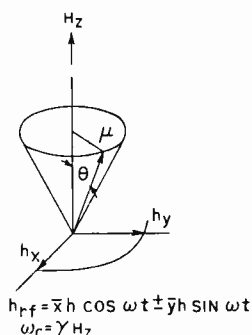


Fig. 2—Precession of an electron spin  $\mu$  about a polarizing field  $H_z$ .

of the circling electron gives it a dipole moment of about  $10^{-20}$  erg per gauss. Furthermore, the circling motion makes the electron act as a little gyroscope with an angular momentum of about  $10^{-28}$  erg second. These properties of an electron are usually referred to as the "spin."

Now consider the behavior of the electron spin in a magnetic field. Figure 2 shows an electron spin, represented by the vector  $\mu$  oriented at an angle  $\theta$  with respect to an aligning steady magnetic field  $H_z$ . The magnetic field exerts a torque on the spin, and the spin, like a gyroscope, precesses about the Z-axis with an angular frequency

<sup>2</sup> For a comprehensive discussion of masers, see J. Weber, "Masers," *Rev. Mod. Phys.*, Vol. 31, No. 3, p. 681, July 1959.

$$\omega_0 = \gamma H_z$$

where  $\gamma$  is the ratio of the magnetic dipole moment to the spin angular momentum. If a circularly polarized r-f magnetic field, such as represented by  $\mathbf{h}_{r,f} = \bar{x} h \cos \omega t \pm \bar{y} \sin \omega t$  in the figure is impressed on the spin, and if the rotation of the field is synchronous with the precession of the spin, the spin will absorb energy and the angle  $\theta$  will increase. If the direction of rotation of the field is reversed, the field will have no effect on the spin. This nonreciprocal behavior is used to make such microwave devices as ferrite isolators and circulators. It is also used to prevent backward propagation in traveling-wave amplifiers.

While the simple mechanical picture of spin presented above says nothing about possible orientation angles,  $\theta$ , of the spin, quantum mechanics does, and limits the spin orientations to specific values,

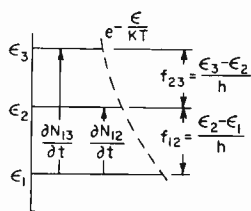


Fig. 3—Equilibrium occupancy and transitions between the energy states of a set of spins.

each characterized by a specific energy. The permitted energy levels may be represented as shown in Figure 3. To change the spin from a lower to a higher energy level requires an excitation at a frequency equal to the energy difference divided by Planck's constant. Conversely, if a spin drops from a higher to a lower level, radiation is emitted at a frequency equal to the energy difference divided by Planck's constant. When no excitation is present, an assembly of spins will, in the course of time, distribute itself among the possible levels according to the Boltzmann law. This distribution is indicated by the lengths of the horizontal lines labelled  $\epsilon_1$ ,  $\epsilon_2$  and  $\epsilon_3$  in Figure 3. Now consider the rate of exchange of spins between levels when excitation is present. As in Figure 3, let  $\partial N_{12}/\partial t$  be the net rate of loss of spins of level 1 to level 2, and  $\partial N_{13}/\partial t$  be the rate of loss to level 3. If the situation is stable, the net loss by level 1 must be zero. Therefore

$$\frac{\partial N_{12}}{\partial t} + \frac{\partial N_{13}}{\partial t} = 0. \quad (4)$$

Now, if each term in Equation (4) is multiplied by Planck's constant times the frequency corresponding to the transition and divided by the frequency to maintain the equality,

$$\frac{hf_{12}}{f_{12}} \frac{\partial N_{12}}{\partial t} + \frac{hf_{13}}{f_{13}} \frac{\partial N_{13}}{\partial t} = 0.$$

But

$$hf_{12} \frac{\partial N_{12}}{\partial t} = P_{12},$$

where  $P_{12}$  is the rate of transport of energy from level 1 to level 2. Similarly

$$hf_{13} \frac{\partial N_{13}}{\partial t} = P_{13}.$$

Hence

$$\frac{P_{12}}{f_{12}} + \frac{P_{13}}{f_{13}} = 0. \quad (5)$$

A similar equation can be written for transitions from level 2;

$$\frac{P_{21}}{f_{12}} + \frac{P_{23}}{f_{23}} = 0. \quad (6)$$

Note that an exchange of subscripts on the power requires a change of sign of the power. Equations (5) and (6) may be written

$$P_{12} = - \frac{f_{12}}{f_{13}} P_{13}, \quad (7)$$

$$P_{23} = - \frac{f_{23}}{f_{13}} P_{13}. \quad (8)$$

Thus, if power is applied (pumped) to cause transitions from level 1 to level 3, the power output available in the other transitions is equal to the ratio of the output frequency to the pump frequency times the pump power. If power is extracted at frequency  $f_{12}$ , the other fre-

quency,  $f_{23}$ , is called the idler frequency, and vice versa. These power relations are known as the Manley-Rowe relations and were originally derived in a consideration of energy transformations by nonlinear reactances.<sup>3,4</sup> They apply equally to masers and parametric amplifiers.

The means of obtaining maser amplification are now obvious. One takes a crystal such as ruby or rutile and dopes it with paramagnetic ions such as chromium three-plus ( $\text{Cr}^{+++}$ ) to obtain a high density of spins and thus, hopefully, a large gain-bandwidth product. A pump signal at a frequency  $f_{13}$  (as in Figure 3) is applied to pump spins from level 1 into level 3, and the output power is then removed at either frequency  $f_{23}$  or  $f_{12}$ . There are, however, a few details to be taken care of before maser action is obtained. The Manley-Rowe relations tell what power outputs are theoretically possible but do not tell how to obtain them. First, something must cause transitions in order to get the power out. It is true that there are spontaneous transitions, but these are few in number at microwave frequencies. Moreover, they are random and give rise to noise, not to a useful signal. Two things induce transitions. The first is spin-lattice relaxation. The spins in excited states in a crystal "collide" with the crystal lattice and drop to lower energy levels. This relaxation process removes spins from excited states so rapidly at ordinary temperatures that it is impossible to maintain an over-population in the excited states. In masers, therefore, the crystals are cooled to liquid helium temperature where the excitation lifetimes become so long (of the order of milliseconds) that an over-population of the excited states can be maintained with a reasonable pump power.

When the spin-lattice relaxation time is long, a second cause of transitions that can be exploited is r-f excitation. An r-f signal triggers transitions and the energy released is added coherently to the signal. In effect, the maser behaves as a negative resistance.

### *Parametric Amplifiers*

Parametric amplifiers, as the name implies, operate by virtue of a varying circuit parameter.<sup>5-7</sup> It is easily shown that to achieve gain

<sup>3</sup> J. M. Manley and H. E. Rowe, "Some General Properties of Nonlinear Elements," *Proc. I.R.E.*, Vol. 44, p. 904, July 1956.

<sup>4</sup> M. T. Weiss, "Quantum Derivation of Energy Relations Analogous to Those for Nonlinear Reactances," *Proc. I.R.E.*, Vol. 45, p. 1012, July 1954.

<sup>5</sup> A. van der Ziel, "On the Mixing Properties of Nonlinear Capacitances," *Jour. Appl. Phys.*, Vol. 19, p. 999, November 1948.

<sup>6</sup> S. Bloom and K. K. N. Chang, "Theory of Parametric Amplification Using Nonlinear Reactances," *RCA Review*, Vol. 18, p. 578, Dec. 1957.

<sup>7</sup> L. S. Nergaard, "Nonlinear-Capacitance Amplifiers," *RCA Review*, Vol. 20, p. 3, March 1959.

the parameter that must be varied is a reactance, i.e., a circuit element that stores energy. Storage elements which have been used to achieve parametric amplification are electron spins (in ferrites), the junction capacitances of semiconductor diodes, and electron beams. While parametric amplification has been achieved with ferrites, the pumping power required has been very large, so that at the moment, ferrite amplifiers are not practical at microwave frequencies. Hence, these amplifiers are not discussed in this paper.

The general scheme of parametric amplifiers is shown in Figure 4. The network consists of three circuits, the first tuned to the signal frequency, the second tuned to the pump frequency and driven by a

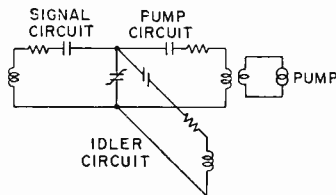


Fig. 4—Basic circuit of a parametric amplifier.

local oscillator, and the third tuned to the sum of, or difference between, the pump and signal frequencies, with all three coupled by a nonlinear reactance. The third circuit is known as the idler circuit. The general method of obtaining amplification is as follows. The signal voltage beats with the local oscillator voltage in the nonlinear reactance to produce a current at idler frequency. The current at idler frequency excites the idler circuit to produce a voltage which beats with the local oscillator voltage in the nonlinear reactance to produce a current at signal frequency. This current excites the signal circuit and produces a voltage which adds to the original signal voltage and, thus, produces amplification. Again, the amplifier presents an effective negative resistance to the signal. The power delivered by the negative resistance comes from the local oscillator or pump, of course, and the amount of power available is given by the Manley-Rowe relations, as previously discussed. Because the active element in parametric amplifiers is a reactance, it displays no Johnson noise and, hence, provides low-noise amplification.

The simplest parametric amplifiers use semiconductor diodes as nonlinear reactors. The current-voltage characteristic and capacitance-voltage characteristic of such a diode are shown in Figure 5. In the forward direction, the current rises very rapidly with voltage; in the

backward direction, it saturates and remains almost constant until avalanche conduction sets in. Hence, when the diode is biased in the backward direction, it presents a very high shunt resistance to any circuit to which it is connected. Unfortunately, the shunt resistance is not the only resistance the diode presents to the circuit. There is also a series resistance. This series resistance,  $r_{\text{series}}$ , in connection with the capacitance of the diode, determines the diode  $Q$  ( $= 1/(\omega Cr_{\text{series}})$ ) and sets an upper limit on the frequency at which the diode is useful.

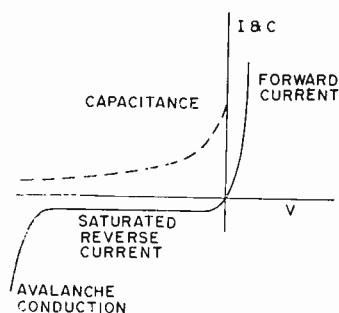


Fig. 5—Parametric diode characteristics.

In the backward direction, the capacitance varies approximately inversely with the square root of the applied voltage. This voltage-dependent capacitance serves admirably as the nonlinear reactance in microwave amplifiers.

There has been a considerable amount of work on electron beams as nonlinear reactances.<sup>8</sup> Parametric amplifiers using the longitudinal space-charge waves employed in ordinary traveling-wave tubes have failed to yield low noise figures. The catch seems to be that the nonlinearity in the beam produces many idler frequencies all of which are supported by the beam. The noise in the beam at the idler frequencies interact with the pump voltage to produce noise at the signal frequency. The result is a noisy amplifier. As yet, no means of suppressing unwanted idler signal responses in the electron beam have been found. It is not so simple as omitting additional idler circuits in Figure 4.

While parametric amplifier tubes using longitudinal waves on electron beams have not been successful in giving low-noise amplification, a tube using transverse waves has been eminently successful.

<sup>8</sup> A. Ashkin, "Parametric Amplification of Space-Charge Waves," *Jour. Appl. Phys.*, Vol. 29, p. 1646, Dec. 1958.

This tube, the Adler tube, is shown schematically in Figure 6.<sup>9,10</sup> The tube consists of (reading from left to right in Figure 6) (1) an electron gun which launches the beam, (2) a pair of deflection plates which (in the presence of a magnetic field  $H$  of a magnitude to make the cyclotron frequency,  $\omega_c$ , of the electrons approximately equal to the signal frequency) impart a spiral motion to the electrons, (3) a set of quadrupole electrodes driven in pairs at twice the cyclotron frequency, (4) a pair of output deflection plates which absorb energy from the spiral motion of the electrons and deliver the energy to the output circuit, and (5) the electron-beam collector. When the electron beam enters the region between input deflection plates, it carries noise in its transverse motion because of the thermal velocity distribution of the electrons in the beam. The length of the deflection plates and the loading of the input circuit are chosen to completely absorb the transverse noise on the beam at the same time the signal is impressed.

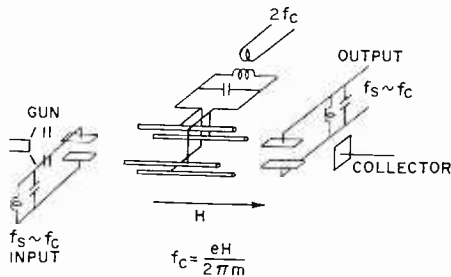


Fig. 6—Schematic diagram of the Adler Tube.

Thus, the beam is noise free when it emerges from the deflection plates and carries only the signal in the form of a spiral motion of the electrons. The radius of the spiral motion is proportional to the signal amplitude. When the beam enters the quadrupole region, it sees a tangential electric field which is zero on the axis and increases with increasing displacement from the axis. Furthermore, the tangential field in effect rotates in synchronism with the electrons. Thus, each electron which enters in proper pump phase is accelerated in proportion to its displacement from the axis (the electrons which enter in improper phase are decelerated and end up on the axis of the tube). Because of the magnetic field, the electron continues to spiral at the

<sup>9</sup> R. Adler, "Parametric Amplification of the Fast Electron Wave," *Proc. I.R.E.*, Vol. 46, p. 1300, June, 1958.

<sup>10</sup> R. Adler, G. Hrbek, and G. Wade, "The Quadrupole Tube Amplifier, a Low-Noise Parametric Device," *Proc. I.R.E.*, p. 1713, October, 1959.

AUTHORS, VOLUME XXI	ISSUE PAGE
Holt, F. R. (Coauthor)—“A Compatible Stereophonic System for the AM Broadcast Band” .....	Sept. 299
Honig, R. E. (Coauthor)—“Vapor Pressure Data for Some Common Gases” .....	Sept. 360
Hook, H. O. (Coauthor)—“Vapor Pressure Data for Some Common Gases” .....	Sept. 360
Johnston, T. W.—“Time-Averaged Effects on Charged Particles in A-C Fields” .....	Dec. 570
Kennedy, R.—“Sine-Squared Pulses in Television System Analysis” .....	June 253
Kihn, H. (Coauthor)—“Microminiature Multichannel Pulse-Position-Modulation System Incorporating Transistor-Magnetic-Core Circuitry” .....	June 199
Klensch, R. J. (Coauthor)—“Microminiature Multichannel Pulse-Position-Modulation System Incorporating Transistor-Magnetic-Core Circuitry” .....	June 199
Knight, M. B.—“A New Miniature Beam-Deflection Tube” ..	June 266
Komlos, S. G. (Coauthor)—“Theoretical and Experimental Study of Wide-Band Paraboloid Antenna with Central-Reflector Feed” .....	Mar. 94
Laport, E. A. (Coauthor)—“Improved Antennas of the Rhombic Class” .....	Mar. 117
Larrabee, R. D.—“Measurement of Semiconductor Properties through Microwave Absorption” .....	Mar. 124
Mark, J. T. (Coauthor)—“The Ultra-High-Vacuum System for the C-Stellarator” .....	Dec. 508
Morgan, J. M. (Coauthor)—“The Stratoscope I Television System” .....	June 151
Mueller, C. W. (Coauthor)—“High-Frequency Varactor Diodes” .....	Dec. 547
Murakami, T.—“Ringing in Horizontal-Deflection and High-Voltage Television Circuits” .....	Mar. 17
Nergaard, L. S.—“Amplification—Modern Trends, Techniques and Problems” .....	Dec. 485
Ochs, S. A.—“A Plug-Type Image Orthicon Target” .....	Dec. 558
O'Connell, J. H. (Coauthor)—“A Compatible Stereophonic System for the AM Broadcast Band” .....	Sept. 299
Paschke, F.—“Nonlinear Theory of a Velocity-Modulated Electron Beam with Finite Diameter” .....	Mar. 53
Pike, W. S. (Coauthor)—“The Stratoscope I Television System” .....	June 151
Preisig, J. O. (Coauthor)—“A Compatible Stereophonic System for the AM Broadcast Band” .....	Sept. 299
Rhodes, R. N. (Coauthor)—“A Compatible Stereophonic System for the AM Broadcast Band” .....	Sept. 299
Schindler, M. J.—“The Magnetic Field and Flux Distributions in a Periodic Focusing Stack for Traveling-Wave Tubes” ..	Sept. 414
Simon, A. H. (Coauthor)—“Microminiature Multi-channel Pulse-Position-Modulation System Incorporating Transistor-Magnetic-Core Circuitry” .....	June 199
Stocker, C. F. (Coauthor)—“The Design of Varactor Diodes” ..	Sept. 457
Veldhuis, A. C. (Coauthor)—“Improved Antennas of the Rhombic Class” .....	Mar. 117
Veloric, H. S. (Coauthor)—“Evaluation and Control of Diffused Impurity Layers in Germanium” .....	Sept. 437
Wolkstein, H. J.—“Design Considerations for Grid-Controlled Electron Guns for Pulsed Traveling-Wave Tubes” .....	Sept. 389



cyclotron frequency, but moves to a larger radius as a result of the acceleration. Thus, each electron leaves the quadrupole field with its radius of spiral motion increased in proportion to the signal it carried when it entered the region. The added energy may be extracted at the output coupler thus yielding an amplified signal. The fact that noise on the beam was removed by the input coupler makes the tube a low-noise amplifier. The Adler tube has many attractive features in addition to its low-noise performance, and these are mentioned in the next section.

### *Tunnel Diode*

In all the devices thus far discussed, the gain mechanism has been reduced to an equivalent negative conductance. It is fitting to conclude, therefore, with the tunnel diode, not only because it is the most recent in point of development, but also because it displays a negative conductance at first hand.<sup>11</sup> To discuss the mechanism by which the

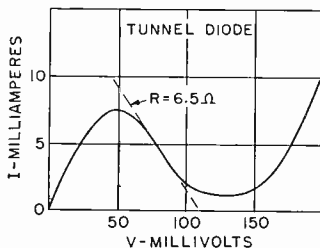


Fig. 7—Tunnel-diode characteristic.

tunnel diode achieves a negative conductance would be to wander a little far afield. Therefore, it will have to suffice to note that its current-voltage characteristic is typically as shown in Figure 7. The current rises rapidly with voltage in the forward direction, reaches a maximum at about 50 millivolts, decreases to a minimum, and then rises again. In the region between 50 and 100 millivolts, roughly, the diode displays a negative conductance. This negative conductance can be realized at a low average current. Because the noise in the tunnel diode is due to shot effect, the low average current means a low noise output from the diode.

<sup>11</sup> K. K. N. Chang, "Low-Noise Tunnel-Diode Amplifier," *Proc I.R.E.*, Vol. 47, p. 1268, July, 1959.

## LOW-NOISE AMPLIFIERS

All of the low-noise amplifiers to be considered fall into one or the other of two broad categories, "lumped-circuit" amplifiers and traveling-wave amplifiers. In the lumped-circuit amplifiers, resonant cavities are used to provide selectivity, to separate various frequency components in parametric amplifiers, and to effect impedance transformations. A typical lumped-circuit negative-conductance amplifier is shown in Figure 8. This schematic drawing may be used to represent a maser, a parametric amplifier, or a tunnel-diode amplifier. In the

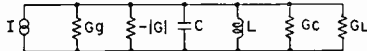


Fig. 8—Basic circuit of a negative-resistance amplifier.

case of a maser, the negative conductance  $-|G|$  is produced by the spins, and the capacitance  $C$  includes a contribution from the spins. In the case of the parametric amplifier, the negative conductance arises from the "mixing" of pump power with the signal via the idler circuit. Thus  $-|G|$  depends on the pump power and the idler-circuit load. Because the idler circuit stores energy, it also contributes to the capacitance  $C$ ; in fact, in many cases the idler contribution to  $C$  dominates and determines that bandwidth of the amplifier. In the case of the tunnel diode,  $-|G|$  is just the negative conductance of the diode, and  $C$ , ideally, is just the capacitance of the diode. In every case,  $G_g$  is the source conductance,  $G_L$  the load conductance,  $G_c$  the loading due to circuit loss (including the crystal loss in the case of the maser and the diode loss in the case of diode amplifiers), and  $L$  is the inductance required to tune out the capacitance  $C$  at the signal frequency. In the ideal diode-amplifier circuit,  $G_c$  would be just the diode loss conductance and  $C$  the diode capacitance, and the ultimate circuit performance would be determined by the  $Q$  of the diode.

The power gain of the amplifier is

$$\beta = \frac{4G_L G_g}{[G_g - |G| + G_L + G_C]^2}, \quad (9)$$

and the bandwidth is

$$\Delta\omega = \frac{G_g - |G| + G_L + G_C}{C}. \quad (10)$$

Hence, the voltage-gain-bandwidth product is

$$\sqrt{\beta}\Delta\omega = \frac{2\sqrt{G_L G_g}}{C}. \quad (11)$$

It is easily shown that  $(\sqrt{\beta}-1)\Delta\omega C$  cannot exceed the magnitude of the negative conductance minus the circuit loss ( $|G| - G_c$ ). Hence, the available negative conductance and the circuit loss limit the gain-bandwidth product. The noise figure of the amplifier is

$$F = 1 + \frac{T}{T_0} \left( \frac{G_L + G_c + G_N}{G_g} \right) \quad (12)$$

where  $T_0$  is the reference temperature of the noise source,  $T$  is the ambient temperature, and  $G_N$  is the noise conductance of the negative conductance. An obvious method for reducing the noise factor is to increase the source conductance  $G_g$ . The increase in  $G_g$  usually entails a decrease in the available gain-bandwidth product. If the bandwidth is fixed by systems requirements, the decrease in noise factor requires a sacrifice of gain.

The noise factor of the various amplifiers will now be considered in turn.

**The Maser**—In the maser, noise is determined principally by the idler transitions. They contribute an approximate noise conductance of

$$G_N = \frac{\omega_s}{\omega_t} |G|,$$

where  $\omega_s$  is the signal frequency,  $\omega_t$  is the idler frequency, and  $|G|$  is the magnitude of the negative conductance. Because masers are operated at very low temperatures, approximately 4°K, their noise factor is correspondingly low.

**Parametric Amplifiers**—In parametric amplifiers, the principal source of noise is the idler circuit. Hence, the noise conductance is the same as for masers, namely,

$$G_N = \frac{\omega_s}{\omega_t} |G|.$$

Thus, the noise factor may be reduced by making the idler frequency

high compared to the signal frequency. As in the maser, it is also possible to reduce the noise factor by cooling the idler circuit so that its Johnson noise is low. When this is done, a very low noise factor is obtained.

**The Tunnel Diode**—As noted earlier, the noise in the tunnel diode is due to shot effect. Thus,

$$G_N \sim \frac{eI_0}{2kT}, \quad (14)$$

where  $I_0$  is the d-c current. With diodes operating at 1 milliamperes or less, the diode usually makes a negligible contribution to the noise factor.

All of the amplifiers discussed above have several unfortunate limitations:

1. The input and output circuits are common. Thus, noise originating in the following stage can reach the amplifier and return to the following stage in amplified form. This difficulty may be avoided by interposing an isolator or circulator between the amplifier and the following stage. It would be a happier state of affairs, however, if no isolation were required.
2. The gain-bandwidth product is usually uncomfortably small when the compromises necessary to the achievement of a low noise figure are made.
3. When the gain is increased, the amplifier tends toward instability, and any slight drift in bias, pump power, or mismatch may result in oscillation.

Some of the difficulties discussed above are circumvented in the parametric up-converter.<sup>12,13</sup> In the up-converter, the idler frequency is made higher than the signal frequency, and the output is taken from the idler circuit. The ratio of signal-to-idler frequency is then favorable for a low noise factor, the input and output are separate, and the circuit is stable. However, as the signal frequency is pushed to higher and higher frequencies, the pump frequency, which conventionally lies above the idler frequency, may get uncomfortably

<sup>12</sup> G. F. Hermann, M. Uenohara, and A. Uhler, Jr., "Noise Figure Measurements on Two Types of Variable Reactance Amplifiers Using Semiconductor Diodes," *Proc. I.R.E.*, Vol. 46, p. 1301, June, 1958.

<sup>13</sup> B. Salzberg and E. W. Sard, "A Low-Noise, Wide-Band Reactance Amplifier," *Proc. I.R.E.*, Vol. 46, p. 1303, June, 1958.

high. A possible solution is the use of higher-order nonlinearities of a diode capacitance characteristic to achieve lower-frequency pumping. This scheme has been demonstrated by Chang and Bloom.<sup>14</sup>

The tunnel diode may be used as a down-converter by providing a local oscillator.<sup>15,16</sup> Because the noise of the diode is shot effect and no frequency ratios are involved in the noise factor during the conversion process, a low-noise tunnel diode is quite feasible and, as in the case of the parametric up-converter, the input and output circuits are separated. However, it is sensitive to output load.

None of these artifices increase the gain-bandwidth product. All of these negative-conductance amplifiers start with a circuit having a passive bandwidth limited by the capacitance of the active device and the source and load conductances; bandwidth is traded for gain. The obvious way out is to start with a circuit having a very large passive bandwidth. This is precisely what is done in the traveling-wave tube, and it is for this reason that traveling-wave masers and traveling-wave parametric amplifiers are receiving so much attention.<sup>17-19</sup> These amplifiers take the form of slow-wave structures to which are coupled slabs of ruby or rutile (in the case of masers) or diodes (in the case of parametric amplifiers). Slow-wave structures are used to get high-interaction impedances and high gain per unit length. The appropriate relations are shown in Figure 9. It will be seen that slowing down the wave propagation (i.e., decreasing the phase velocity,  $v$ ) increases the gain parameter  $G/(2vC)$ . Thus, the traveling-wave schemes provide a large bandwidth, can provide high gain with a long structure, and have separate input and output connections. The separate input and output connections do not ensure stability, and any mismatch at the output termination can cause serious feedback and instability. In traveling-wave tubes, attenuation is intro-

---

<sup>14</sup> K. K. N. Chang and S. Bloom, "A Parametric Amplifier Using Lower-Frequency Pumping," *Proc. I.R.E.*, Vol. 46, p. 1383, July, 1958.

<sup>15</sup> K. K. N. Chang, G. N. Heilmeyer, H. J. Prager, "Low-Noise Tunnel Diode Down Converter Having Conversion Gain," *Proc. I.R.E.*, Vol. 98, p. 854, May, 1960.

<sup>16</sup> D. I. Breitzer, "Noise Figure of Tunnel Diode Mixer," *Proc. I.R.E.*, Vol. 98, p. 935, May, 1960.

<sup>17</sup> R. W. DeGrasse, E. O. Schulz-Dubois, H. E. D. Scovil, "The Three-Level, Solid-State, Traveling-Wave Maser," *B.S.T.J.*, Vol. 38, p. 305, March, 1959.

<sup>18</sup> P. K. Tien, "Parametric Amplification and Frequency Mixing in Propagating Circuits," *Jour. Appl. Phys.*, Vol. 29, p. 1347, September, 1958.

<sup>19</sup> R. S. Engelbrecht, "A Low-Noise, Nonlinear Reactance Traveling-Wave Amplifier," *Proc. I.R.E.*, Vol. 46, p. 1655, September, 1958.

duced into the slow-wave structure near the center to absorb any power reflected by the output termination, or, in some cases, the slow-wave structure can be severed. These schemes are quite satisfactory where part of the energy is transported by an electron beam moving in the forward direction so that the forward signal is not lost by attenuation or an interrupted structure. In devices where power is not transported in the forward direction by the active material or devices, these artifices will not work. In traveling-wave masers, a ferrite slab is placed in a region adjoining the slow-wave structure where there is circular polarization of the r-f magnetic field. The slab is oriented to pass power proceeding in the forward direction but to absorb any power proceeding in the backward direction.

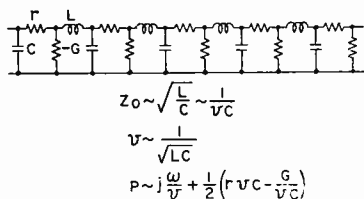


Fig. 9—Characteristic impedance, phase velocity, and propagation constant of a traveling-wave, negative-resistance amplifier.

The Adler tube does not need these embellishments, since the input and output are separate and isolated. The amplifier is stable and the gain is high. Principal limitations of this device are its bandwidth, which is determined by the consideration that the signal frequency must be close to the cyclotron frequency, and its structure, which can be awkward at higher frequencies.

#### STATUS OF LOW-NOISE AMPLIFIERS

It is now pertinent to examine and compare the performance of the low-noise amplifiers discussed above. The performance of masers is illustrated by Figure 10, which shows the bandwidth achieved at 20 decibels gain at various frequencies.<sup>20</sup> Noise factors, which are not shown, are low. Even with the added noise due to plumbing, circulators, and the other hardware necessary for a practical system, noise figures of 0.4 decibel and lower have been achieved.

The performance of typical traveling-wave tubes, parametric am-

<sup>20</sup> These data were kindly supplied by H. R. Lewis of RCA Laboratories.

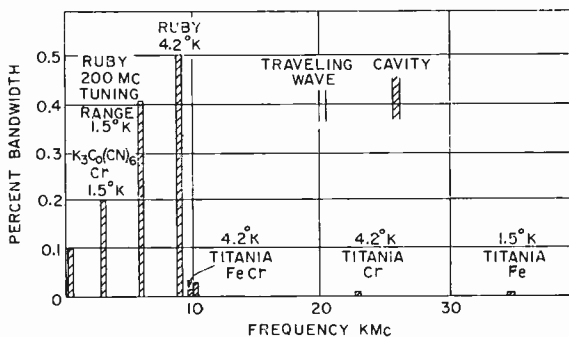


Fig. 10—Maser performance at 20 db gain.

plifiers, and tunnel diodes is illustrated in Table I. The chart is self-explanatory and needs no comment other than to note that the helix parametric amplifier is a traveling-wave amplifier which utilizes a helix as a slow-wave structure.<sup>21</sup> The particular amplifier cited had two diodes along its length.

Table I—Performance of Some Typical Low-Noise Amplifiers.

Type	$f_s$ mc	$f_p$ mc	$f_o$ mc	$\Delta f$ mc	Gain db	NF db
<i>TWT</i>						
Forward wave	3,000	.....	3,000	300†	20	2.5
Backward wave	10,000	.....	10,000	1,000†	20	4.0
<i>Parametric</i>						
Amplifier	5,850	11,700	5,650	8	18	3
	11,550	23,100	11,550	53	10	3.2
Up-converter	460	8,915	9,375		9	2±0.5
	1	20	21	0.1	10	0.4
Traveling-wave	380	630	380	10-20	10-12	3.5
Helix	2,800	3,800	2,800	*	26	5-7
Adler tube	560	1,120	560	50	20	1.3
<i>Tunnel Diode</i>						
Amplifier	4,500	0	4,500	20	23	7
Down-conv. (Ge)	210	0	30	0.9	6	5.2
(GaAs)	210	0	30	0.15	22.7	2.8

† The range in which the noise factor is near the value cited.

\* Can be tuned through 80 mc range by tuning pump through 100 mc.

<sup>21</sup> G. Conrad, K. K. N. Chang, R. D. Hughes, "A Diode-Loaded Helix as a Microwave Amplifier," *Proc. I.R.E.*, Vol. 48, p. 939, May, 1960.

How these amplifiers compare and how they stack up against systems requirements is shown in Figure 11. In this figure, all of the noise factors have been reduced to equivalent noise temperatures, as defined by the relation

$$T_e = T_0(F - 1), \quad (15)$$

where  $T_e$  is the effective noise temperature and  $T_0$  is the reference temperature ( $300^\circ\text{K}$  in this case). In Figure 11, the noise due to galactic sources appears on the left. The noise temperatures of such sources drops rapidly with frequency and, aside from radio stars, the noise temperatures of such sources drops rapidly with frequency and, aside from radio stars,

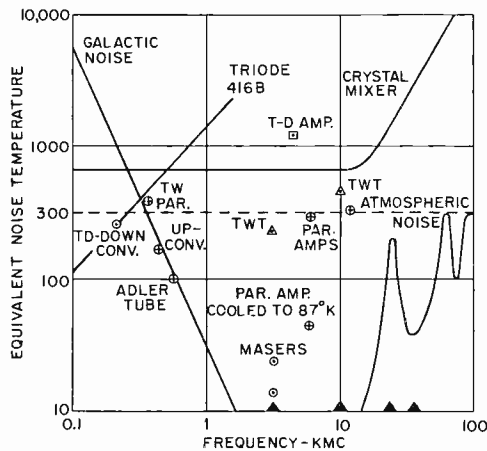


Fig. 11—Noise performance of various low-noise amplifiers relative to natural noise sources.

becomes negligible above 1 kilomegacycle. The noise due to atmospheric absorption is shown at the right. It rises steeply at about 10 kilomegacycles and, aside from a pair of “windows,” has a noise temperature approximately equal to the temperature of the earth.

The three noise sources (galactic, atmospheric, and the earth) determine what is required of an amplifier. If the antenna looks upward and is highly directional so that it does not see the earth through side lobes or spill-over, the amplifier should have a noise temperature as low as the galactic noise temperature, or, if the frequency is above 10 kilomegacycles, as low as the atmospheric temperature, to achieve the ultimate in performance. If the antenna sees the earth, amplifiers with a noise temperature below  $300^\circ\text{K}$  are adequate.

The noise temperature of a familiar triode is shown at the left in Figure 11. It still looks like a good low-noise tube below 500 megacycles. At frequencies below 1 kilomegacycle, tunnel-diode down-converters and a variety of parametric amplifiers, provide noise figures low enough for any application. Above 1 kilomegacycle, masers outshine everything else, both as to noise figure and operating frequency (the black triangles show frequencies at which masers have been operated). Traveling-wave tubes and room-temperature parametric amplifiers are adequate for systems in which the antenna sees the earth. Parametric amplifiers with the idler circuit cooled show indications of competition with masers and, with the development of better diodes, may give the maser real competition for upward looking applications. The tunnel-diode amplifier has yet to make itself felt above 1 kilomegacycle. The 7-decibel noise figure at 4.5 kilomegacycles indicates potentiality, and further refinements in diodes may make it a real contender.

It seems to the present writer that each of these devices will find its own place. At low frequencies, all provide adequate performance and the choice will be determined by specific rather than general requirements and by economics. At frequencies above 1 kilomegacycle, the traveling-wave tube offers unparalleled bandwidth and is quite satisfactory for applications in which the antenna sees the earth. For radio astronomy, for communication above the atmosphere, and for other applications where the antenna does not see the earth, masers and cooled parametric amplifiers yield the best noise performance. Above 10 kilomegacycles, the maser stands alone and may continue to do so for a long time to come. Its operation does not depend on charge transport and the RC limitation that goes with charge transport.

#### TRANSMITTING TUBES

Present transmitting tubes are able to provide power outputs in excess of a kilowatt average at frequencies up to 10 kilomegacycles. Such power outputs have been achieved with magnetrons, amplitrons, traveling-wave tubes, and klystrons. Grid-controlled tubes, both triodes and tetrodes, perform well up to about 1 kilomegacycle and give impressive power outputs, but they tend to bog down at higher frequencies because of transit-time effects. The general characteristics of all of these tubes are summarized in Table II. At very high power outputs, the bandwidths of klystrons and traveling-wave tubes tend to become comparable. In order to handle the circuit dissipation at high powers in the traveling-wave tube, the slow-wave structure takes the form of coupled cavities; therefore, the circuit

Table II—General Characteristics of Power Amplifiers.

Characteristic	Triode Tetrode	Magnetron Amplitron	TWT	Klystron
Frequency (mc)	< 1200	> 400	> 400	> 400
Power gain (db)	< 20	< 20	> 20	> 20
Bandwidth (%)	~ 15	> 15	> 15	< 15
Efficiency (%)	~ 50	60	35	40
Operating voltage (kv)	< 50	< 50	> 50	> 50

becomes dispersive instead of smooth and the bandwidth decreases. It is to be noted that high-power traveling-wave tubes and klystrons operate at voltages above 50 kilovolts, and voltages in excess of 200 kilovolts have been used.

All of these transmitting tubes are subject to the fundamental limitations outlined in Table III. The power output per unit area of any tube is determined by the emission density available from the cathode and the output impedance per unit area. The output impedance per unit area is determined by the bandwidth and the output capacitance per unit area;

Table III—Power Tube Limitations  $\left( P_o = j^2 R A = j^2 \frac{1}{\Delta\omega C} A = j^2 \frac{1}{\Delta\omega C} \lambda^2 \right)$ .

	Definition	Determined by
$P_o$	Power output	System requirement
$j$	Emission density	Cathode
$R$	Load res. per unit area	Output capacitance $C$
$A$	Area	Moding
$\Delta\omega$	$2\pi \times$ bandwidth	System requirement
$C$	Capacity per unit area	Space charge
$\lambda$	Wavelength	System requirement

$$R = \frac{1}{\Delta\omega C}. \quad (16)$$

The output capacitance, in turn, is determined by electron-space-charge effects. This is easily seen in the case of a triode. Suppose the triode is operated as a grounded-grid, class-B amplifier and that the plate voltage is swung down to the peak grid voltage to ensure maximum efficiency. Then the maximum plate current passes when the grid and plate voltages are equal. The space charge in the grid-anode space depresses the potential between the grid and plate; the greater the spacing between grid and plate, the greater the potential depression. If the grid-anode spacing is increased beyond 2.8 times the cathode-grid spacing in an effort to reduce the output (grid-plate) capacitance, a virtual cathode will form in the grid-anode space. The virtual cathode will reflect electrons to the grid with disastrous effects on the grid. Thus, the maximum grid-anode spacing and the minimum output capacitance are determined by space charge. Similar considerations apply to all transmitting tubes.

The total power output of the tube, then, will be determined by the emission density, the bandwidth required, the output capacitance per unit area, and the area. The area that can be used is determined by the wavelength and is, in fact, proportional to the square of the wavelength. By way of illustration, consider a cylindrical triode. The length of the active section of the tube must be less than a quarter wavelength, otherwise the droop of voltage at the ends of the active section will impair the efficiency. The periphery of the tube must be less than one wavelength. If the periphery exceeds one wavelength, higher-order modes excited by inevitable small asymmetries are possible. These modes unbalance the tube and impair the efficiency, to say the least. Thus, both length and periphery are proportioned to the wavelength, and the active area is proportional to square of the wavelength.

To sum up, the power output of a transmitting tube is determined by:

1. The emission density available from the cathode (a fundamental limitation).
2. The bandwidth required (a systems requirement).
3. The output capacitance (a fundamental limitation).
4. The area (at present this is a very real limitation, but one that may yield to ingenuity).

With these considerations in mind, a plot of the power output of available power tubes against frequency-squared should indicate the state of the art. An equivalent plot, that of the logarithm of power output versus the logarithm of frequency, is shown in Figure 12. Two straight lines corresponding to  $P_0 f^2 = \text{constant}$  have been drawn through the data. The two lines correspond to the state of the art at

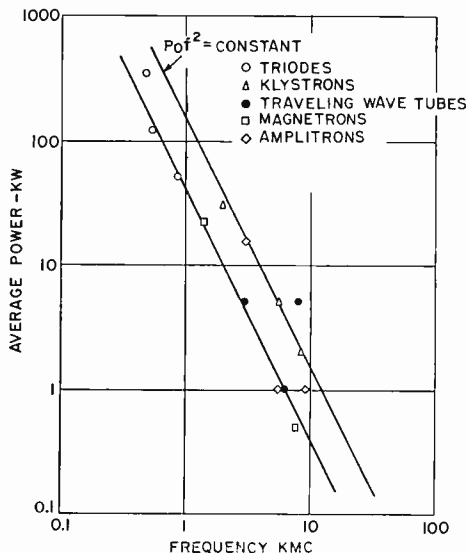


Fig. 12—Power output of typical power tubes as a function of frequency.

times which are roughly a year apart. The plot is not complete; many of the more powerful tubes are classified, and information on them is not available. However, the plot does show that all transmitting tubes have been brought to a comparable degree of perfection, and that the state of the art is given approximately by the equation

$$P_0 f^2 = 100 \quad (17)$$

where  $P_0$  is the average power output in kilowatts and  $f$  is the frequency in kilomegacycles.

It seems likely that still higher power outputs are possible by refinements in present techniques. At frequencies above 1 kilomegacycle, these improvements are most likely to come in klystrons, magnetrons, and traveling-wave tubes. At the moment, the increases in power output to be expected from refinement do not seem large, however, and a major break-through may be required to achieve order-of-magnitude improvements.

## CONCLUSION

The present paper has reviewed the present "glamor" amplifiers and has tried to put them on a common footing to compare their merits. On the basis of such a comparison it is concluded, that

1. All are capable of adequate performance at frequencies below 1 kilomegacycle.
2. Traveling-wave tubes, tunnel-diode amplifiers, and uncooled parametric amplifiers are capable of adequate performance at frequencies between 1 and 10 kilomegacycles in applications where the antenna sees the earth.
3. Masers and cooled parametric amplifiers are capable of adequate performance under any conditions at frequencies between 1 and 10 kilomegacycles.
4. The maser stands unchallenged in performance at frequencies above 10 kilomegacycles.

The present performance of transmitting tubes has been outlined and compared with the fundamental limitations on transmitting tubes. It is surmised that an order of magnitude improvement may require a major breakthrough.

# THE ULTRA-HIGH-VACUUM SYSTEM FOR THE C-STELLARATOR\*

BY

KARL DREYER AND JOHN T. MARK

RCA Electron Tube Division,  
Lancaster, Pa.

*Summary*—In building the vacuum system for the C-Stellarator, it was first necessary to solve many problems of design and fabrication of the component parts. Final assembly did not impose serious hardships, except in cases where the preliminary work proved to be inadequate. This paper describes much new knowledge gained during the course of the work. The welding and joining of stainless steels, the assembling of glass and ceramics into vacuum vessel systems, and the achievement of an ultra-high vacuum and its accurate measurement are described. Many of the arts of electrical control systems, material cleaning, lubrication and movement of parts in vacuum, and electrical and thermal insulation, are also discussed.

## INTRODUCTION

THIS paper describes the novel features of the vacuum system which was built and tested at the Lancaster Plant of the RCA Electron Tube Division for the C-Stellarator for subsequent installation at Princeton University. The detailed design and construction of the Stellarator for operation by Princeton University were carried out by Allis-Chalmers and the Radio Corporation of America under the direction of a supervisory group known as C-Stellarator Associates, which comprises technical personnel of both Allis-Chalmers and RCA. The C-Stellarator is to be used for research in the field of controlled thermonuclear fusion in the Matterhorn Project at the Forrestal Research Center in Princeton, N. J., as part of the Atomic Energy Commission's Sherwood Project for Peaceful Applications of Atomic Energy.

The problem of controlled thermonuclear fusion is concerned with the application of the physics of a high-temperature plasma confined by a magnetic field. The C-Stellarator is an experimental machine which will permit the study of the physics of such a plasma, particularly as it relates to basic Stellarator concepts. One of the major purposes of the C machine is to study plasma instabilities and stabilizing methods. The confining field is generated by external coils powered from motor

---

\* Manuscript received 15 July 1960.

generators. It will be operated continuously at low-power levels and pulsed at high-power levels with confining fields of 50,000 gauss.

The vacuum vessel in which the plasma is formed is oval in shape to avoid end effects. The C-Stellarator vessel is made of 8-inch diameter stainless steel tubing with a ceramic insulating gap. The desired gas is injected into the vessel at a rate to produce the desired pressure with the diffusion pumps in operation. This gas is broken down by the application of r-f voltages across the gap. Complete ionization and some heating is achieved by passing 30,000 to 50,000 amperes through the plasma, which forms the single turn secondary of a transformer. Further heating methods which use r-f electric fields normal to the confining magnetic field lines will be studied later.

The specifications for the vacuum system of the C-Stellarator are extremely severe. A vacuum of at least  $3 \times 10^{-10}$  mm of Hg must be maintained in a stainless-steel vessel with a volume in excess of 25,000 cubic inches—a vessel which is greatly complicated by the many diagnostic ports and other attachments required to permit the physicist to obtain data.

The enormity of the problem may be appreciated from the fact that until quite recently, a vacuum of  $3 \times 10^{-10}$  mm of Hg was possible only in a small volume and under laboratory conditions. In a volume the size of that of the C-Stellarator, a vacuum of  $3 \times 10^{-8}$  would have been considered a significant accomplishment. The successful construction of the C-Stellarator system, then, represents a technical advance of something like two orders of magnitude.

An ultra-high vacuum is required, not because a base pressure of  $3 \times 10^{-10}$  mm Hg is a measure of the allowed gas impurities level, but rather as a measure of the cleanliness of the walls of the vessel.

The vacuum system consists basically of two major sections—the vessel and the pumping system. The vessel, shown in Figures 1 and 41, is constructed of stainless-steel tubing with an inside diameter of 8 inches. The tubing is arranged in an oval configuration with an axial length of approximately 40 feet. The radius of the end “U” bends is 43 inches to the centerline of the tube. The vessel is demountable and bakeable and is equipped with expansion joints to compensate for the thermal and mechanical stresses anticipated during operation, a pump box to serve as a manifold connecting to the pumping system, and other auxiliary components. The ceramic section opposite the pumping station acts as an insulating break and ultimately as a coupling for the application of the r-f field to the plasma. Diagnostic port crosses are equipped (interchangeably) with smaller ceramic-to-metal seals for

use as high-voltage standoffs for ionization gauges, or with sapphire or glass windows to facilitate diagnostic apparatus for plasma analysis.

The work on the vacuum system was performed in two phases. Phase One, the Vacuum Test Facility, was an experimental program and Phase Two, the C-Stellarator Vessel and Pumping System, was a design and testing program.

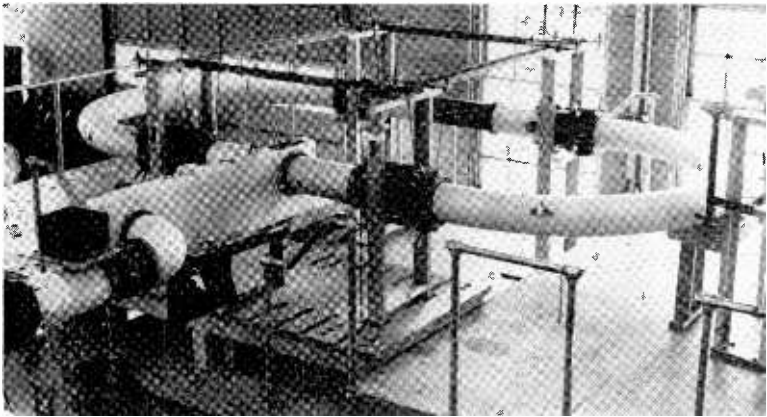


Fig. 1—Photograph showing the junction between pump box and vacuum vessel. Spring-loaded stainless-steel suspension wires are also shown.

#### PHASE ONE—THE VACUUM TEST FACILITY

The initial phase of the project was the construction of a vacuum test facility to determine how to scale up the size of the smaller systems developed at the Forrestal Research Center. Answers to the following specific questions were sought.

1. Would large pumps (more than 4 inches in diameter) produce ultra-high vacuum?
2. Would mercury or oil be more suitable as a pump fluid?
3. What type of vacuum gauge would be suitable for measuring the ultra-high vacuum obtained?
4. What trap configuration would best yield maximum conductance with minimum liquid-nitrogen consumption?
5. What types of seals would be adaptable for the numerous joints under the prescribed temperature conditions, material combinations, and anticipated stresses?

6. What flange design would be best suited for the interchangeable joints so as to provide ease of assembly, vacuum tightness, and ruggedness?
7. What preassembly cleaning procedure would give greatest assurance of meeting the ultra-high-vacuum stipulation of  $3 \times 10^{-10}$  mm of Hg after a reasonable bakeout procedure? What would be the optimum bakeout temperature consistent with dimensional, material, and power-dissipation limitations?
8. Could a bakeable ultra-high-vacuum valve be designed to isolate the vessel and pumping systems manually or automatically for emergencies?
9. What testing programs would give assurance of reliability of all system components, both major and auxiliary?

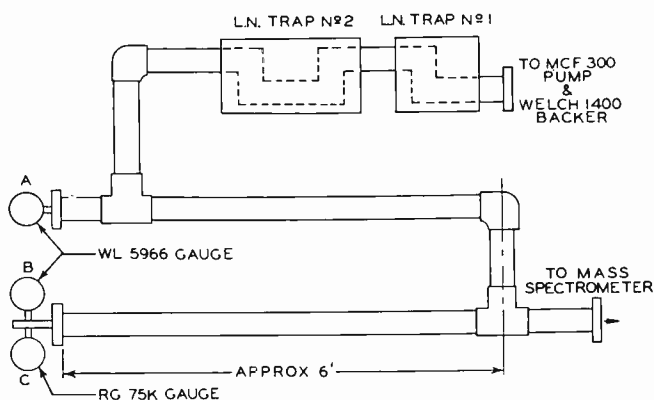


Fig. 2—15-liter-per-second vacuum system.

### *The Preliminary 15-Liter-per-Second System*

Several pumping systems were constructed and tested during the initial phase of the project. A 15-liter-per-second system constructed of 2-inch diameter stainless steel pipe, as shown in Figure 2, was used to develop operating procedures for obtaining and maintaining ultra-high vacuum. A pressure-temperature history of 22 days for this system is shown in Figure 3. Tests of pressure-versus-trap-temperature as a function of time are shown in Figure 4. This curve shows that whatever gas has collected on the trap is released when the trap warms up  $8\text{--}10^\circ\text{C}$  from the liquid-nitrogen temperature. By the use of a bakeable mass spectrometer, it was determined that a gas

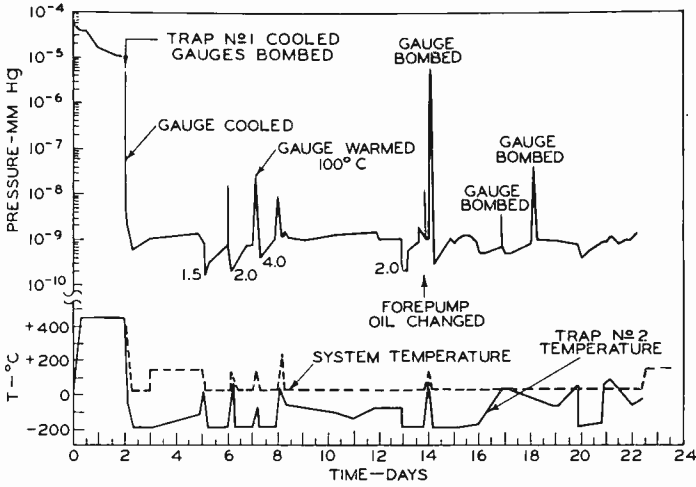


Fig. 3—Pressure-temperature history of the 15-liter-per-second vacuum system.

of mass 28 was released; this was assumed to be carbon monoxide. It was further noticed that the mass spectrometer could not pick up any signal when the system pressure was at  $5 \times 10^{-11}$  mm of Hg. This observation was interpreted to mean that the mass spectrometer was not the source of any carbon monoxide.

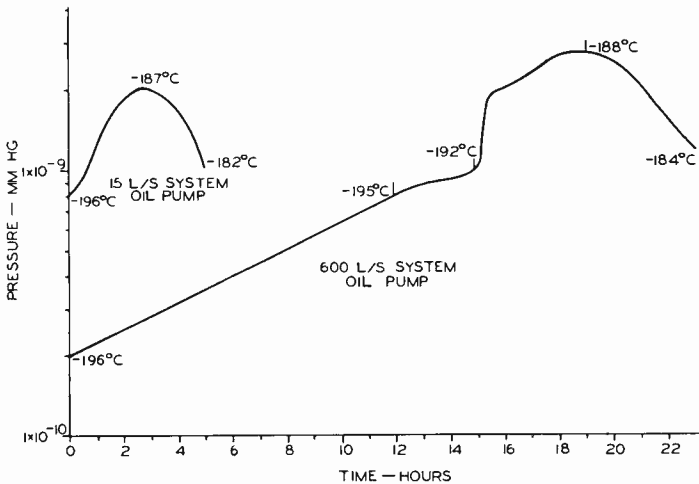


Fig. 4—Curves showing pressure-vs.-trap temperature characteristics for two systems as a function of time.

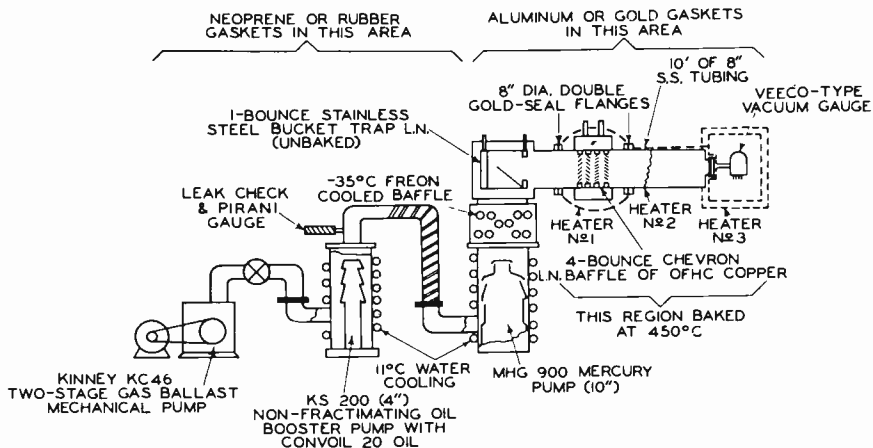


Fig. 5—600-liter-per-second mercury pumping station used for test evacuation of 10-foot vessel.

600-Liter-per-Second Systems

In another test, a 600-liter-per-second pumping system using an MHG 900 mercury diffusion pump was connected to a stainless-steel vessel made of a 10-foot-long, 8<sup>5</sup>/<sub>8</sub>-inch-diameter pipe, as shown in Figure 5. After a 450°C bake, the vessel pressure reached  $4 \times 10^{-10}$  mm of Hg, as shown in Figure 6. Later, after a 4-hour power failure

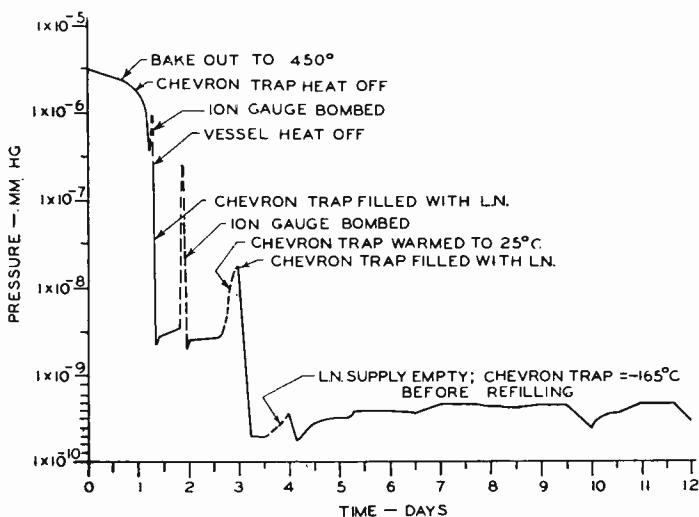


Fig. 6—Pressure history for the arrangement shown in Figure 5.

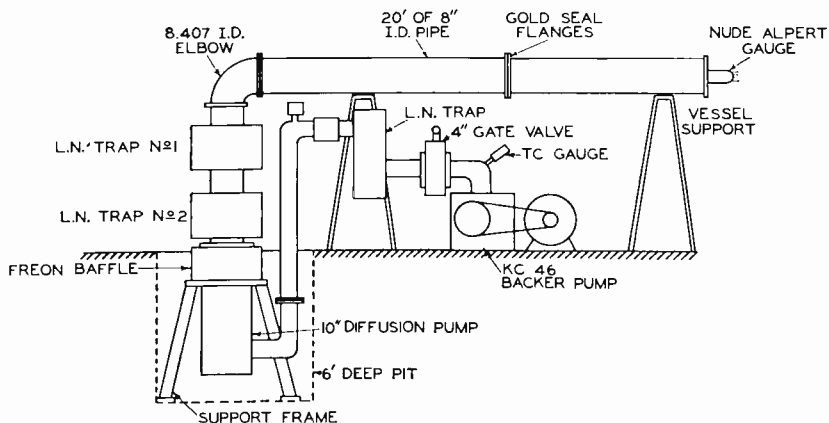


Fig. 7—600-liter-per-second oil pumping station used for test evacuation of 20-foot vessel.

during which the vessel pressure rose above a micron, the system was pumped back to the  $10^{-10}$  mm range without rebakeout of the vessel.

Another 600-liter-per-second pumping system was connected to a 20-foot-long stainless-steel vessel made of 8-inch-inside-diameter tubing, as shown in Figure 7. This system was evacuated with an MCF 1400 10-inch-diameter oil-diffusion pump. A pressure history of the system covering a period of 16 days is shown in Figure 8. Subsequently, this system was changed over to a mercury-pumped system using an

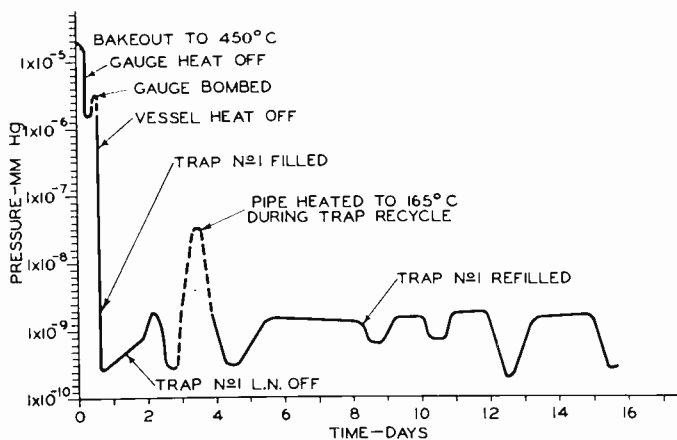


Fig. 8—Pressure history for the arrangement shown in Figure 7; MCF-1400 pump used.

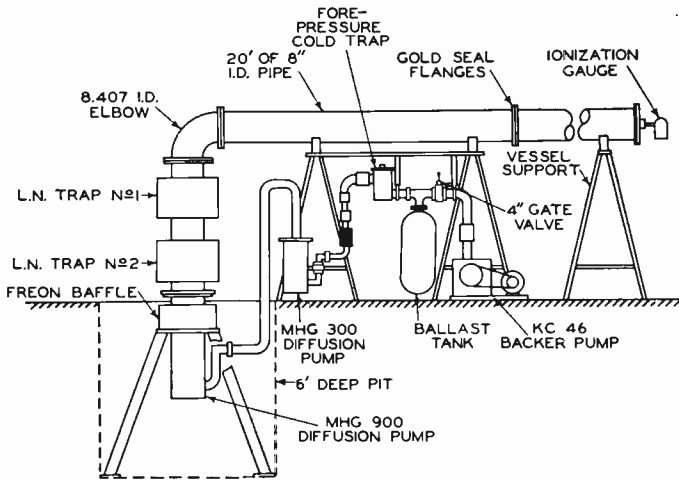


Fig. 9—600-liter-per-second pumping system using MHG 900 mercury-diffusion pump.

MHG 900 pump, as shown in Figure 9. A pressure history of this system is shown in Figure 10. The MHG 900 pump system was chosen for the first-stage Stellarator operation because mercury can be trapped fairly effectively, whereas some products of oil fractionation cannot be trapped at liquid-nitrogen temperatures. Such contaminants would be undesirable in the Stellarator vessel.

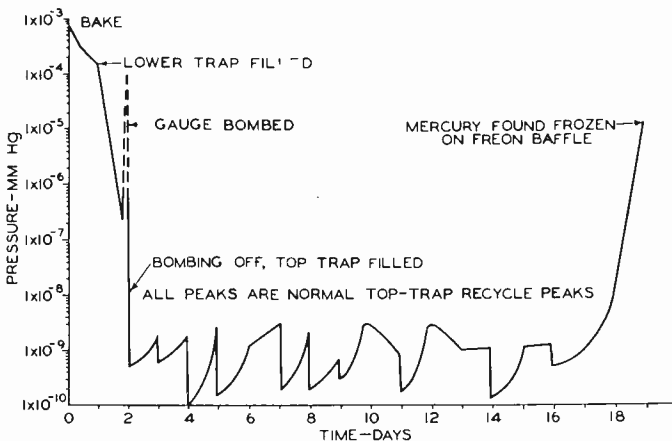


Fig. 10—Pressure history of the arrangement shown in Figure 9.

Forepressure-tolerance characteristics for nitrogen and helium were determined by separately leaking nitrogen or helium into the foreline and observing any change in fine pressure of the pump as the forepressure was increased. The results of these tests are plotted in Figures 12 and 13. It is to be noted that the Leybold DO-2001 10-inch oil pump is superior to the other pumps in this respect.

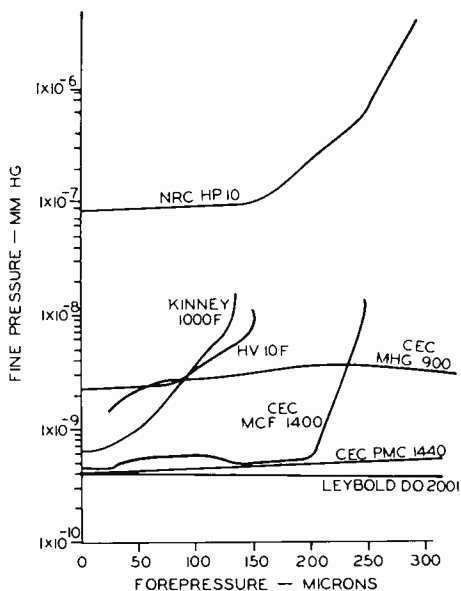


Fig. 12—Forepressure-tolerance characteristics of various pumps for nitrogen gas.

Relative backstreaming of the pumps was checked by means of a glass collection dome with the oil draining into a 1-millimeter diameter capillary tube as shown in Figure 14. This dome was placed over the top flange of each pump, and the rate at which oil collected in the capillary was used as a measure of backstreaming. The data presented in Figure 15 indicate that some pumps are particularly poor with respect to backstreaming, whereas the CVC PMC-1440 and Leybold DO-2001 are superior.

The pump-speed measurements for several of the most promising pumps were made with the setup shown in Figure 16. A 1500-liter tank is evacuated by the pump under test while pressure-versus-time data are automatically recorded from a log amplifier output of collector current fed onto a log chart recording instrument. Thus, the

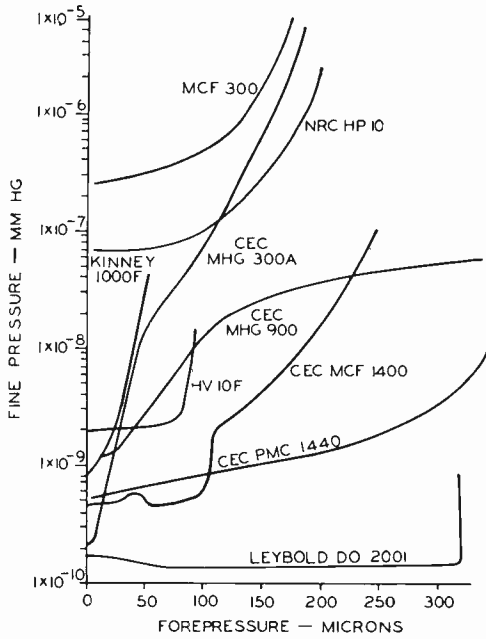


Fig. 13—Forepressure-tolerance characteristics of various pumps for helium gas.

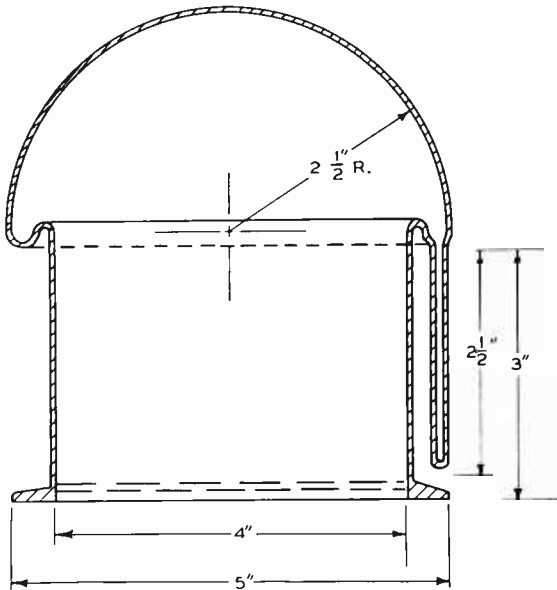


Fig. 14—Cutaway drawing of glass dome arrangement used to test backstreaming characteristics of high-vacuum pumps.

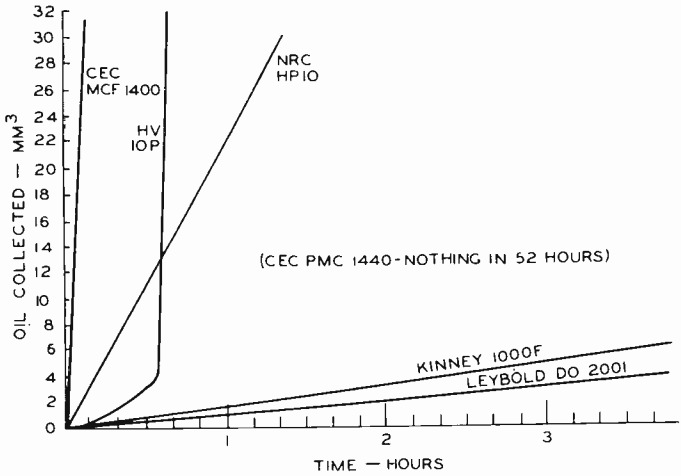


Fig. 15—Relative-backstreaming characteristics of various pumps.

slope of the curve is proportional to pump speed. Speeds were recorded as shown in Figure 17. Pump-speed tests of three pumps were made for both nitrogen and helium; the results are shown in Table II. In general, the measured pump speeds were found to be comparable to quoted catalog speeds.

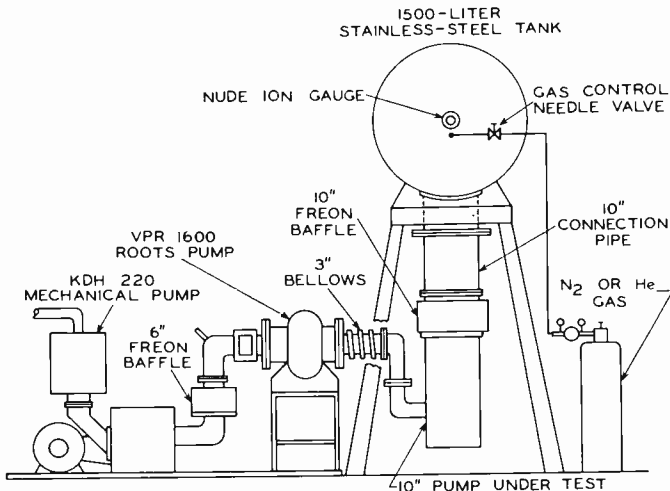


Fig. 16—Arrangement used for pump-speed measurements.

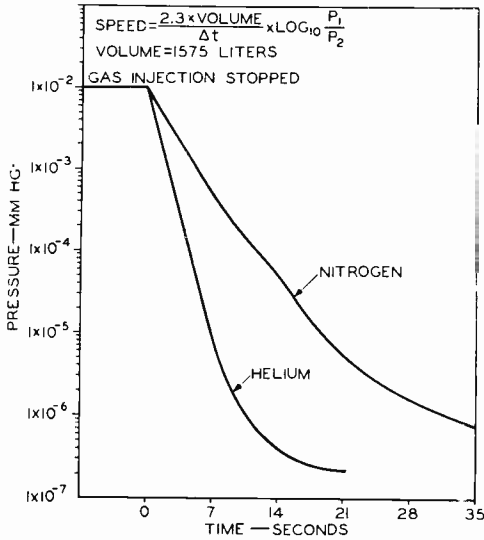


Fig. 17—Typical pump-speed measurement curves.

*Gauging*

Bayard-Alpert gauges are employed to indicate pressures in the Stellarator vessel and high-vacuum pump lines. A typical gauge mounting is shown in Figure 18. These gauges were baked along with the vessel to a temperature of 400°C. Other gauge arrangements used during tests include a glass “nude” type and a metal-ceramic type, shown in Figures 19 and 20.

Table II—Summary of Pump-Speed Data for Three High-Vacuum Pumps.

Pump	Measured Pumping Speed (Liters/Second)	
	N <sub>2</sub>	He
NRC		
HP 10	725	1400
LEYBOLD		
DO2001	750	1500
CEC		
MHG-900	725	1500

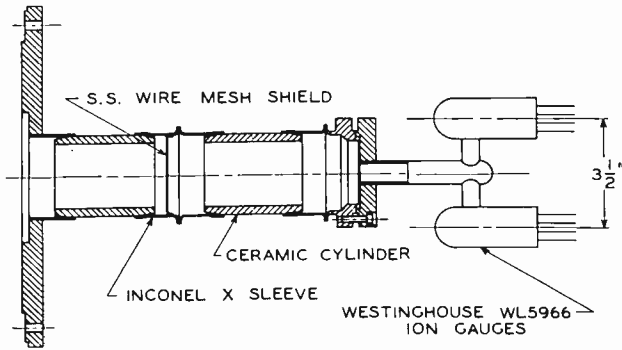


Fig. 18—Typical mounting arrangement for ionization pressure gauges.

### *Liquid-Nitrogen Traps*

The pump tests showed that liquid-nitrogen traps would be required to achieve ultra-high vacuum in the Stellarator. The following design prerequisites for a good liquid-nitrogen trap were established:

1. The trap must offer a minimum impedance in the pumping system,
2. All the walls must be cold and remain constantly cold,
3. There must be no warm path around the cold surface by which molecules of the pump fluid could migrate from the low-vacuum region to the high-vacuum region.
4. Consumption of liquid nitrogen must be held to a minimum.

A trap meeting these specifications was designed and placed in use;

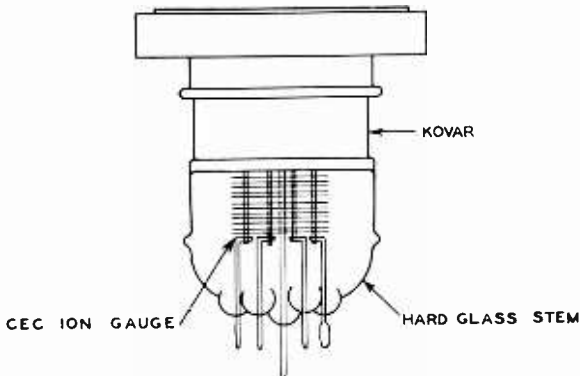


Fig. 19—"Nude" glass-to-metal ionization gauge.

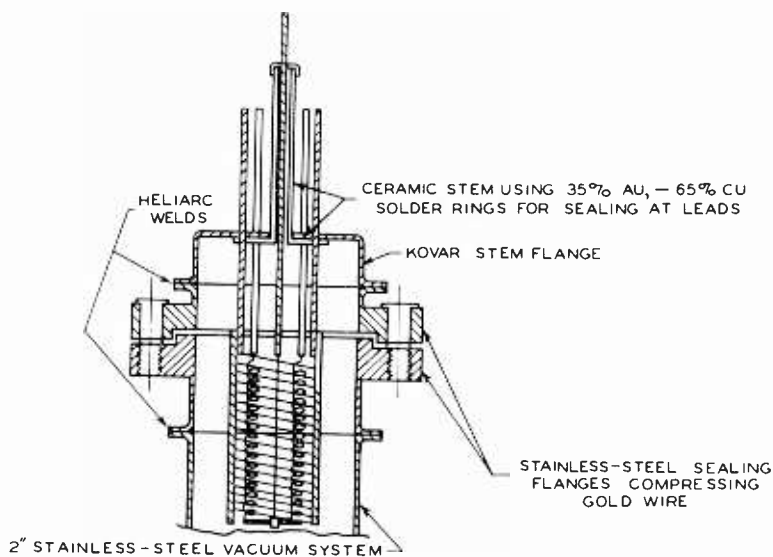


Fig. 20—Ceramic-to-metal ionization gauge.

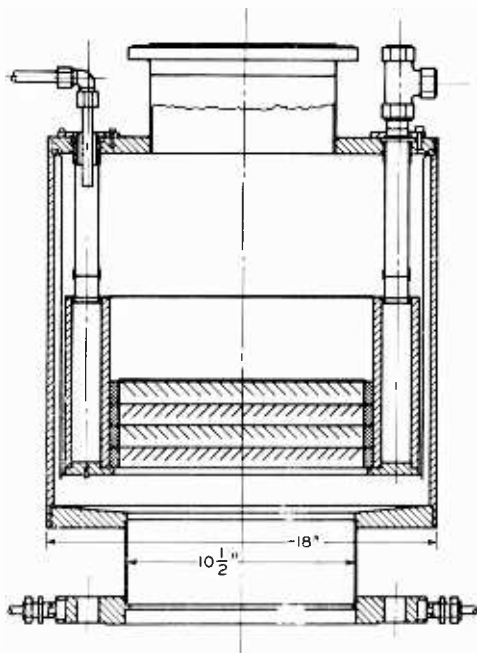


Fig. 21—Cross section of 2000-liter-per-second liquid-nitrogen chevron trap.

its performance has met all requirements. A cross section of this trap is shown in Figure 21. With two of these traps in series over a Freon\* baffle, pressures of  $2 \times 10^{-10}$  mm of Hg have been obtained in vacuum vessels for long periods of time.

## PHASE TWO—THE C-STELLARATOR VESSEL AND PUMPING SYSTEM

### Gold Seals

For those sections of the vacuum vessel and the pumping system which are subject to bakeout, flanged joints of the corner-gold-seal type were used. A total of 69 gold seals are used in the entire system, and the total lineal gold-seal surface is 1179 inches, or about 98 feet. The basic design of such a joint is shown in Figure 22.

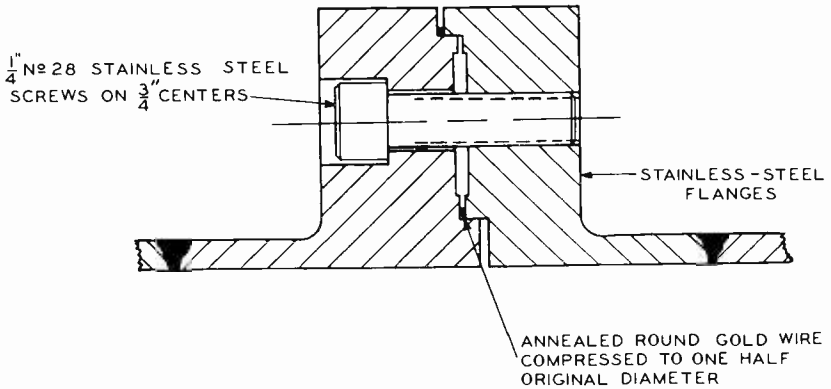


Fig. 22—Simplified drawing of a double gold-seal flange.

For satisfactory vacuum-tight seals, very accurate control of the gold-seal diameters is necessary. The gaskets are banded about the male flanges (left side of Figure 22). In all cases of such double seals, vacuum integrity is dependent upon the mating flanges. The outer seal is for balance purposes to minimize radial flange distortion due to compressive forces of the bolts. *For both seals*, however, the clearance between the male and female flanges must be maintained with extreme accuracy.

The derivation of the gold-seal dimension parameters is best illustrated by the experimental data of Table III which was obtained by use of a Tinius-Olsen Tester. Early experience with bolts made of type

\* Registered trade mark.

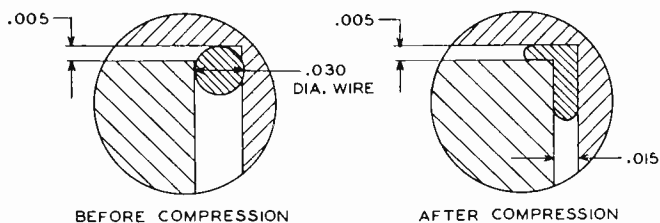


Fig. 23—Enlarged views of correct corner seals before and after compression.

305 stainless steel dictated the use of the parameters shown in Figure 23 which imposed a stress of 25,050 pounds per square inch on a  $\frac{1}{4}$ -inch-diameter bolt. However, mechanical seizures of the bolt in the flange were not uncommon at high stress levels; further studies led to the selection of bolts made of a hardenable alloy, A286, using a proprietary lubricant, "Thred-Gard." Other lubricants, especially molybdenum sulfide compounds, proved of negligible value after baking at 450°C.

Table III—Summary of Data on Gold Vacuum-Seal Compression Test.

Type of Compression Seal	Gasket Diameter (Inches)	Compressed Diameter (Inches)	Radial Clearance (Inches)	Force Required For Compression (Pounds/Inch)	Stress Per Bolt On Standard Seal Ring ( $\frac{1}{4}$ -28 Bolt) (Pounds/Square Inch)
flat	0.020	0.010	—	795	15,600
flat	0.029	0.008	—	1,240	24,300
flat	0.030	0.010	—	1,520	29,900
flat	0.030	0.008	—	3,650	72,000
corner	0.020	0.010	0.001	1,395	27,500
corner	0.020	0.008	0.001	2,150	42,500
corner	0.020	0.010	0.002	857	16,900
corner	0.020	0.008	0.002	1,430	28,300
corner	0.020	0.010	0.005	704	13,850
corner	0.020	0.008	0.005	1,135	22,400
corner	0.030	0.015	0.002	1,470	29,000
corner	0.030	0.012	0.002	2,360	46,600
corner	0.030	0.015	0.004	1,100	29,000
corner	0.030	0.012	0.004	1,770	46,500
corner	0.030	0.015	0.005	1,275	25,050
corner	0.030	0.012	0.005	2,000	39,500

NOTE: All gaskets annealed at 600°C in air for one hour.

### *System Bakeout*

In the development of systems for the C-Stellarator, it has been the practice to bake the entire vacuum system at 450°C for a period of at least 18 hours for the first bake and at least 10 hours for subsequent bakings after the vacuum system is opened to air. However, there are exceptions to this baking time. For example, some mercury-pumped systems have been operated at vacuums of  $10^{-10}$  mm of Hg after exposure to air without subsequent bakeouts. The stainless-steel vacuum system was kept heated at 150°C during the time it was exposed to atmosphere and, thus, moisture was prevented from condensing on the vacuum-system surface. No unbaked parts were added to the system when it was exposed to atmosphere.

The bakeout procedure for the entire system has been described. Pressure during the 450°C bakeout should be approximately  $5 \times 10^{-5}$  mm of Hg. In a stainless-steel vacuum system having one trap cold and the rest of the system at room temperature, for example, normal pressure readings using an MCF-300 pump were  $1 \times 10^{-9}$  mm of Hg. Trap No. 2 is the so-called "clean trap" and seems to gather the carbon monoxide, oxygen, and nitrogen in the system.

Because these gases liquefy near liquid-nitrogen temperature, trap No. 2 soon becomes saturated with monolayers of gas. It is then necessary to warm the trap and allow the collected gas to be pumped away. After the trap is warmed to  $-185^\circ\text{C}$  (above the release temperature for CO, O<sub>2</sub>, and N<sub>2</sub>), it can be refilled, and the system will again drop to  $10^{-10}$  mm of Hg. This procedure is called trap "cycling" and can be continued indefinitely to increase the vacuum to the  $10^{-11}$  mm range.

Because the Stellarator vessel must remain leak tight throughout the entire bakeout cycle, very little relative motion between mechanically joined parts can be tolerated. Such motion might cause scrubbing of the gold seals, thereby destroying the intimate contact of the "dif-fused" gold with the stainless steel flange surfaces or the gasket effect of the silver plating of the radial compression type seals. The permissible leak size is smaller than  $1 \times 10^{-10}$  atmosphere cubic centimeter per second (cumulative total of all the leaks present at any one time). Obviously, this requirement does not allow much leeway in movement or mismatch of parts. The materials for these parts have been selected for their similar thermal expansion characteristics, and therefore their temperatures must be held to the same value so as to utilize these properties. The rate at which the bakeout temperature is increased is governed, therefore, by the degree of control that must be maintained

over temperatures of adjacent parts. The cool-down period is also governed by the necessity for close control. Total bakeout time is usually about four or five days.

### *Heaters*

Experiments indicated that a power input of 3 watts per square inch of surface area was sufficient to overcome the heat dissipation which would occur while the vessel was at a temperature of 450°C. Actual operation confirmed this figure for most parts, although for relatively massive parts such as flanges, a larger amount of heat insulation was necessary to reduce heat loss. Accordingly, some heaters were redesigned to provide up to 5 watts or more per square inch.

The heater materials must withstand these operating temperatures continuously without losing either their thermal or electrical insulating properties. Also, they must remain physically strong, since many of them must be removed after the bakeout. All materials must be nonmagnetic to avoid influencing the magnetic confining field.

A commercial heater was found that could be adapted for heating small or oddly shaped parts where thickness was not too critical and the heater could be removed readily. The inner surface of these heaters is asbestos cloth re-enforced with Nichrome\* wire for strength and uniform heat dispersion. The Nichrome wire heating element is encased in quartz fiber sleeving and sewed to the asbestos with quartz thread. A layer of ceramic fiber heat insulation is placed over the heating element; the thickness of this layer is determined by the space limitation and the desired outside surface temperature.

Fiber-glass cloth is suitable for the outside covering, since the temperature of the outside surface does not exceed approximately 150°C (see Figure 24). These heaters have poor electrical insulating qualities, however, and must be removed during machine operation.

At certain points, a standard commercial heater is too bulky, cannot be removed readily, and can not withstand the 5,000-volt potential difference that will exist between the vessel and the coils. It was necessary, therefore, to develop a heater to meet these requirements. This heater will heat the part to 450°C, will withstand up to 25 or 30 kilovolts before breakdown, and is only one-quarter inch thick.

This heater is built directly on the part to be heated. Layers of mica tape are wrapped on the part and the Nichrome ribbon heating element, encased in quartz fiber sleeving, is then laid or wrapped around the part with pieces of ceramic fiber paper between the windings to

---

\* Registered trade mark.

preserve their physical placement. More mica tape is put on for voltage insulation and to hold the heating element in place, and one thickness of aluminum foil is applied. A layer of ceramic-fiber paper is put on top to aid in preventing excessive heat dissipation. Another wrap of mica tape can be applied, depending on the required voltage-break-

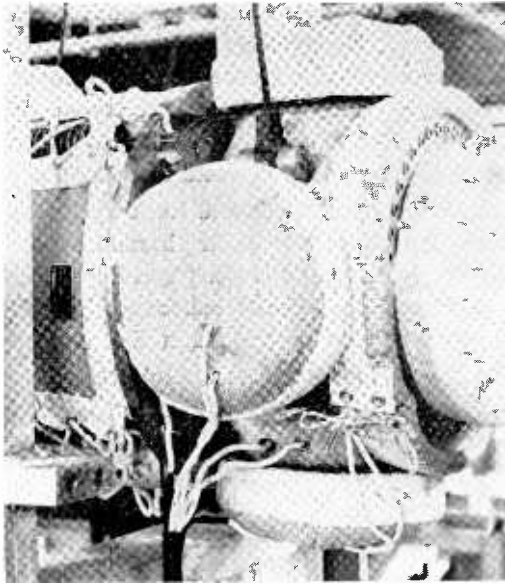


Fig. 24—Heating arrangement used for small or oddly shaped parts.

down characteristics. The whole construction is held in place with a final wrap of a glass-fiber tape which has fairly good electrical insulating qualities but virtually no thermal insulating property.

Figure 25 shows the first arrangement which successfully provided the electrical and thermal qualities required. Table IV evaluates various insulation materials which were tested for voltage breakdown with an adjustable high-voltage, low-current supply. Each was baked out to at least 450°C, and some to incandescence. Voltage-breakdown measurements were taken before and after each bakeout. For the final results, an average of six breakdown readings were taken on all baked materials.

#### *Bakeout Circuit Design*

Each vessel part has one or more separate heaters; for each heater there is a temperature-controlling device operating from a thermo-

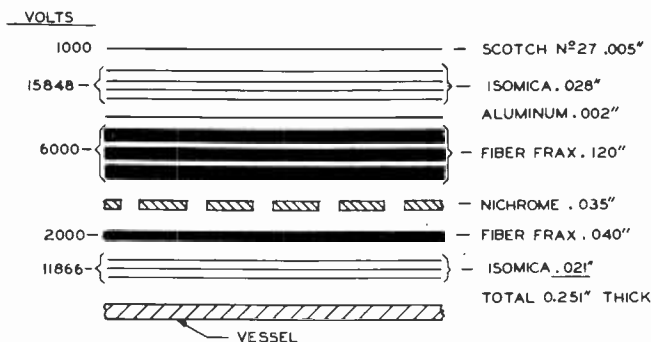


Fig. 25—Typical ¼-inch heating and insulating arrangement for the vacuum vessel. This arrangement provides 28,000 volts of insulation breakdown before bakeout.

couple input. Chromel–alumel thermocouples with quartz fiber sleeving are used. The heater power circuit contains an isolation transformer to prevent two or more simultaneous heater faults to the vessel from producing a short circuit across the power supply. The heating panels are of three standard sizes: 1 KVA, 3 KVA, and 5 KVA.

The only exceptions to these standard panels are the supplies which heat the “U” bends, where a 30-KVA supply is provided for each “U” bend. The variable output from the panel is fed to an isolation trans-

Table IV—Voltage Breakdown Measurements of Material Tested for Use in Heater Designed for Vacuum Vessel.

Baked-Out Material	Volts per 0.001 inch
1. Isomica	566
2. Scotch #27 Glass Tape	200
3. Asbestos Paper	166
4. Russel (Ecc-11-A)	150
5. Single Thickness Fiber Glass Sleeving ⅜", flat	120
6. Triple Thickness (3 mils) Fiber Glass Sleeving ¾", flat	98
7. Sheet Fiber Frax	50
8. Fiber Frax #102B-T (White)	50
9. Fiber-Frax Backed Aluminum	30
10. Fiber Frax #102B-T (dark)	0 (contained carbon)

former with a 12-volt secondary winding. A heating current of about 2400 amperes is normal. The ceramic break insulator section prevents current flow from one "U" bend to the other. Also, the supplies to the two "U" bends are phased alike so that no potential difference exists between the two ends facing each other along either the front or back sides.

Additional thermocouples are installed on all parts for monitoring their temperature on a multi-point chart recorder, with additional points provided so that especially critical parts can be more closely observed. There are 110 individual heating panels, and a total of 144 temperatures is recorded.

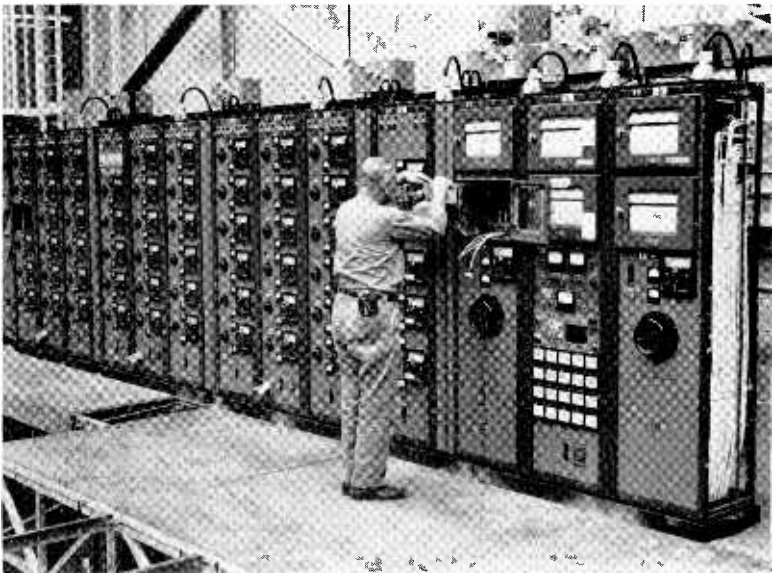


Fig. 26—Monitors and controls used for bakeout regulation of vacuum vessel.

During a typical bakeout, the temperature is raised  $25^{\circ}$  every two to three hours. At this rate, the ultimate temperature is reached in about 45 hours. The length of time the temperature is maintained at  $450^{\circ}\text{C}$  is dependent upon the vacuum conditions, which are a function of internal contamination and the leak rate. The temperature is then lowered in  $25^{\circ}$  intervals.

Twelve successful bakeouts were performed on the C-Stellarator vessel at Lancaster before it was dismantled and delivered to the Princeton site. The operating procedure and refinements to the basic

system design were developed as a result of practical experience with the test systems. Because this is essentially an experimental tool and components are subject to change, flexibility is desirable. Figure 26 shows portions of this control cabinetry during installation at the Princeton site.

### *Ceramic, Sapphire, and Glass Seals*

The vessel is equipped with a ceramic section opposite the pump box, and the diagnostic port crosses are fitted at predesignated positions with glass windows of 4-inch and 7-inch diameters. Three sizes

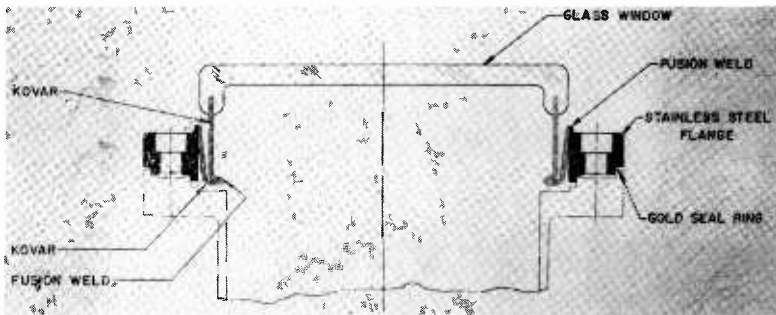


Fig. 27—Glass-window assembly.

of sapphire windows are provided for optimum ultraviolet-light transmission in port crosses, the pump box, and the left “U” bend. A large diameter (10-inch) ceramic section acts as a high-voltage insulator between the vessel and the pumping system. All of the ionization gauges are attached to the vessel with double ceramic standoff insulators for 11-kilovolt electrical isolation.

The glass windows are conventional seals of 7056 glass to Kovar.\* However, the method used to install these windows in the vessel is unique. Figure 27 shows the glass-window design.

The ceramic-to-metal seals and the sapphire-to-metal seals are made by the radial-compression seal technique. Figure 28 shows diagrams of the three basic types of the radial-compression seal. The diagram on the top left shows a seal assembly in which the seal is made on the outer diameter only. This construction places the ceramic in hoop compression; however, there is induced in the ceramic a longitudinal

\* Registered trade mark.

### Expansion and Elasticity

The choice of materials for use in the radial-compression seal is quite important because the mechanical properties of these materials must serve a definite function. Consider, as an example, the outside seal shown in Figure 28(a). The force maintained by the metal member on the ceramic is maximum at room temperature.

The seals designed for the C-Stellarator vessel insulation are made from a high-alumina ceramic. The flexural strength of the ceramic

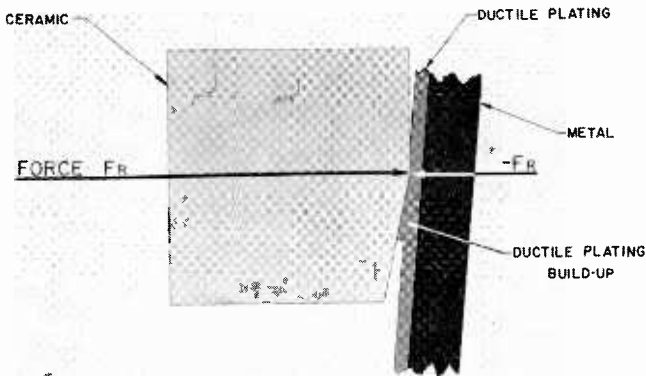


Fig. 30—Cross section of radial-compression seal.

body employed is about 60,000 pounds per square inch. However, high-strength metals suitable for a radial-compression seal have much higher expansion coefficients than the ceramic. It can be shown that the expansion differential between the ceramic and the metal can be compensated for by the elasticity in the metal and ceramic.

Figure 31 shows a stress-strain curve of a high-strength metal which, with some added information, illustrates the behavior of a radial-compression seal during bakeout. Force on the metal caused by the interference fit during the initial sealing process results in an elongation of the metal ring or sleeve to point A on the curve. This point is beyond the yield point of the metal. Although the stress in the metal sleeve at the sealing surface depends on the type of material selected, in this case a typical value of 125,000 pounds per square inch is used. The ultimate strength of the metal is in the order of 160,000 pounds per square inch. The total elongation in the metal sleeve at a stress of 125,000 pounds per square inch is 12 mils at room temperature. The total force at the seal surface of the metal-ceramic interface is about 1000 pounds per linear inch.

If it is assumed that the metal has a greater expansion rate than the ceramic, line ABD, drawn parallel to the elastic portion of the curve, represents the slow release of stress as the temperature is increased. The total elastic strain storage in the metal sleeve at room temperature, represented by line DE, is about 4 mils per inch. Line BC is proportional to the product of the temperature range and the expansion differential. Therefore, if the two materials had identical expansion coefficients, the sealing force would remain constant. Any mismatch in expansion increases length BC and results in a reduction of force at the seal.

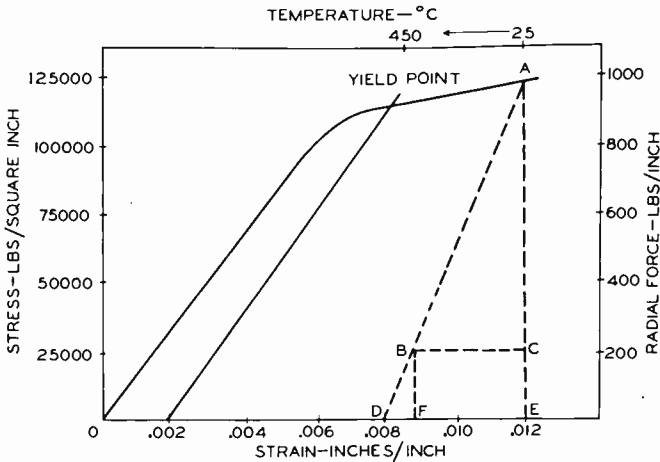


Fig. 31—Stress-strain curve illustrating behavior of a radial-compression seal during bakeout.

The stress in the metal sleeve cannot be permitted to reach zero. Some force must remain to maintain a vacuum-tight seal at the maximum temperature of operation. Because a portion FE of the total strain has been relieved by the differential expansion between the ceramic and the metal as the seal is raised in temperature, the remaining strain in the seal is now DF. This strain must produce sufficient force (for example, 200 pounds per inch) to maintain the seal at this elevated temperature (in this case, 450°C).

The relationship used to determine the requirements at maximum bakeout temperature is as follows:

$$S_c + S_m - \Delta T \Delta C = S_b$$

where  $S_c$  is the unit elastic strain in the ceramic in inches per inch,

$S_m$  is the unit elastic strain in the metal in inches per inch,

$\Delta T$  is the temperature difference in degrees Centigrade,

$\Delta C$  is the expansion coefficient difference per degree Centigrade,

$S_b$  is the minimum value of strain in inches per inch.

This equation shows that the higher the strains, with the resultant stresses, the greater the permissible mismatch in the degree of expansion of the two materials. In these seals, it should be noted that only elastic strains are being considered. The plastic strain is used only to increase the permissible tolerances of the parts, but otherwise serves no function during the temperature cycle.

### Stress

The stress condition within the members requires careful considerations, especially because the longitudinal bending of the cylinder can result in a maximum stress an inch or more away from the metal-ceramic contact. By the proper choice of parameters, these stresses can be minimized. The radial forces in the seal can be determined from the following expression:

$$V_0 = KE\Delta R \left( \frac{t}{R} \right)^{3/2} \frac{1}{(1-r^2)^{1/4}},$$

and therefore maximum bending stress  $X_b$  is given by

$$X_b = \frac{K}{(1-r^2)^{1/2}} \frac{E\Delta R}{R},$$

where  $V_0$  is the radial force in pounds per inch,

$E$  is Young's modulus,

$t$  is the wall thickness,

$R$  is the mean radius,

$\Delta R$  is the change in radius,

$r$  is Poisson's ratio,

$K$  is a constant (dependent on locus or position of loading).

The design parameters for the sapphire window seals are determined in basically the same manner as those used in the construction of the ceramic-to-metal seals. One additional stress encountered in the sapphire seals is buckling. So long as a proper thickness of sapphire is chosen, this stress does not cause any great concern in the design of the seal.

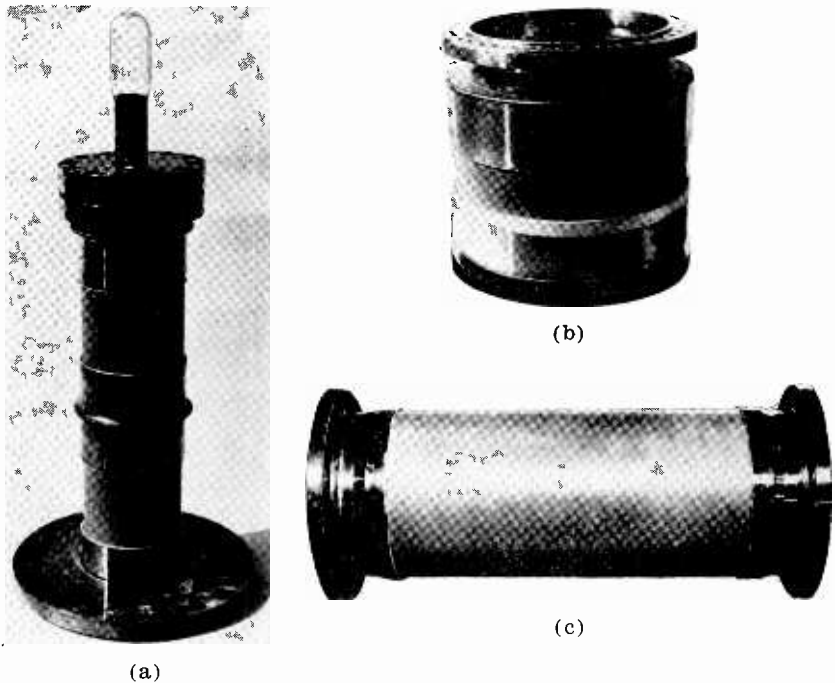


Fig. 32—Various C-Stellarator ceramic-to-metal radial-compression seals: (a) small seal used for gas-injection system and as “stand-off” for ionization gauges; (b) pump-line insulating ceramic assembly; (c) main-vessel insulating ceramic assembly.

### *Seals for the C-Stellarator Vessel*

Figure 32 shows photographs of the various ceramic-to-metal radial-compression seals designed and tested for the C-Stellarator vacuum vessel. Figure 33 shows the three sizes of sapphire radial seals required for the C-Stellarator vessel. All of the seals described in this paper passed severe bakeout tests before being approved for assembly in the vessel. Each assembly was baked to a temperature of  $500^{\circ}\text{C}$  ( $50^{\circ}$  above operating temperature) for one hour. Prototypes

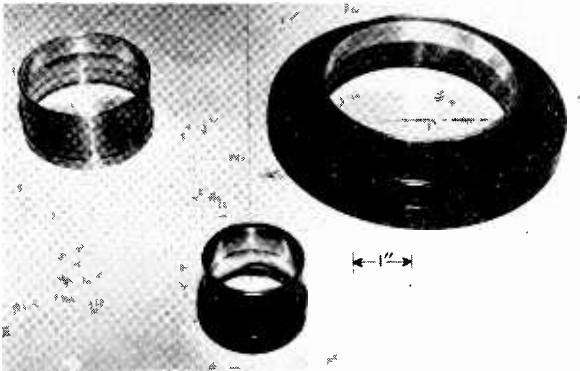


Fig. 33—Three sizes of sapphire radial-compression seals; outside diameters are  $1\frac{3}{4}$ ,  $2\frac{5}{8}$ , and 4 inches.

of these seals have been checked for much longer periods of time at operating temperature. One seal tested was still vacuum-tight at the end of 1200 hours of operation at a temperature of  $450^{\circ}\text{C}$ .

#### *Aperture Limiters for Divertor Simulation*

In final form, the C-Stellarator will utilize a "divertor" which will limit the diameter of the plasma by diverting those magnetic field lines which have a radius greater than a specified value. To simulate the Divertor in initial stages, the pump box contains two "aperture limiters" of different sizes. These molybdenum limiters, shown in Figure 34, are interchangeable and replaceable through a gold-sealed orifice, and feature externally operated adjusting devices for both diameter selection and position selection to facilitate studies of plasma configuration at this point. The three independent movements are

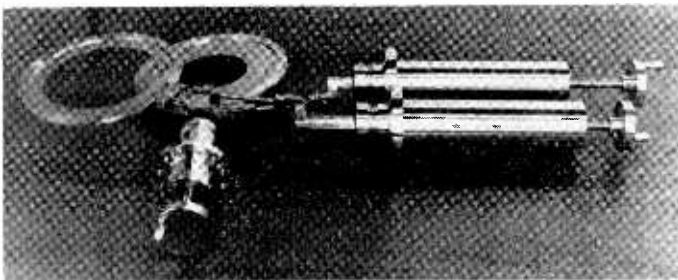


Fig. 34—Molybdenum aperture limiters used for studies of plasma configuration.

precision controlled by handwheels. Vacuum integrity is positive due to the nesting-type expansion bellows within the cylinders.

The molybdenum and sapphire nonlubricated bearings of the limiter assembly are novel in that they allow easy manipulation in high vacuum after the 450°C bake.

A smaller vacuum system, called the gas-injection system, is located adjacent to the main tube and is used to mix and insert experimental gases. This system uses a 2-inch mercury pump and two miniature liquid-nitrogen traps modeled after those of the large systems. It employs 12 Granville-Phillips laboratory-type ultra-high-vacuum valves, and is joined with gold seals. This system, shown in Figure 35, is also baked at 450°C, but in an oven.

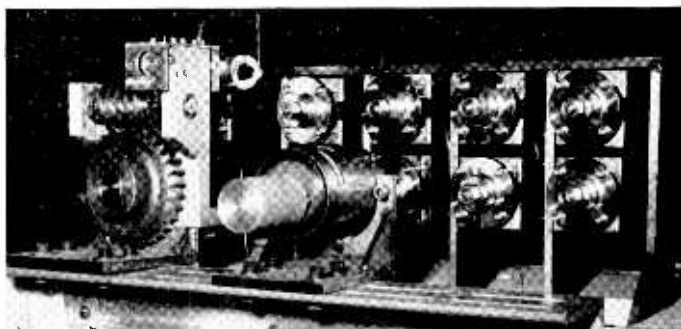


Fig. 35—The gas-injection system. This system is oven-baked to 450° C.

#### *Ultra-High-Vacuum Bakeable Valve*

The large bakeable valve, which is used to isolate the vacuum vessel from the pumping system in emergencies and which can also be used to control the pumping speed, is shown in Figure 36. A portion of the automatic control apparatus is shown in Figure 37. This valve, which has a throat diameter of eight and three quarter inches, has an over-all maximum conductance of about 2100 liters per second when fully open. Because it is bakeable to 450°C, it minimizes the adverse effects of outgassing on the ultimate vacuum of the over-all system. Seal effectiveness was found to be less than  $1 \times 10^{-12}$  standard atmosphere liter per second conductance.

The valve body is basically a stainless steel "T" and is provided with a bellows between the vertical ram shaft and the body. Thin welded joints, slightly flexible, are used to assemble and seal the body and allow rebuilding when required.

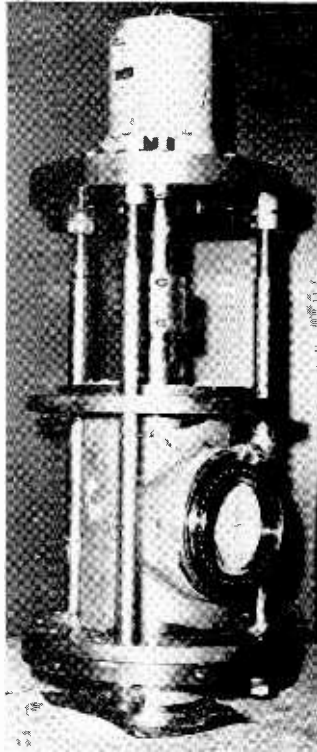


Fig. 36—Large bakeable valve used to isolate the vacuum vessel from the pumping system.

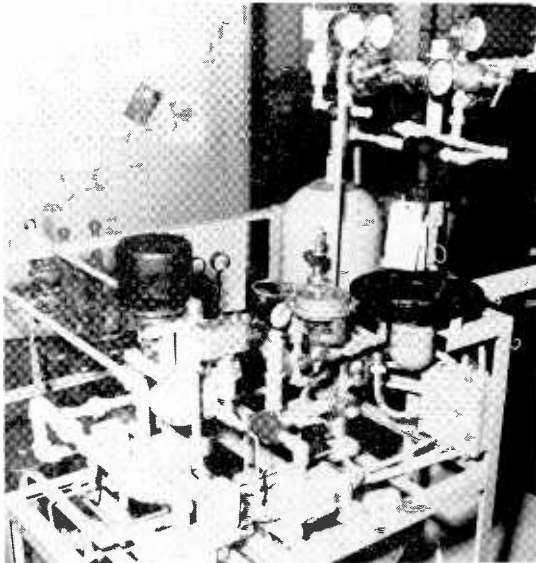


Fig. 37—Automatic control apparatus for the 8-inch bakable valve.

The seat design is novel. Attached to the hydraulically operated ram is a poppet type nose of soft (OFHC) copper which is forced into a circular, stainless steel broaching ring. Slight diameter interference provides for uncovering virgin metal at each closing to effect the seal. Repetitive closures curl the work-hardened metal away in the form of an annular chip. Hundreds of closures were made without deterioration of the valve seat. Chip depth averaged slightly over 2 mils per closure from the full two-inch length of nose available.

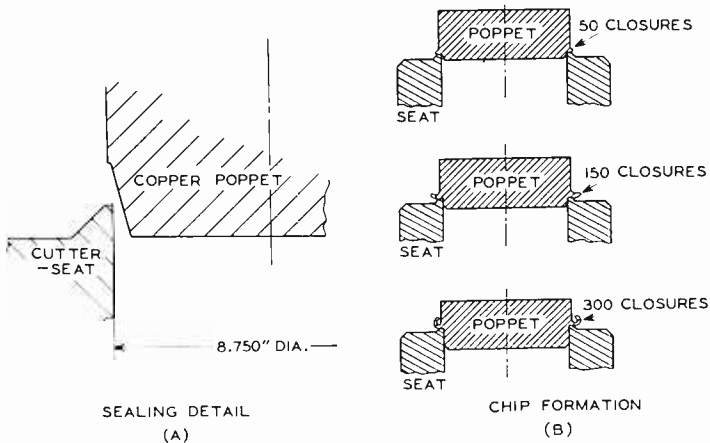


Fig. 38—(a) Sealing detail and (b) chip formation of the valve seat of the ultra-high-vacuum bakable valve.

Figure 38 illustrates design details of the poppet and seat and demonstrates how the seal is achieved and is maintained for many closures. Experiments showed that the relationship of angles, radii, chip thickness, and material properties is extremely critical if seal leakage in the order of  $10^{-12}$  atmosphere liter per second is to be attained repeatedly for hundreds of closures. An average pressure of 53,100 pounds per square inch is developed in the copper of the poppet on closing, and higher local pressures are developed which cause plastic flow and the sealing action.

The valves requires a force of 25 tons to flow metal on closing and a force of 15 tons to hold a seal. These forces are easily obtained from the basic hydraulic system shown in Figure 39.

A friction brake, acting on the hydraulic piston shaft, prevents unwanted closing of the vacuum valve. The brake is required because differential gas pressures acting on the valve poppet and the weight

of moving parts total approximately 700 pounds of unwanted closing force when the valve is under vacuum.

Conductance of the vacuum valve is indicated on a voltmeter which is calibrated in per cent of full conductance. A slidewire voltage divider is mounted on the valve so that position of the shaft coupling sets the indicating voltage.

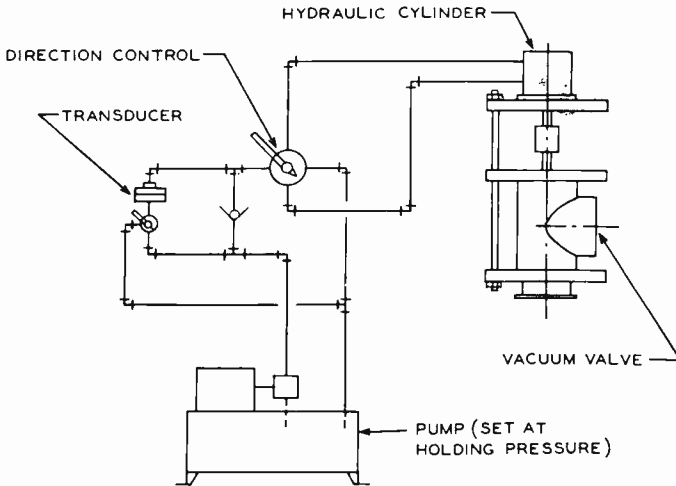


Fig. 39—Hydraulic pressure system used to exert 25 tons closing pressure and fifteen tons holding pressure on the ultra-high-vacuum valve.

#### ASSEMBLY OF THE VESSEL

Component parts for the initial system were assembled by inert-arc-fusion welding to full penetration, allowing no cracks or crevices in the high-vacuum side of the weld. All metal surfaces were machined to a Number 4 finish or better. Prior to assembly, the parts were washed in hot water and a strong household detergent, rinsed thoroughly in hot tap water, rinsed in hot distilled water, and then dried with chemically pure acetone. No commercial degreasing agents were used, and wherever possible machining was done dry without the use of cutting oils.

After assembly and leak-checking by means of a helium mass spectrometer, the welds were dry-hydrogen fired at 1100°C, and then leak-checked again to detect any possible leaks that may have developed as a result of burnout impurities or contaminations. The vessel was not considered leak-tight until the entire system, with the exception of the forepump, could be held at vacuum by the leak-checker with

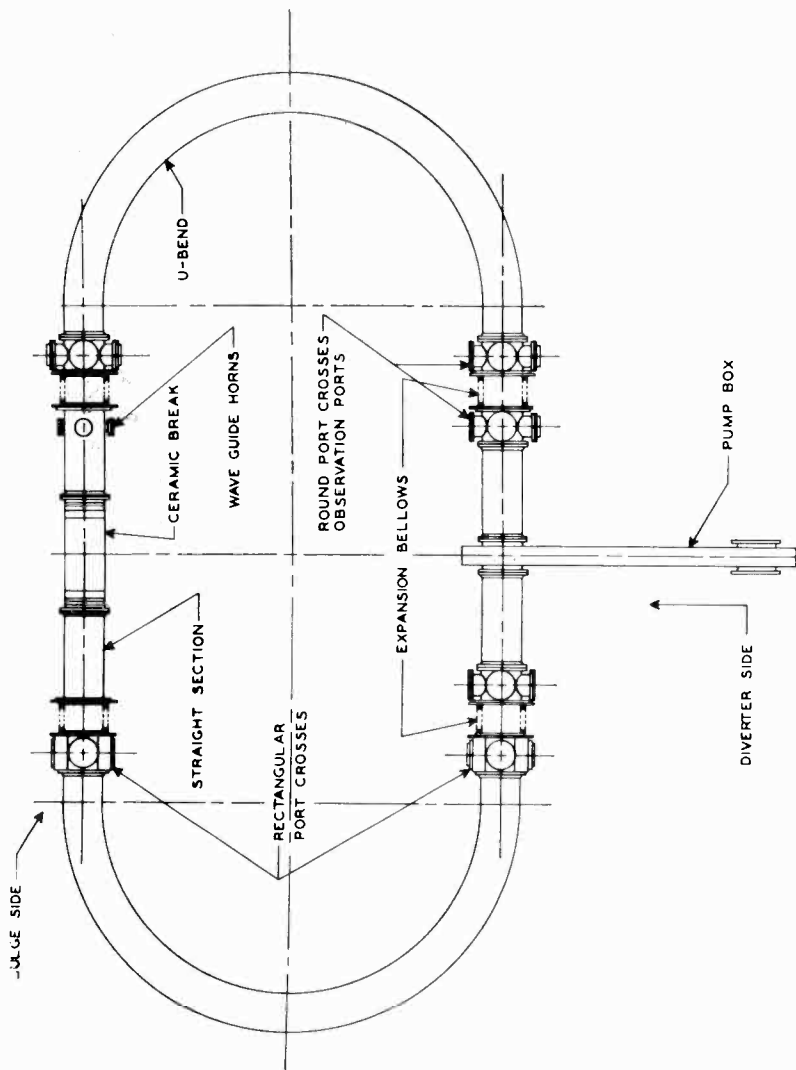


Fig. 40—Line drawing of the first-stage vacuum vessel, showing expansion bellows.

its pump throttled while sections of the machine were "bagged" with sheet rubber, flushed with helium, and allowed to remain flushed for a period of five minutes. It was also found necessary to leak-check periodically while the system was being baked.

The entire vacuum vessel is mechanically secured to the Stellarator base and coils at only one point, the pump box, as shown in Figure 1. Although the vessel is ultimately supported from the Stellarator coils,

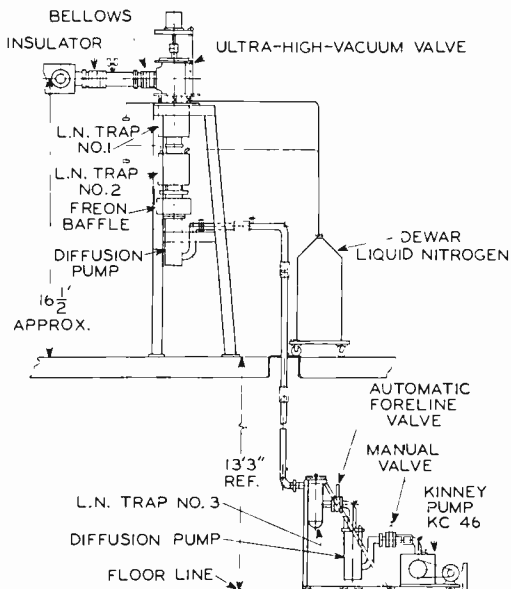


Fig. 41—The ultra-high-vacuum pumping system. Lateral movement is achieved through roller mounting.

an aluminum framework was provided for the initial assembly and test. This additional suspension is provided by six sets of electrically insulated, spring-loaded stainless-steel wire-rope slings which are capable of handling the thermal expansions incident to the bakeout excursions. Measured expansion along the major axis reached 1.2 inches at maximum temperature, while the width increased 0.720 inch.

The dimensions of the vessel after assembly were precise to fractions of an inch as a result of the controls (hot and cold) which were maintained on the "U" bends for flatness, bend radii, and ovality. Length control of the vessel is obtained by a simple adjusting mechanism on each of the four expansion bellows assemblies (Figure 40). These same bellows are provided with counterbored slots for the bolt heads to correct for poor radial orientation of any mating parts. The

suspended pumping system of high-vacuum valve, traps, and diffusion pump rests upon its framework flexibly by a system of rollers to permit lateral movement and a six-spring cushioning platform. This is shown in Figure 41. Figure 42 shows the ultra-high-vacuum portion of the pumping system installed at the Princeton site.

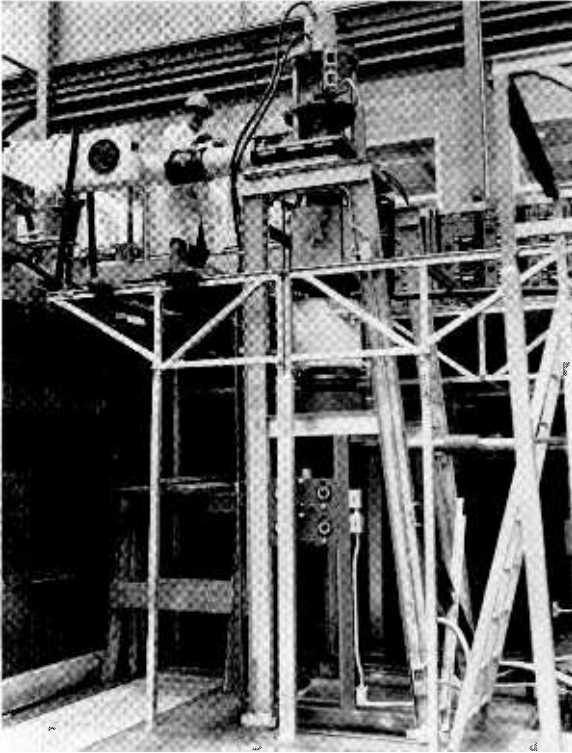


Fig. 42—Actual ultra-high-vacuum system installation at Princeton, N.J.

### CONCLUSION

All design specifications have been met or exceeded for the initial stage of operation. The equipment was successfully tested at Lancaster and is now being installed at Princeton University.

When initial-stage operation has been concluded, the vacuum system will be modified by the addition of a 90-inch-diameter divertor section with 1200-liter-per-second pumping and a 20-inch-diameter ceramic section for crossed-field r-f heating. The addition of these

two components will increase the volume of the vacuum by a factor of approximately 2.

#### BIBLIOGRAPHY

1. L. Spitzer, Jr., "The Stellarator," *Scientific American*, Vol. 199, p. 28, October, 1958.
2. Amasa S. Bishop, *Project Sherwood—The U.S. Program in Controlled Fusion*, Wesley Publishing Co., Inc., Massachusetts, 1958.
3. The following papers appeared in the *Transactions of the 1959 Symposium on Vacuum Technology*, American Vacuum Society, Boston, Mass.: K. Dreyer and J. T. Mark, "Ultra-High Vacuum System Development for the Model C-Stellarator"; W. G. Henderson, J. T. Mark and C. S. Geiger, "Evaluation of Large Diffusion Pumps and Traps for the Ultra-High Vacuum System of the Model C-Stellarator"; and J. E. Martin, J. A. Powell, and J. A. Zollman, "Ceramic, Sapphire, and Glass Seals for the Model C-Stellarator."

# HIGH-FREQUENCY VARACTOR DIODES\*

BY

C. W. MUELLER AND R. D. GOLD

RCA Laboratories  
Princeton, N. J.

*Summary*—Varactor junction diodes are described which give substantially better high-frequency performance than that of any previously available units. Typical electrical characteristics are: capacitance from 0.5 to 1 micromicrofarad, series resistance  $\approx 1$  ohm, and cutoff frequency above 200 kilomegacycles. These diodes have operated as phase-locked oscillators at a signal frequency of 17 kilomegacycles (34 kilomegacycles pump frequency) and in various microwave strip line amplifiers.

Fabrication of these diodes is described. Detailed measurements of the impurity gradient show that it can be approximated by a power law whose exponent is greater than unity. Since this impurity distribution cannot be explained exclusively by the out-diffusion process, an interaction of the alloying and out-diffusion is necessary.

A new thin hermetically sealed ceramic enclosure with a very low inductance (0.6 millimicrohenry) and a low case capacitance (0.3 micromicrofarad) has been developed. The diode may readily be inserted directly into microwave strip transmission line, between the coils of a traveling-wave helix, or into a wave guide.

A method of measuring the diode parameters at 2 kilomegacycles was developed, and a computer used to obtain the desired parameters.

## INTRODUCTION

THE VOLTAGE-VARIABLE capacitance of the semiconductor diode has found increasing use as a tuning element, a low-noise high-frequency amplifier, and a harmonic generator.<sup>1-3</sup> A recent use is as a high-speed computer element by means of subharmonic oscillators.<sup>4,5</sup> Although the desired electrical characteristics of a

\* Manuscript received August 15, 1960.

<sup>1</sup> L. J. Giacoletto and J. O'Connell, "A Variable-Capacitance Germanium Junction Diode for UHF," *RCA Review*, Vol. 17, p. 68, March 1956.

<sup>2</sup> A. Uhler, Jr., "The Potential of Semiconductor Diodes in High-Frequency Communications," *Proc. IRE*, Vol. 46, p. 1099, June 1958.

<sup>3</sup> H. Heffner, "Masers and Parametric Amplifiers," *IRE Wescon Convention Record*, Part 3, Electron Devices, p. 3, 1958.

<sup>4</sup> J. Hilibrand and W. R. Beam, "Semiconductor Diodes in Parametric Subharmonic Oscillators," *RCA Review*, Vol. 20, p. 229, June 1959.

<sup>5</sup> J. Hilibrand, C. W. Mueller, C. F. Stocker, and R. D. Gold, "Semiconductor Parametric Diodes in Microwave Computers," *IRE Trans. on Electronic Computers*, Vol. EC-8, No. 3, p. 287, September 1959.

variable-capacitance diode depend to some extent on the specific circuit application, two requirements common to most circuits are low series resistance and high capacitance-voltage sensitivity. This paper describes the fabrication, resulting impurity distribution, and electrical characteristics of diodes built to satisfy these requirements specifically for optimum performance in ultra-high-speed computer circuits. These diodes have operated in phase-locked-oscillator circuits at a pump frequency of 34 kilomegacycles (17-kilomegacycle signal frequency).<sup>6</sup> Gain has also been observed in a modulation-demodulation circuit using a 34-kilomegacycle carrier.<sup>7</sup>

### FABRICATION

If the design requirements for low series resistance and high capacitance-voltage sensitivity are considered qualitatively, it is clear that a very high impurity concentration is desired outside the depletion-layer region (for low resistance) and a relatively low concentration is desired at the junction (for high capacitance-voltage sensitivity and also for a reasonable reverse breakdown voltage). An analytic treatment<sup>8</sup> of the design requirements has shown that optimum performance is obtained for diodes whose impurity distribution approximates a power law with an exponent between 1 and 2 (i.e.,  $N(x) = ax^b$ , where  $N$  is the impurity concentration at a distance  $x$  from the junction, and  $a$  and  $b$  are arbitrary constants with  $1 < b < 2$ ). Such a diode ( $b > 1$ ) is called "superlinear".

The diode can be characterized by a figure of merit<sup>4,5,8</sup>

$$F = f_{co} S_c = \frac{1}{2\pi r C} \frac{1}{C} \frac{dC}{dV}, \quad (1)$$

where  $f_{co}$  is the diode cutoff frequency (frequency at which the Q of the diode capacitance is unity),  $S_c$  is a measure of the capacitance-voltage sensitivity,  $r$  is the diode series resistance,  $C$  is the depletion-layer capacitance, and  $V$  is the total barrier potential. For convenience in experimental evaluation,  $f_{co}$  and  $S_c$  are defined as

<sup>6</sup> A. H. Solomon and F. Sterzer, "A Parametric Subharmonic Oscillator Pumped at 34.3 KMC," *Proc. IRE*, Vol. 48, No. 7, p. 1322, July 1960.

<sup>7</sup> W. Eckhardt and F. Sterzer, "Microwave-Carrier Modulation-Demodulation Amplifiers and Logic Circuits," to be published.

<sup>8</sup> J. Hilibrand and C. F. Stocker, "The Design of Varactor Diodes," *RCA Review*, Vol. 21, p. 457, September 1960.

$$f_{co} = \frac{1}{2\pi r C_1}, \quad (2)$$

and

$$S_c = \frac{C_1 - C_2}{C_1}, \quad (3)$$

where  $C_1$  and  $C_2$  are the diode capacitances at  $-1$  volt and  $-2$  volts, respectively. Note that  $f_{co}$  is *not* defined in terms of  $C_{\min}$ , the capacitance at breakdown.

Choosing the optimum diode construction involves considerations of the semiconductor material, the fabrication technique, and the encapsulation. The variables governing the choice of material can be formulated in several ways,<sup>9</sup> but the actual difference found between the various available semiconductor materials is not large as long as very-high-temperature operation is not a requirement. However, the choice of the material greatly affects the fabrication techniques. Since maximum speed is a major objective, the high mobility of germanium, for *both* n and p type, together with its simpler fabrication methods, make it a natural choice.

The reduction of series resistance is the most important diode fabrication problem. The d-c resistance, as well as skin-effect loss, must be low at microwave frequencies. The bulk and contact resistances are important because any resistance that can reach 0.1 ohm under some conditions of fabrication is important. The ohmic connection to the base is made with arsenic-doped solder. The high-frequency losses in the metal of the enclosure are kept low by plating with copper and gold. The resistance and inductance of a soldered triangular tab are lower than those of a thermocompression bonded wire.

Because the junction is so thin, a direct measurement of the resistance of this region on a complete diode is difficult. Therefore, special units were made in which the junction was eliminated by making n+ on n-type and p+ on p-type devices of the same size and material, thus eliminating the resistance at the junction and its environs. Measurements showed that a resistance of 0.5 to 0.8 ohm could readily be attained, whereas initial observation of junction diodes had indicated resistances of 5 to 10 ohms. The problem resolved itself into reducing the resistance in and near the junction.

---

<sup>9</sup> D. A. Jenny, "A Gallium Arsenide Microwave Diode," *Proc. IRE*, Vol. 46, No. 4, p. 717, April 1958.

The ideal configuration would be a capacitive region, in which the doping concentration varies, supported by two regions of zero resistance. In practice, however, the regions must be joined and do influence each other. Also, a part of the capacitive region adds to the resistive region during the low-voltage part of the cycle. In the regions adjacent to the junction, therefore, the effects of capacitance, resistance, breakdown, and contact potential become interrelated in their dependence on impurity concentration. The optimum doping profile, as previously pointed out, is a superlinear variation of the impurity concentration. This doping profile is obtained near the junction by outdiffusion from a highly doped wafer and subsequent alloying at low temperature. Of the several fabrication methods which have been used, only the method giving the highest-cutoff-frequency units is described below.

A base wafer of  $2 \times 10^{18}$  antimony atoms per cc is out-diffused by heating for one hour at  $900^{\circ}\text{C}$  in a reducing atmosphere. This produces an out-diffused layer of about 0.2 mil. The diffused layer on one side is removed by etching. A 2-mil dot of indium containing 0.5 per cent gallium is alloyed to the outdiffused side of the wafer at  $300^{\circ}\text{C}$  to form a junction on the germanium. The pointed metal tab is connected to the dot and the unit is etched. The high impurity density used in these diodes results in a very low reverse current. Typical reverse currents at  $-2.5$  volts are 0.1 microampere at room temperature, 4 microamperes at  $65^{\circ}\text{C}$ , and 10 microamperes at  $100^{\circ}\text{C}$ . With these low currents, it is evident that the "shot noise" will be very small when these diodes are used in parametric amplifiers.

The encapsulation is an important part of varactor construction. In a very-high-frequency circuit, the diode case becomes part of the circuit and a good encapsulation is necessary before reproducible measurements can be made. The diode enclosure must have low lead inductance and low shunt capacitance (i.e., small energy storage in the case), and must be hermetically sealed. For the particular application mentioned earlier, it was also necessary that the diode fit directly into a strip-type transmission line. Figure 1 shows a cross-sectional view of the completed structure. The lead inductance is about 0.6 millimicrohenry; case capacitance is about 0.3 micromicrofarad; and case losses at 2 kilomegacycles are equivalent to about 0.15 ohm series resistance. Figure 2 shows the parts and assembly of the diode enclosure.

#### IMPURITY DISTRIBUTION

As stated previously, the impurity distribution in the vicinity of the junction is very important for high-frequency varactor diodes. To

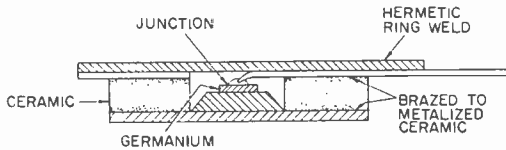


Fig. 1—Cross section of diode.

determine this distribution experimentally in completed units, a precise capacitance-voltage measurement was made. The impurity concentration has been shown<sup>10</sup> to be inversely proportional to  $d(1/C^2)/dV$ , and this method was used to determine impurity profiles of alloy junctions to within ten per cent and actual impurity levels to within twenty per cent.<sup>11</sup>

The results of this experiment are interesting for two reasons.



Fig. 2—Varactor diode parts and assembly.

<sup>10</sup> W. Schottky, "Vereinfachte und erweiterte Theorie der Randschichtgleichrichter," *Z. Physik*, Vol. 118, p. 539, 1941-42.

<sup>11</sup> J. Hilibrand and R. D. Gold, "Determination of the Impurity Distribution in Junction Diodes from Capacitance-Voltage Measurements," *RCA Review*, Vol. 21, No. 2, p. 245, June 1960.

First, they verify that the highest-frequency diodes result when the doping follows a superlinear law. Second, they show that alloying a small dot at low temperature to a highly doped out-diffused base wafer results in an impurity profile which cannot be explained by the usual outdiffusion model.

Several investigators have reported on the out-diffusion of antimony from germanium.<sup>12-14</sup> Figure 3 shows the expected impurity distribution in an out-diffused base wafer under different time and temperature conditions. These curves are based on the diffusion constant and evaporation-rate constant of Smits and Miller.

It is important to note that the maximum slope of each curve (on a log plot) varies from 0.3 to 0.9. The evaporation-rate constant of Smits and Miller used in the two upper curves of Figure 3 was determined by outdiffusing into a vacuum, whereas in the varactor diodes

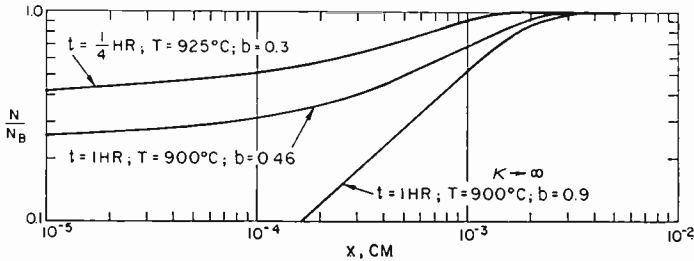


Fig. 3—Expected impurity distribution in antimony out-diffused base wafers (after Smits and Miller).

described here the out-diffusion was into flowing nitrogen containing 10 per cent hydrogen. The exact rate constant under these conditions was not determined. Use of a different rate constant would not alter these curves appreciably, however, for even if an infinite evaporation rate constant is assumed, the resulting bottom curve of Figure 5 has a slope of only 0.9. In fact, the usual out-diffusion process cannot yield a slope greater than unity.

Figure 4 shows a diode impurity distribution which appears to

<sup>12</sup> F. M. Smits and R. C. Miller, "Rate Limitation at the Surface for Impurity Diffusion in Semiconductors," *Phys. Rev.*, Vol. 104, p. 1242, December 1, 1956.

<sup>13</sup> R. C. Miller and F. M. Smits, "Diffusion of Antimony out of Germanium and Some Properties of the Antimony-Germanium System," *Phys. Rev.*, Vol. 107, p. 65, July 1, 1957.

<sup>14</sup> K. Lehovc, K. Schoeni, and R. Zuleeg, "Evaporation of Impurities from Semiconductors," *Jour. Appl. Phys.*, Vol. 28, No. 4, p. 420, April 1957.

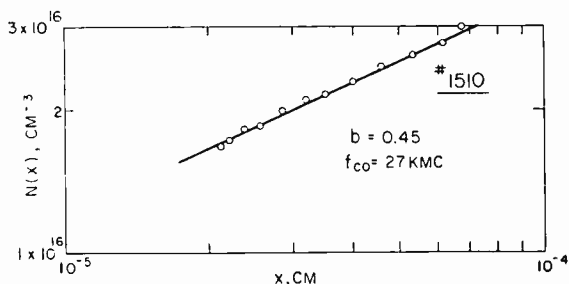


Fig. 4—Impurity concentration as a function of  $x$ : initial bulk concentration  $2 \times 10^{17}$  Sb atoms/cc; out-diffusion for one hour at  $900^\circ\text{C}$ ; dot alloyed at  $300^\circ\text{C}$  for approximately 15 seconds.

obey the above out-diffusion theory. The initial bulk concentration here was  $2 \times 10^{17}$  antimony atoms per cc. The wafer was out-diffused for one hour at  $900^\circ\text{C}$ , and a dot was alloyed at  $300^\circ\text{C}$  for about 15 seconds. Note that for this particular initial bulk concentration, the slope of the impurity distribution is less than unity, and is, in fact, in good agreement with that expected from the out-diffusion calculations shown in Figure 3. The measured cutoff frequency of this unit is only 27 kilomegacycles.

Figure 5 shows the distribution resulting from somewhat different out-diffusion conditions. The initial concentration was  $2 \times 10^{18}$  antimony atoms per cc, and out-diffusion was for 15 minutes at  $925^\circ\text{C}$ .

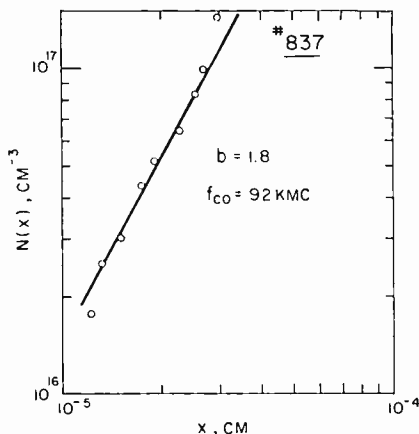


Fig. 5—Impurity concentration as a function of  $x$ : initial bulk concentration  $2 \times 10^{18}$  antimony atoms per cc; out-diffusion for 15 minutes at  $925^\circ\text{C}$ ; dot alloyed as in Figure 4.

Alloying was about the same as before, 15 seconds at 300°C. Note that here the slope is 1.8, twice the maximum possible from ordinary out-diffusion, and several times greater than that expected for the out-diffusion time and temperature used. It is believed that the recrystallization process for rapid, low-temperature alloying of a small dot to a highly doped base wafer results in a modification of the impurity distribution near the junction. The cutoff frequency for this unit is 92 kilomegacycles.

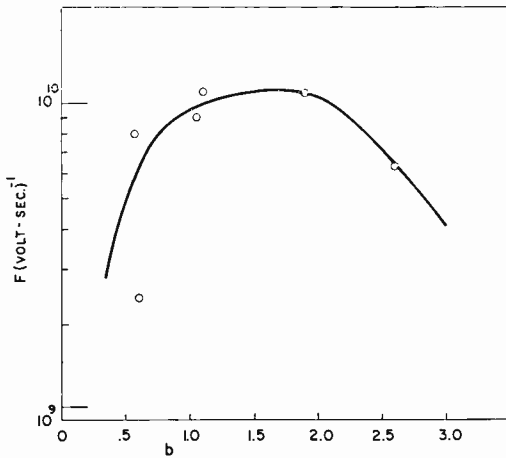


Fig. 6—Diode figure of merit versus impurity distribution exponent.

The higher cutoff frequency can be attributed, in part, to the higher bulk concentration, but measurements showed that this is not sufficient to explain the large increase observed, especially since the capacitance per unit area is increased relative to that shown in Figure 4. The importance of the impurity gradient is shown in Figure 6. Here the figure of merit,  $F$ , is plotted against impurity slope for a group of diodes with the same bulk concentration,  $2 \times 10^{18}$  antimony atoms per cc. The results are in good agreement with the analysis of Hili-brand and Stocker.<sup>3</sup> The general shape can be explained qualitatively by the fact that  $f_{co}$  increases while  $S_c$  decreases for increasing values of  $b$ . It should also be pointed out that diodes having cutoff frequencies on the order of 200 kilomegacycles have been made with this out-diffusion and alloying process. Detailed impurity gradient measurements were not made of the higher-cutoff-frequency units because the accuracy decreases for the smaller-capacitance units.

Table I compares the cutoff frequency of a group of abrupt-junction diodes with a group of out-diffused diodes. Both groups were designed to have about the same breakdown voltage, and a capacitance of 1 micromicrofarad at  $-1$  volt. One can see the large improvement in series resistance for the out-diffused diode and the corresponding increase in cutoff frequency. Although the capacitance-voltage sensitivity is somewhat lower for the out-diffused structure, the advantage gained in series resistance is much more important. The last column, which shows the combined figure of merit as defined in Equation (1), indicates an improvement by a factor of 6.

Table I—Effect of Out-Diffusion on Electrical Characteristics for Diodes with the Same Breakdown Voltage

	Base wafer	$V_{Br}$ (at 1 ma)	$C^*$ ( $\mu\mu f$ )	$r^*$ (ohms)	$f_{co}^*$ (kmc)	$F^*$	$S_r^*$
No							
Outdiffusion—	$6.8 \times 10^{16}$ Sb	6.5	.9	10.2	18	.21	3.8
Outdiffused —	$2.7 \times 10^{18}$ Sb	7.5	1.15	.95	150	.15	22.5

\*  $r$ ,  $C$ ,  $f_{co}$  are evaluated at  $-1$  volt bias;  $S_r \approx (C_1 - C_2)/C_1$ ,  $F = f_{co} S_r$ .

It is clear that the combination of out-diffusion from highly doped germanium and rapid low-temperature alloying of a small dot to the out-diffused surface results in a considerable improvement over what can be obtained from simple alloying, due to the resulting high impurity gradient.

#### ACKNOWLEDGMENT

The help of Mrs. E. Moonan and A. W. Fisher in making the diodes and the measurements and the many helpful discussions with J. Hilibrand and C. F. Stocker are gratefully acknowledged.

#### APPENDIX — ELECTRICAL MEASUREMENTS

The diode can be represented by the equivalent circuit shown in Figure 7. Here,  $C(V)$  is the voltage-sensitive depletion-layer capacitance,  $r_d$  is the series resistance loss of the semiconductor, and  $G(V)$  is the voltage-sensitive diode conductance. For reverse-bias voltages below breakdown,  $G(V)$  is usually negligible. The diode case is represented by a lead inductance  $L$ , a case capacitance  $C_c$  and a resistance

$r_c$  which represents losses in the case.\* To characterize a diode completely, it is necessary to evaluate each element of this equivalent circuit and to determine the reverse breakdown voltage.

The diode capacitance and case capacitance are easily measured at 1 megacycle with a precision capacitance bridge, using a dummy open (a diode with the tab lifted off the alloy dot) for case capacitance. Lead inductance and case losses were determined from coaxial-line standing-wave measurements at 2 kilomegacycles on a dummy short (a diode case with copper replacing the germanium wafer), referenced to an essentially "perfect" short. The breakdown voltage was measured

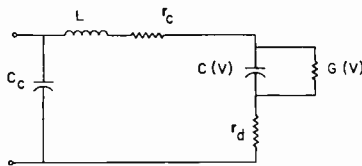


Fig. 7—Equivalent circuit of encapsulated diode.

on a transistor current-voltage curve tracer. The measurement problem therefore was essentially to determine  $r_d$ . This was difficult because at microwave frequencies  $r_d$  is much smaller than the reactance in series with it.\*\*

Several workers have measured the losses in varactor diodes by means of a transformation method.<sup>15,16</sup> Although this method is fairly simple, it does not separate the semiconductor and case losses. During the development of a new device, it is desirable to have a separate measure of these two losses. The method chosen was to measure the diode impedance on a coaxial slotted line (frequency = 2 kilomegacycles) and to calculate  $r_d$  from the known values for the equivalent

\* For evaluating device processing techniques, Equations (1) and (2) use  $r = r_d$ . For circuit studies, however,  $r = r_d + r_c$  is used.

\*\* A fixed frequency measurement was desirable. The variation of  $C_D$  from unit to unit made it impossible to simply resonate  $L$  with  $C_D$ . External reactive elements (e.g., shorting stubs) could not be conveniently used because they introduced a variable loss which is comparable to the diode losses.

<sup>15</sup> N. Houlding, "Measurement of Varactor Quality," *Microwave Jour.*, Vol. 3, No. 1, p. 40, January 1960.

<sup>16</sup> R. I. Harrison, "Parametric Diode Q Measurements," *Microwave Jour.*, Vol. 3, No. 5, p. 43, May 1960.

circuit after correcting for line and fixture losses. This allows a separate determination of  $r_d$  and  $r_d + r_c$ . It is important to recognize that such a "lumped constant" treatment at 2 kilomegacycles is possible only because the diode encapsulation is sufficiently small compared with the wavelength, and the relative position of the parts of the enclosure are accurately reproduced in all units. This method is accurate for diodes with cutoff frequencies up to 200 kilomegacycles. The calculation for  $r_d$  is performed on a digital computer.

# A PLUG-TYPE IMAGE ORTHICON TARGET\*

BY

STEFAN A. OCHS

RCA Laboratories,  
Princeton, N. J.

*Summary*—A new structure-type target for image-orthicon camera tubes has been investigated in the laboratory. It consists of an array of metal plugs embedded in an insulating film of aluminum oxide.

Several experimental image orthicons containing such targets, in a 750- or 1000-mesh pattern, have been made. These tubes show very little or no image retention ("sticking"), either initially or after extended operation, and they perform well over a wide range of target temperatures. Due to the high resistance between elements, the plug-type target can store a high-resolution picture for a long time.

Camera tubes containing plug-type targets are particularly useful for viewing low-light-level scenes, possibly at reduced scanning rates.

## INTRODUCTION

THE MOST widely used camera tube in modern television broadcasting, as well as in many noncommercial applications, is the image orthicon.<sup>1-3</sup> Its high sensitivity derives from the following significant features: an efficient photocathode, electron-image multiplication and storage at the target, and inclusion of a signal multiplier.

A cross-sectional view of the image orthicon is given in Figure 1. Light from the scene is focused onto the photocathode and causes the emission of photoelectrons. The resultant electron stream is imaged onto the semiconducting target, which is stabilized near gun-cathode potential by the low-velocity scanning beam. Each photoelectron strikes the target with an energy of about 400 electron-volts and ejects, on the average, about four secondary electrons. These are collected by a fine-mesh metal screen which is mounted close to the

---

\* Manuscript received November 7, 1960.

<sup>1</sup> A. Rose, P. K. Weimer, and H. B. Law, "The Image Orthicon—A Sensitive Television Pickup Tube," *Proc. I.R.E.*, Vol. 34, p. 424, July, 1946.

<sup>2</sup> R. B. Janes, R. E. Johnson, and R. S. Moore, "Development and Performance of Television Camera Tubes," *RCA Review*, Vol. 10, p. 191, June, 1949.

<sup>3</sup> V. K. Zworykin and G. A. Morton, *Television*, Second Edition, Chapter 10, p. 347, John Wiley & Sons, Inc., New York, N. Y., 1954.

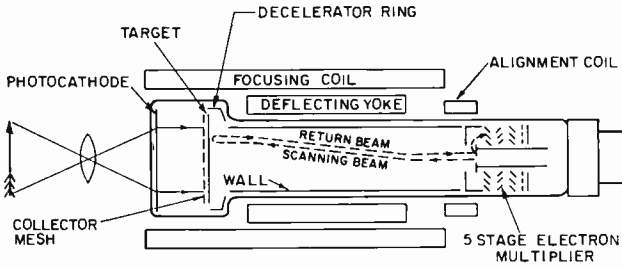


Fig. 1—Image orthicon.

target and held a few volts above cathode potential. On the target, therefore, a pattern of positive charge results which is a replica of the optical image projected onto the photocathode.

This charge image is neutralized by the low-velocity beam which scans the target. After a sufficient number of electrons has landed on any elemental area to return it to its equilibrium potential, excess beam electrons are reflected and return, approximately along their previous trajectories, toward the gun. There they strike the first dynode of the electron multiplier. As the "return beam" is modulated through subtraction by the charge pattern on the target, the output signal of the multiplier will also represent this pattern.

The "two-sided" target must satisfy two conditions: (1) It has to be sufficiently conductive across its thickness so that the positive charge due to the photo-electrons and the corresponding negative charge deposited by the beam on the other side, will combine and cancel out within a frame time. (2) Its lateral resistance must be so high that the definition of the charge image stored on the target is not deteriorated excessively due to lateral leakage.

This paper describes work done on an experimental image-orthicon target which consists of an array of metal plugs (to provide the desired transverse conductivity) embedded in an insulating film of aluminum oxide (to prevent lateral leakage). The basic construction is indicated in Figure 2. Such an anisotropically conductive target

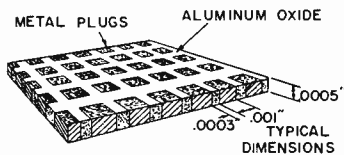


Fig. 2—Section of plug target.

can be expected to operate over a wide temperature range and to be able to store high-resolution patterns for extended times. Early work on plug targets is described by Zworykin and Morton.<sup>4</sup>

### ANODIZATION

Since anodization of aluminum plays a significant part in the fabrication of this target, it is appropriate to describe this technique. When a sheet of aluminum is anodized in an electrolyte (such as sulfuric, phosphoric, oxalic, or chromic acids) which dissolves aluminum oxide, a porous oxide coating is formed. In other electrolytes (e.g., ammonium citrate, tartrate, or borate solutions) nonporous oxide layers are formed.<sup>5</sup> In both cases a zone of nonporous oxide, or "barrier layer," is formed adjacent to the metal. This layer grows to a final thickness which is a function of the electrolyte and proportional to the anodization potential (~14 angstroms per volt). The barrier layer under a porous film usually is of the order of 100 angstroms thick while nonporous films (which consist exclusively of the barrier layer) typically are a few hundred to several thousand angstroms thick. The total thickness of porous films generally is many times that of the barrier layer and depends primarily on the anodization time. The pores are holes, a few hundred angstroms in diameter, which are approximately perpendicular to the aluminum surface. The spacing of the pores is fairly uniform, though irregular, with the walls between the pores of about the same thickness as that of the barrier layer.<sup>6,7</sup> Figure 3 gives a schematic presentation of the structure of nonporous and porous anodic oxide coatings.

Self-supporting films can be formed of both types of these anodic coatings by removing the oxide layer on the opposite side as well as the metallic aluminum.

### PLUG-TYPE TARGETS

The excellent regularity which is achieved in the mesh of electroformed screens suggested that a related technique, also based on

---

<sup>4</sup> See pp. 352-354 in reference 3.

<sup>5</sup> G. Hass, "On the Preparation of Hard Oxide Films with Precisely Controlled Thickness on Evaporated Aluminum Mirrors," *Jour. Opt. Soc. Amer.*, Vol. 39, p. 532, July, 1949.

<sup>6</sup> F. Keller, M. S. Hunter, and D. L. Robinson, "Structural Features of Oxide Coatings on Aluminum," *Jour. Electrochem. Soc.*, Vol. 100, p. 411, September, 1953.

<sup>7</sup> M. S. Hunter and P. Fowle, "Determination of Barrier Layer Thickness of Anodic Oxide Coatings," *Jour. Electrochem. Soc.*, Vol. 101, p. 481, September, 1954.

patterns generated by a ruling engine, might yield a structure target of the degree of uniformity needed for a high-quality tube.

Of the two kinds of anodic aluminum oxide, the porous type is particularly suitable as the insulating matrix of a plug-type target. It can be made into thicker and therefore stronger films than the nonporous coating. Also, its porosity permits very much more effective use of etching resists.

As indicated in Figure 2, the structure which was developed consists of a rectangular array of nickel plugs inserted in a film of porous aluminum oxide. The dimensions shown are typical for a 750-mesh target. Such targets are produced by the following method.

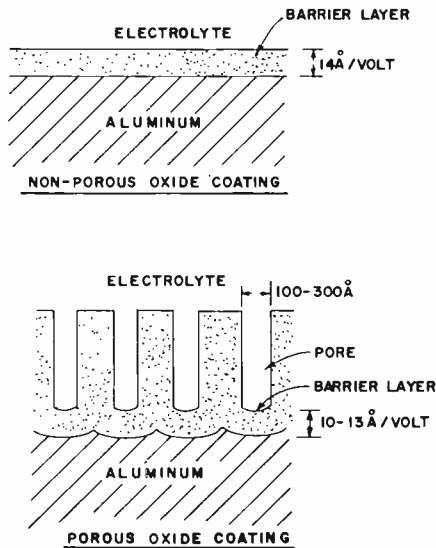


Fig. 3—Anodic aluminum oxide coatings.

The base material is a sheet of aluminum, eight to twelve mils thick, which is anodized to form a porous oxide film of about one-half mil thickness. After the piece has been rinsed and dried, a thin film of Kodak Photo Resist\* (KPR) is applied to one side. This coating material is an organic-solvent solution of a light-sensitive plastic which, after exposure to ultra-violet radiation, resists the action of many acids and alkalis. It can be applied in thicknesses of less than 0.01 mil and apparently is free of grain. The exposure is made through

\* Registered trade mark.

a suitable mask which is held in close contact with the KPR-coated surface. The mask consists of a pattern of opaque squares obtained by making a photographic negative of an engine-ruled master bearing an electroformed mesh. After the photoresist has been developed, a mesh pattern of exposed resist is left on the aluminum oxide surface.

The oxide is then removed where not protected by the resist. Due to the pore structure of the oxide, the etchant penetrates the layer rapidly. Therefore very little under-cutting occurs during the time necessary for exposing the aluminum base material.

After the etch, the piece is immersed in a nickel-plating bath and nickel is deposited onto the aluminum where it is exposed in the openings of the mesh pattern. In a typical case the plating is continued until the level of the nickel reaches that of the oxide surface (Figure 4). However, the process can be controlled to yield nickel plugs which stay below the surface of the oxide or extend above it.

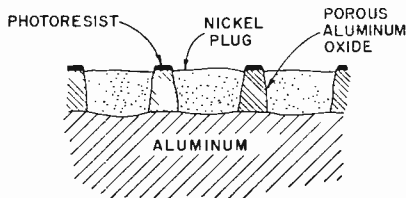


Fig. 4—Cross section of oxide coating containing nickel plugs.

After the KPR has been removed, the piece is covered with a protective lacquer except for an area on the reverse side (Figure 5A). The oxide layer in this exposed area is then etched off (Figure 5B) after which the underlying aluminum is removed (Figure 5C). Finally, the lacquer is removed. This leaves a self-supporting film of aluminum oxide which contains an array of nickel plugs and is held in a frame of anodized aluminum sheet (Figure 5D). This film is then removed from its aluminum frame and mounted on a suitable support ring.

#### PERFORMANCE OF PLUG-TYPE TARGET

Many image orthicons containing plug-type targets, mostly with 750 or 1000 plugs per linear inch, have been made. Although some earlier tubes exhibited a certain amount of "sticking" (as discussed below), in later tubes practically no image-retention was observed, either initially or after extended operation.

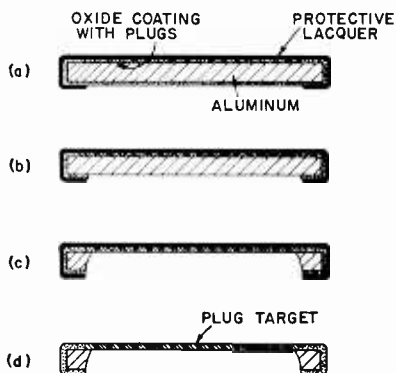


Fig. 5—Cross section of piece during production of plug target.

The pictures produced by early targets had shown a marked degree of graininess, but this has been reduced considerably in later tubes as a result of a great improvement in plug definition. However, most targets have blemishes which are due to surface imperfections of the original aluminum foil. These picture defects are not sufficiently pronounced to limit the resolution attainable, but do present a problem which has to be solved before such tubes will be acceptable for commercial broadcasting.

Figure 6 shows a small magnified area of an actual target with 750 plugs per inch. This target, as well as the plug target included in the image orthicon used in obtaining Figures 7-10, were made by

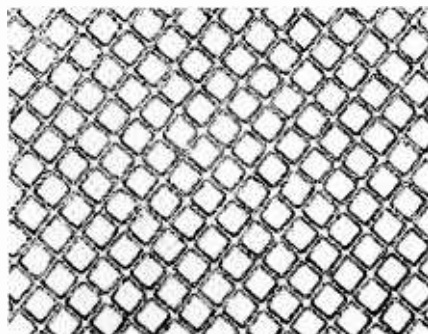


Fig. 6—Photomicrograph of plug-type target.

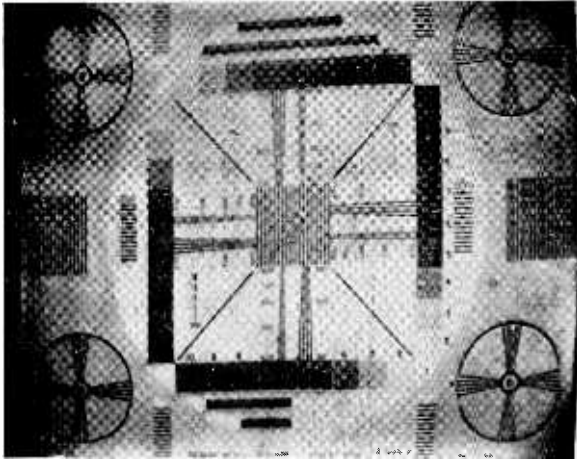


Fig. 7—Picture produced by image orthicon with plug target.

R. L. Van Asselt.\* Figures 7 and 8 are reproductions of pictures produced by an image orthicon containing an experimental plug target. In both cases the same kinescope area was photographed. In Figure 7 the target was scanned in the regular fashion, while in Figure 8 it

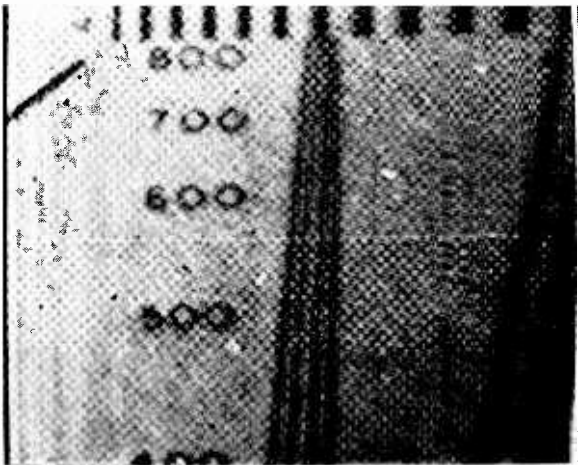


Fig. 8—Picture produced by underscanning plug target.

\* RCA Electron Tube Division, Lancaster, Pa.

was greatly underscanned, so that the individual plugs were resolved. The size of the optical pattern projected onto the photocathode was the same for both pictures.

Figure 9 shows an experimental curve of limiting resolution as a function of photocathode illumination for the same image orthicon. Also shown is the corresponding characteristic for a 6849 image orthicon, which contains a glass target having approximately the same capacitance (relative to the collector mesh) as that of the plug-target tube.

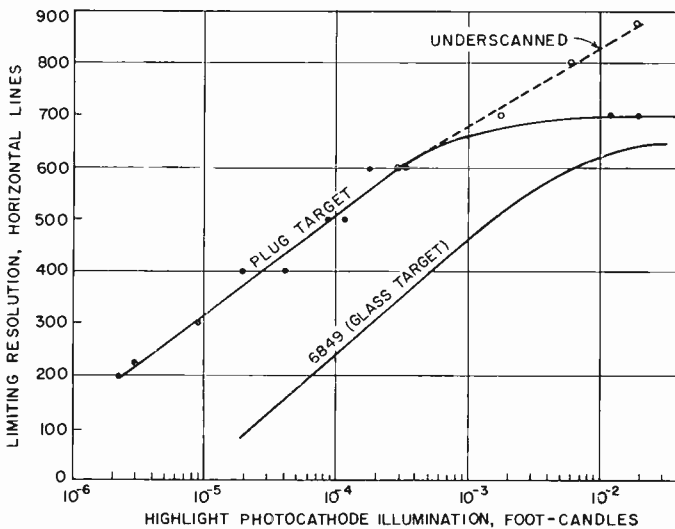


Fig. 9—Limiting resolution versus photocathode illumination.

The photocathode in the plug-target tube has a sensitivity of 67 microamperes per lumen. This is quite similar to the average sensitivity of the photocathode in a commercial tube. Therefore, a comparison of the curves shown in Figure 9 gives a meaningful indication of the relative characteristics of the experimental plug-type target and a conventional glass target. The superior performance of the experimental plug target at low light levels is primarily due to its highly anisotropic conduction properties. The high interelement resistance permits full frame-time storage of charge (on those elements which correspond to illuminated regions of the scene) without the loss of resolution which would attend an excess of lateral leakage.

Due to the limitations in the equipment with which the resolution tests were made, resolutions above 700 lines could not be observed under standard scanning conditions. Therefore, the target was under-scanned so that a given resolution pattern stored on the target would correspond to a lower signal frequency to be displayed on the kinescope. The dashed curve of Figure 9 shows the limiting resolution measured in this fashion. The characteristics of the 6849 were obtained from a system of 9 megacycles bandwidth, which corresponds to a resolution of about 700 television lines.

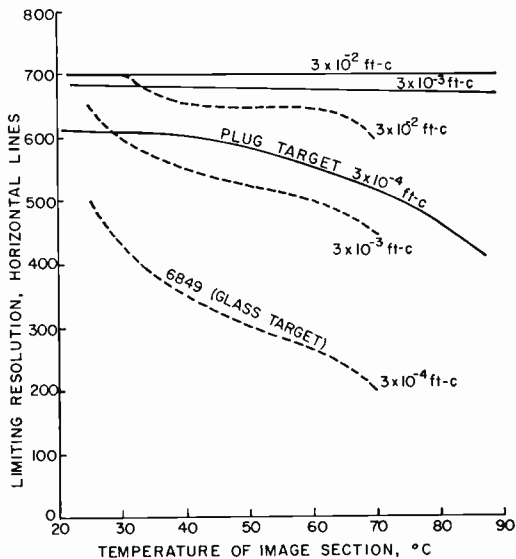


Fig. 10—Effect of image-section temperature on limiting resolution.

The effect of the image-section temperature on limiting resolution is shown in Figure 10 for three different levels of photocathode illumination. The performance of the plug-target tube again is compared to the data for the 6849 image orthicon with a conventional glass target. The resistivity of the aluminum oxide which separates the nickel plugs in the plug-type target should be so high that the resolution remains unaffected by moderate temperature changes. Presumably the decline in resolution which is seen is due to lateral leakage caused by surface contamination of the target. A possible cause of this surface leakage is the cesium vapor which is used in the activation of the photocathode.

An experimental image orthicon containing a plug-type target was operated intermittently for a total of 3,500 hours. The operation of the tube remained satisfactory and relatively stable, except that after about 1,300 hours the target showed a small amount of "sticking," i.e., after a change in the scene, an after-image of the original (but of opposite polarity) was produced. This effect did not grow worse with additional tube operation. It was produced by the aluminum-oxide mesh whose surface became more insulating during operation of the tube (due to a progressive cleaning-up) causing the aluminum oxide to charge up in the regions corresponding to illuminated areas of the optical image and, by coplanar-grid action (on the scanned side of the target), producing negative-polarity after-images. In later tubes, with targets which (due to better definition of the plug structure) had smaller exposed oxide areas, much less sticking was observed.

At the same time that the above-described sticking occurred, the target was found to be capable of storing an image for a much longer time than when the tube was new. A pattern with several hundred lines of resolution could be stored for over a minute (in some regions of the target). This test was made by projecting, for a short time, an optical image onto the photocathode of the tube while the scanning beam was off. Then, after the desired storage time was over, the beam was turned on and the picture obtained on the first scan was photographed. This storage ability of the plug target makes it useful for operation with long frame times.

#### COMPOSITE MESH-TARGET STRUCTURES

The geometry of the plug target lends itself to the production of a structure which consists of the target itself and a "built-in" mesh. As indicated in Figure 11, this composite unit carries the collector mesh in a fixed position relative to the target plugs. The capacitance between the plugs and the collector mesh can be controlled through (1) the spacing between the plane of the mesh and the top surfaces of the plugs (distance  $a$  in Figure 11), and (2) by having the mesh extend a predetermined distance  $b$  down the walls of the holes.

In this arrangement, since the collector mesh prevents photoelectrons from reaching the insulating regions between the plugs, the "sticking" effect described in the preceding section will be avoided. However, the chief advantage of such a mesh-target structure is that it prevents the occurrence of "microphonics." This effect consists of a moving pattern of signal modulation superposed on the desired

output picture when the tube is exposed to shocks or vibration. Microphonics are due to the relative motion of target and collector mesh—both acting like thin, edge-supported membranes—causing time-dependent variations of the storage capacitance across the target area and resulting in corresponding variations of signal output.

A few laboratory models of the composite mesh-target structure have been made. An image orthicon containing such a target which was operative over part of its area, was found to perform in the expected fashion. It did not show sticking and was free from

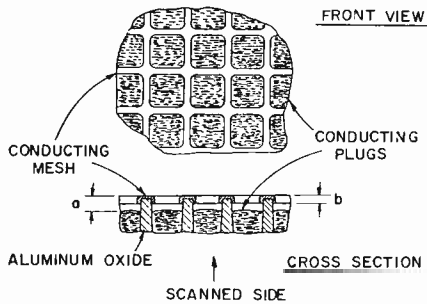


Fig. 11—Plug target with integral collector mesh.

microphonics. Its resolution capability was similar to that of a tube containing a simple plug target. At low light levels the effects of capacitive lag were observed, as expected in a tube with a very close target-to-mesh spacing.

Since the completion of the work described in this paper Day, Hannam and Wargo<sup>8</sup> have reported on a plug-type storage target which consists of an insulating glass or ceramic matrix containing metal plugs and carrying conducting meshes on one or both sides. These targets are made from an insulating screen made by the FOTOFORM\* process of the Corning Glass Company. The development of the plug target described in the present paper was based on the use of anodic aluminum oxide because it lends itself to the production of relatively fine mesh and because of the simple manner in which metal plugs can be electroplated onto the underlying aluminum base material.

<sup>8</sup> H. R. Day, H. J. Hannam, and P. Wargo, "Targets for Storage and Camera Tubes," *Trans. I.R.E. PGED*, Vol. ED-7, p. 78, April, 1960.

\* Registered trade mark.

## CONCLUSIONS

An experimental plug-type image-orthicon target has been developed which is capable of yielding high resolution at relatively low light levels. Its useful life has been shown to be very long and the target was found to be operable in a wide range of operating temperatures.

This target, however, is not entirely free of "sticking" effects at relatively low temperatures. In addition, it shows at elevated temperatures a small temperature dependence of limiting resolution.

The plug target was found capable of storing patterns with several hundred lines of resolution for many seconds. This target structure may therefore be of interest as a possible memory plate. The very high degree of anisotropy in the conduction properties of plug targets may also make them useful for many other applications. For instance, if a somewhat thicker (and stronger) film than described in this paper is made the faceplate of a tube, it might be used for transferring a charge image deposited on the vacuum side of the film onto an insulating sheet held against its outside face.

A composite mesh-target structure was formed by depositing a conducting mesh on the insulating areas on one side of a plug target. Such a combination is free of microphonics and can, if desired, be designed to have a relatively high mesh-to-target capacitance.

## ACKNOWLEDGMENTS

The writer gratefully acknowledges helpful discussions with Dr. P. K. Weimer during this work. He also is indebted to several other members of RCA Laboratories: to Dr. H. B. Law for his contribution to the basic technique, to C. H. Morris for his originality and experience in electrochemical methods, and to E. A. James for his assistance in solving target-mounting problems. Acknowledgment also is due to R. L. Van Asselt for many valuable discussions and for permission to present results obtained from plug targets made by him.

# TIME-AVERAGED EFFECTS ON CHARGED PARTICLES IN A-C FIELDS\*

BY

T. W. JOHNSTON

RCA Victor Company, Ltd.,  
Montreal, Canada

*Summary*—When a nonuniform a-c field is applied to a charged particle it experiences a time-averaged acceleration in addition to the a-c acceleration. The development and application of the basic theory to plasmas is outlined, including some cases with a d-c magnetic field. A fairly complete bibliography, and a critique of theory and experiments are also given.

## INTRODUCTION

IN RECENT YEARS considerable attention has been given to time-averaged forces exerted on charged particles by nonuniform a-c fields.<sup>1-28</sup> These particles range from small metal dust particles<sup>21</sup> down to the ions and electrons in plasmas. Most emphasis has been on confinement of hot plasmas, but with some consideration given to possible application to thrust engines with high specific impulse.

As is usual in the early stages of analysis, there is a certain amount of confusion and, indeed, actual error in some of the physical concepts used to explain the results. Gradient field, radiation pressure, plasma dielectric effect are some of the terms involved. The following exposition is intended to clarify the basic ideas and to give a coherent picture of the particle motions so that the phenomena can be readily understood.

It will be shown that "gradient field" is a convenient concept when the particle currents do not seriously alter the impressed fields, and that radiation pressure is the useful idea when the particle currents are so large that very high field and particle density gradients are produced. Essentially, the two concepts are useful for a low-density plasma and a high-density plasma, respectively. Dielectric effect is not a useful idea since incautious application of it leads to erroneous results. When the particle density is so low that the particle currents do not seriously alter the applied fields, the analysis is relatively simple. When the particle density is not low, the trajectory equations must be combined with Maxwell's equations, including particle currents

---

\* Manuscript received 15 October 1960.

and charge effects, and also with an equation of state or stochastic particle interaction equations. A strong magnetic field will seriously inhibit and alter the gradient field action in four out of the five cases considered—the fifth is not likely to be of practical interest.

#### TRAJECTORY EQUATIONS WITH KNOWN FIELDS

The simplest way to approach the single-particle motion is Boot's<sup>1</sup> method which involves the field variation "felt" by the particle as a result of its finite amplitude of motion, and neglects any radiation effects. A simple equation for a particle in an a-c field only with a viscous damping term ( $\nu$ ), (assumed to act only on the first-order motion) is

$$\ddot{\mathbf{r}} = \frac{q}{m} (\mathbf{E} + \dot{\mathbf{r}} \times \mathbf{B}) e^{j\omega t} - \nu \dot{\mathbf{r}}, \quad (1)$$

where  $q$  and  $m$  are the particle charge and mass and  $\mathbf{E}$  and  $\mathbf{B}$  (generally complex numbers) denote the fields at angular frequency  $\omega$ , and the real part of the result is kept. This point must be clearly held in mind since here the second-order effects are of interest, involving products of a-c quantities. A more general case is to include fields of different frequencies. This adds nothing to the understanding and so only  $\omega$ -periodic fields are considered.

For nonrelativistic velocities and  $\mathbf{B}$  derived from  $\nabla \times \mathbf{E}$ , the  $\dot{\mathbf{r}} \times \mathbf{B}$  term is of second order compared to the first so, for a first-order equation, take

$$\ddot{\mathbf{r}}_1 = \frac{q}{m} \mathbf{E} e^{j\omega t} - \nu \dot{\mathbf{r}}_1, \quad (2)$$

with  $\mathbf{E}$  sufficiently small and uniform that the first-order motion is given by the uniform electric field equation. The first-order amplitude ( $\delta r_1$ ) and velocity ( $\dot{\mathbf{r}}_1$ ) are

$$\delta r_1 = -\frac{q}{m} \frac{\mathbf{E}}{\omega^2} \frac{1 + j\nu/\omega}{1 + \nu^2/\omega^2} e^{j\omega t}, \quad (3)$$

$$\dot{\mathbf{r}}_1 = \frac{q}{m} \frac{\mathbf{E}}{j\omega} \frac{1 + j\nu/\omega}{1 + \nu^2/\omega^2} e^{j\omega t}. \quad (4)$$

For the correction to the first-order equation, substitute equations (3) and (4) into (2) to give

$$\begin{aligned} \ddot{\mathbf{r}} \approx \ddot{\mathbf{r}}_1 + \ddot{\mathbf{r}}_2 = & \frac{q}{m} (\mathbf{E} + (\delta r_1 \cdot \nabla)) \mathbf{E} e^{j\omega t} \\ & + \frac{q}{m} \dot{\mathbf{r}}_1 \times (\mathbf{B} + (\delta r_1 \cdot \nabla) \mathbf{B}) e^{j\omega t} - v \dot{\mathbf{r}}, \end{aligned} \quad (5)$$

where, in the Cartesian notation,<sup>32</sup> we take for any two vector functions  $\mathbf{a}$ ,  $\mathbf{b}$  of coordinates  $x_m$ ,  $x_n$ ,

$$\nabla \mathbf{b} = \frac{\partial b_m}{\partial x_n} \mathbf{i}_m \mathbf{i}_n = \mathbf{b} \nabla, \quad (6)$$

and

$$(\mathbf{a} \cdot \nabla) \mathbf{b} = \nabla \mathbf{b} \cdot \mathbf{a} = a_n \frac{\partial b_m}{\partial x_n} \mathbf{i}_m, \quad (6a)$$

as distinct from

$$\mathbf{a} \cdot (\nabla \mathbf{b}) = a_m \frac{\partial b_m}{\partial x_n} \mathbf{i}_n, \quad (6b)$$

with  $\mathbf{i}_m$  a unit vector in the  $x_m$  direction. The motion then is

$$\begin{aligned} \ddot{\mathbf{r}} = & \frac{q}{m} \mathbf{E} e^{j\omega t} - \frac{q}{m} \frac{v}{j\omega} \frac{1 + jv/\omega}{1 + (v/\omega)^2} \mathbf{E} e^{j\omega t} \\ & - \left( \frac{q}{m} \right)^2 \frac{1}{\omega^2} \left[ \left( \frac{1 + jv/\omega}{1 + (v/\omega)^2} \mathbf{E} e^{j\omega t} \right) \cdot \nabla \right] \mathbf{E} e^{j\omega t} \\ & \quad + \left( \frac{q}{m} \right)^2 \left( \frac{1}{j\omega} \frac{1 + jv/\omega}{1 + (v/\omega)^2} \mathbf{E} e^{j\omega t} \right) \times \mathbf{B} e^{j\omega t} \\ & - \left( \frac{q}{m} \right)^3 \left( \frac{1}{j\omega} \frac{1 + jv/\omega}{1 + (v/\omega)^2} \mathbf{E} e^{j\omega t} \right) \\ & \quad \times \left( \frac{1}{\omega^2} \frac{1 + jv/\omega}{1 + (v/\omega)^2} \mathbf{E} e^{j\omega t} \cdot \nabla \right) \mathbf{B} e^{j\omega t}. \end{aligned} \quad (7)$$

If we average over one  $\omega$  period, all the odd harmonics average to zero, leaving

$$\langle \ddot{\mathbf{r}} \rangle = - \left( \frac{q}{m} \right)^2 \frac{1}{\omega^2} \left\langle \left\{ \left( \frac{1 + jv/\omega}{1 + v^2/\omega^2} \mathbf{E} e^{j\omega t} \cdot \nabla \right) \mathbf{E} e^{j\omega t} + j\omega \frac{1 + jv/\omega}{1 + (v/\omega)^2} \mathbf{E} e^{j\omega t} \times \mathbf{B} e^{j\omega t} \right\} \right\rangle \quad (8)$$

where  $\langle \rangle$  denotes the time average. This time average is more artistically written as

$$\begin{aligned} \langle \ddot{\mathbf{r}} \rangle = & - \left( \frac{q}{m} \right)^2 \frac{1}{\omega^2} \frac{1}{2} \operatorname{Re} \frac{(\mathbf{E} \cdot \nabla) \mathbf{E}^*}{1 + (v/\omega)^2} \\ & + \left( \frac{q}{m} \right)^2 \frac{1}{\omega^2} \frac{v/\omega}{1 + (v/\omega)^2} \frac{1}{2} \operatorname{Im} (\mathbf{E} \cdot \nabla) \mathbf{E}^* \\ & + \left( \frac{q}{m} \right)^2 \frac{1}{\omega} \frac{1}{2} \operatorname{Im} \frac{(\mathbf{E} \times \mathbf{B}^*)}{1 + (v/\omega)^2} \\ & + \left( \frac{q}{m} \right)^2 \frac{1}{\omega} \frac{v/\omega}{1 + (v/\omega)^2} \frac{1}{2} \operatorname{Re} (\mathbf{E} \times \mathbf{B}^*) \quad (9) \end{aligned}$$

Now from Maxwell's relation,

$$\begin{aligned} \nabla \times \mathbf{E} e^{j\omega t} &= -j\omega \mathbf{B} e^{j\omega t} \\ \nabla \times \mathbf{E} &= -j\omega \mathbf{B} \\ \nabla \times \mathbf{E}^* &= j\omega \mathbf{B}^* \end{aligned} \quad (10)$$

[since  $(xy)^* = x^*y^*$ ]. Hence

$$\begin{aligned} \langle \ddot{\mathbf{r}} \rangle = & - \left( \frac{q}{m} \right)^2 \frac{1}{\omega^2} \frac{1}{1 + (v/\omega)^2} \frac{1}{2} [\operatorname{Re} (\mathbf{E} \cdot \nabla) \mathbf{E}^* + \operatorname{Re} (\mathbf{E} \times \nabla \times \mathbf{E}^*)] \\ & + \left( \frac{q}{m} \right)^2 \frac{1}{\omega^2} \frac{v/\omega}{1 + (v/\omega)^2} \frac{1}{2} [\operatorname{Im} (\mathbf{E} \cdot \nabla) \mathbf{E}^* + \operatorname{Im} (\mathbf{E} \times \nabla \times \mathbf{E}^*)]. \end{aligned} \quad (11)$$

Now, using the notation for Cartesian tensors,<sup>32</sup> we have

$$(\mathbf{E} \cdot \nabla) \mathbf{E}^* \equiv (\nabla \mathbf{E}^*) \cdot \mathbf{E} \text{ and } \mathbf{E} \times (\nabla \times \mathbf{E}^*) = \mathbf{E} \cdot (\nabla \mathbf{E}^*) - (\nabla \mathbf{E}^*) \cdot \mathbf{E} \quad (12)$$

so that

$$(\mathbf{E} \cdot \nabla) \mathbf{E}^* + \mathbf{E} \times (\nabla \times \mathbf{E}^*) = \mathbf{E} \cdot (\nabla \mathbf{E}^*) = E_m \frac{\partial E_m^*}{\partial x_n} \mathbf{i}_n \quad (13)$$

with the usual summation over repeated indices and with  $\mathbf{i}_n$  as the unit vector associated with  $x_n$ , as before. Now,

$$\begin{aligned} \operatorname{Re} \mathbf{E} \cdot (\nabla \mathbf{E}^*) &= \operatorname{Re} \left[ (E_{mr} + jE_{mi}) \frac{\partial (E_{mr} - jE_{mi})}{\partial x_n} \right] \mathbf{i}_n \\ &= \left[ E_{mr} \frac{\partial E_{mr}}{\partial x_n} + E_{mi} \frac{\partial E_{mi}}{\partial x_n} \right] \mathbf{i}_n = \frac{1}{2} \left[ \frac{\partial E_{mr}^2}{\partial x_n} + \frac{\partial E_{mi}^2}{\partial x_n} \right] \mathbf{i}_n = \frac{1}{2} \nabla (\mathbf{E} \cdot \mathbf{E}^*) \end{aligned} \quad (14)$$

If we put  $\mathbf{E} = (E_{mr} + jE_{mi}) \mathbf{i}_m = |E_m| e^{j\theta} \mathbf{i}_m$

$$\operatorname{Im} (\mathbf{E} \cdot \nabla \mathbf{E}^*) = \left[ E_{mi} \frac{\partial E_{mr}}{\partial x_n} - E_{mr} \frac{\partial E_{mi}}{\partial x_n} \right] \mathbf{i}_n = -E_m^2 \frac{\partial \theta_m}{\partial x_n} \mathbf{i}_n \quad (15)$$

$$= -E_m E_m^* \frac{\partial \theta_m}{\partial x_n} \mathbf{i}_n$$

Hence

$$\langle \dot{\mathbf{r}} \rangle = -\frac{1}{2} \left( \frac{q}{m} \right)^2 \frac{1}{\omega^2} \frac{1}{1 + (v/\omega)^2} \left[ \frac{1}{2} \nabla (\mathbf{E} \cdot \mathbf{E}^*) + \frac{v}{\omega} E_m E_m^* \frac{\partial \theta_m}{\partial x_n} \mathbf{i}_n \right] \quad (16)$$

The first of these terms is what is known as the gradient field term, and shows that there is a time-averaged acceleration of particles to electric field strength minima, regardless of charge sign.

The second term is somewhat different. It only exists for a propagating wave since  $\partial \theta_m / \partial x_n = 0$  for a standing wave (except at nodes when  $E_m = 0$ ). In a sense it can be regarded as a viscous drag on the momentum of the electromagnetic field, so that the propagating wave will drag the particle with it along the Poynting vector, but only by the viscous or in-phase component of the current. The phenomenon is essentially that of radiation pressure on an absorber.

The trajectory approach will give more physical insight if we consider a few special cases.

STANDING WAVE

In a pure standing-wave system,

$$E_m E_m^* \frac{\partial \theta_m}{\partial x_n} \mathbf{i}_n$$

is zero (since the phase changes only at field zeros) and here we can take  $E$  to be real everywhere. The two cases are (writing  $\mathbf{E} \cdot \mathbf{E}^* = E^2$  for brevity)

$$\mathbf{E} \perp \nabla E^2 \quad \text{and} \quad \mathbf{E} \parallel \nabla E^2.$$

Without following the analyses in detail a few points will be indicated.

$\mathbf{E} \parallel \nabla E^2$

Here the  $(\mathbf{E} \cdot \nabla) \mathbf{E}$  term is the operative one since we take  $\nabla \times \mathbf{E} = 0$ . The simplest case to take is  $\partial E / \partial z = \text{constant} = E_0 / z_0$  and gives

$$\ddot{z} = \frac{q}{m} \frac{E_0}{z_0} z \cos \omega t, \tag{17}$$

with  $z = 0$  at  $E = 0$ . This is a Mathieu equation with the nonperiodic term equal to zero as is seen by putting  $2u = \omega t$  and obtaining

$$\frac{d^2 z}{du^2} - \frac{4}{\omega^2} \frac{q}{m} \frac{E_0}{z_0} z \cos 2u = 0, \tag{18}$$

which is equivalent to

$$\frac{d^2 z}{du^2} + (\theta_0 + 2\theta_1 \cos 2u) z = 0, \tag{19}$$

$$\theta_0 = 0, \quad \theta_1 = -\frac{2}{\omega^2} \frac{q}{m} \frac{E_0}{z_0} = -\frac{2}{\omega^2} \frac{q}{m} \frac{\partial E}{\partial z}. \tag{19a}$$

For  $\theta_1 \ll 1$  the solution is nearly

$$z \approx z_0 \cos \left( \theta_1 \frac{u}{\sqrt{2}} \right) \text{ and } \ddot{z} \approx -\frac{1}{2} \frac{1}{\omega^2} \left( \frac{q}{m} \right)^2 \frac{E_0^2}{z_0^2} z, \quad (20)$$

for  $z = z_0$  (and  $E = E_0$ ) at  $t = 0$ .

If we had begun with the gradient-field formula,

$$\begin{aligned} \langle \ddot{z} \rangle &= -\frac{1}{4} \left( \frac{q}{m} \right)^2 \frac{1}{\omega^2} \nabla E^2 = -\frac{1}{4} \left( \frac{q}{m} \right)^2 \frac{1}{\omega^2} \nabla \left( \frac{E_0}{z_0} z \right)^2 \\ &= -\frac{1}{2} \left( \frac{q}{m} \right)^2 \frac{1}{\omega^2} \frac{E_0^2}{z_0^2} z, \end{aligned} \quad (21)$$

which will give the same results as the Mathieu equation, provided  $\theta_1$

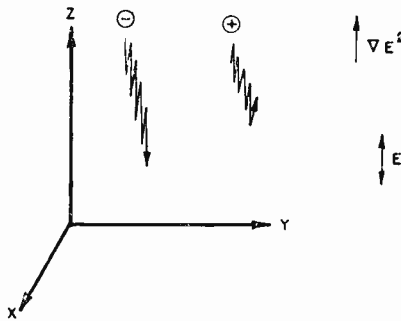


Fig. 1—Single-particle motions for  $\nabla E^2 \parallel \mathbf{E}$ , sketched for a negative  $\ominus$  and heavier positive  $\oplus$  particle.

is small. If we included the second-order terms to give the “ripples” on the main term, the result would be similar to Figure 1. The particle moves out of phase with the field and so sees an opposing force wherever it is. The opposing force is stronger in the high field region and the particle is driven towards the field minimum. The action is that of strong focusing. This action is the dominant one in low-frequency systems ( $\lambda \gg$  apparatus dimensions) since, at low frequencies  $\nabla \times \mathbf{E} = 0$  systems are nearly obtained, i.e., the r-f magnetic field is small.

$\mathbf{E} \perp \nabla E^2$

The next simple gradient field case is with  $\nabla E^2$  perpendicular to

**E.** Then, instead of the  $(\mathbf{E} \cdot \nabla)\mathbf{E}$  term the  $\mathbf{E} \times (\nabla \times \mathbf{E})$  term (the Lorentz force) dominates in Equation (11).

The simple trajectory equations are, in the Cartesian system of Figure 2,

$$\ddot{x} = -\frac{q}{m} E_x \cos \omega t \qquad \ddot{z} = -\frac{q}{m} \dot{x} B_y, \tag{22}$$

and

$$B_y = -\frac{1}{\omega} \frac{\partial E_x}{\partial z} \sin \omega t. \tag{23}$$

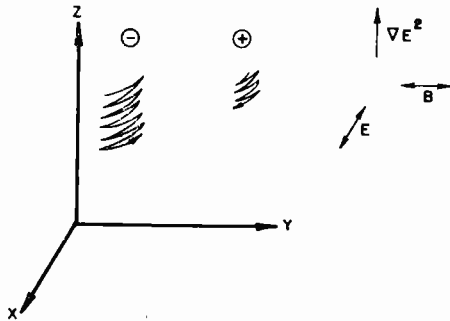


Fig. 2—Single particle motions for  $\mathbf{E} \perp \nabla E^2$ .

This gives

$$\begin{aligned} \dot{x} &= \frac{q}{m} \frac{E_x}{\omega} \sin \omega t, \\ \ddot{z} &= -\left(\frac{q}{m}\right)^2 \frac{1}{\omega^2} E_x \frac{\partial E_x}{\partial z} \sin^2 \omega t \\ &= -\frac{1}{4} \left(\frac{q}{m}\right)^2 \frac{1}{\omega^2} \frac{\partial E_x^2}{\partial z} (1 - \cos 2\omega t) \\ \langle \ddot{z} \rangle &= -\frac{1}{4} \left(\frac{q}{m}\right)^2 \frac{1}{\omega^2} \frac{\partial E_x^2}{\partial z}, \end{aligned} \tag{24}$$

and if  $z$  and  $x$  are plotted, the trajectory is that shown in Figure 2.

## PROPAGATING WAVE

In a plane wave propagating without attenuation,  $\mathbf{E} \cdot \mathbf{E}^*$  is uniform and the  $\nabla(\mathbf{E} \cdot \mathbf{E}^*)$  term is zero. If there is attenuation, as well as a  $\nabla E^2$  term due the loss, there appears to be an in-phase current resulting from  $\nu$ , the damping term. If the plane wave propagating in the  $z$ -direction is given by  $E_0 \exp(-j\beta z) \exp(j\omega t)$  where  $E_0$  and  $\beta$  are uniform and constant (i.e., we assume so few particles that their effect on the wave is negligible), then

$$E_m E_m^* \frac{\partial \theta_m}{\partial x_n} \mathbf{i}_n = -\beta E_0^2 \mathbf{i}_z, \quad (25)$$

and the result should be

$$\langle \ddot{\mathbf{r}} \rangle = \langle \ddot{z} \rangle \mathbf{i}_z = \frac{1}{2} \left( \frac{q}{m} \right)^2 \frac{1}{\omega^2} \frac{\nu/\omega}{1 + (\nu/\omega)^2} \beta E_0^2 \mathbf{i}_z. \quad (26)$$

If we include the effect of  $\nu$  only on the motion due to  $\mathbf{E}$  (to be consistent with the previous analysis), and take  $\mathbf{E}$  to be along the  $x$  axis, we have

$$\mathbf{E} e^{j\omega t} = E_0 \cos(\omega t - \beta z) \mathbf{i}_x, \quad (27)$$

$$\mathbf{B} e^{j\omega t} = \frac{\beta}{\omega} E_0 \cos(\omega t - \beta z) \mathbf{i}_y, \quad (28)$$

$$\ddot{x} = \frac{q}{m} E_0 \cos(\omega t - \beta z) - \nu \dot{x} \quad \text{or}$$

$$\dot{x} = \frac{q}{m} \frac{E e^{j\omega t}}{\nu + j\omega} = \frac{E_0}{\nu^2 + \omega^2} [\nu \cos(\omega t - \beta z) + \omega \sin(\omega t - \beta z)],$$

$$\ddot{z} = \frac{q}{m} \dot{x} \beta e^{j\omega t}$$

$$= \left( \frac{q}{m} \right)^2 \frac{\beta}{\omega} E_0^2 \left( \frac{\nu \cos^2(\omega t - \beta z) + \omega \sin(\omega t - \beta z) \cos(\omega t - \beta z)}{\nu^2 + \omega^2} \right), \quad (29)$$

so that

$$\langle \dot{z} \rangle = \left( \frac{q}{m} \right)^2 \frac{\beta}{\omega} E_0^2 \frac{v/2}{v^2 + \omega^2} = \frac{1}{2} \left( \frac{q}{m} \right)^2 \frac{1}{\omega^2} \frac{v/\omega}{1 + (v/\omega^2)} \beta E_0^2 \quad (30)$$

as predicted from the general Equations (16) and (26).

Essentially, in addition to absorbing power from the a-c field, the in-phase or resistive current flow also can be said to induce momentum "absorption," and so the particle drifts or, more descriptively, is dragged, in the direction of propagation — exactly the mechanism of radiation pressure on an absorber.

At this point a word of caution is in order. This use of a viscous term in the equation is very useful in certain cases, and certainly applies well to metallic particles in a gas,<sup>21</sup> where the charged particle sustains many small impacts per cycle. In a low-loss plasma, when we consider electrons, the effect of near collisions is to deflect the electron in an unpredictable way very suddenly once in many cycles. Long-range coulomb forces are still more difficult to treat satisfactorily, involving something like simultaneous small deflections. Only a much more sophisticated analysis than any given here would really justify this crude use of the viscous collision term. Intuitively, the author believes that the effect would become manifest if the system were sufficiently stable to allow each particle many collisions without appreciable outside changes, i.e., for times much larger than  $1/v$ . For very early times (much less than  $1/v$ ) the effect (if any) would probably be negligible.

Note that this difficulty does not upset normal plasma theory, since sufficiently large volumes of plasma can be considered for sufficiently long times to obtain enough collisions in the time interval to use statistical theory, and the total effect of electron flow is of interest. In this formulation, up to this point, only a single particle has been considered.

There is no reason why the formulation cannot be extended to blobs of charge rather than single particles, providing it is understood that any application of the absorption or propagation drag term be treated somewhat cautiously.

#### TWO-BLOB MODEL

Systems of interest usually have used resonant or standing wave arrangements. Because of this and because of the reservations concerning the drag term, we will here only consider the  $\nabla(\mathbf{E} \cdot \mathbf{E}^*)$  term

applied to a two-blob model, called the elastic-band, ping-pong, and soccer ball model.\* Since we consider the positive (ion) blob to be much heavier than the negative electron blob, let us repeat the simple trajectory picture for each case.

$E \parallel \nabla E^2$

In just the same way as for the single-particle model we set up two equations, one for each blob;

$$\begin{aligned} \ddot{z}_e + \frac{e}{m} \frac{dE}{dz} z_e \cos \omega t + \frac{M}{m+M} f(z_e - z_i) &= 0, \\ \ddot{z}_i - \frac{e}{m} \frac{dE}{dz} z_i \cos \omega t - \frac{m}{m+M} f(z_e - z_i) &= 0. \end{aligned} \quad (31)$$

If we consider the two blobs to separate only by a small amount  $|z_e - z_i| \ll z_e, z_i$ , then the natural choice for  $f(z_e - z_i)$ , the coulomb force between them, is proportional to  $(z_e - z_i)$ . Furthermore for two infinite slabs the constant is

$$\omega_p^2 = \frac{Ne^2}{mM} \approx \frac{Ne^2}{m\epsilon_0} \frac{\epsilon_0}{m+M}$$

the natural restoring force oscillation frequency. For cylinders or spheres the constant would be  $\omega_p^2/2$  and  $\omega_p^2/3$ , respectively. Using  $f(z_e - z_i) = \omega_p^2(z_e - z_i)$  we have, on elimination of  $\omega_p^2$ ,

$$\frac{m}{m+M} \ddot{z}_e + \frac{M}{m+M} \ddot{z}_i + \frac{e}{m+M} \left( \frac{dE}{dz} \right) (z_e - z_i) \cos \omega t = 0. \quad (32)$$

The location of the centre of mass of the system is given by

$$z_m = z_e \frac{m}{m+M} + z_i \frac{M}{m+M}, \quad (33)$$

---

\* This model is easy to justify for blobs much smaller than  $C/\omega_p$  (so the field can penetrate) and for separations ( $\sim eE/m\omega_p^2$ ) much smaller than the blob dimensions. Larger blobs must include the effect of propagating the field around the blob.

so the equation is simply

$$\ddot{z}_m + \frac{e}{m+M} \left( \frac{dE}{dz} \right) \delta \cos \omega t = 0, \tag{34}$$

where

$$\delta = z_e - z_i.$$

If we write  $\ddot{z}_e = \ddot{z}_i + \ddot{\delta}$  and eliminate  $\ddot{z}_i$ , we have

$$\ddot{\delta} + e \left( \frac{dE}{dz} \right) \left( \frac{z_e}{m} + \frac{z_i}{M} \right) \cos \omega t + \frac{M+m}{M+m} \omega_p^2 \delta = 0,$$

or

$$\ddot{\delta} + \omega_p^2 \left[ 1 + \frac{1}{\omega_p^2} \frac{M-m}{Mm} e \frac{dE}{dz} \cos \omega t \right] \delta = -e \frac{dE}{dz} z_m \frac{M+m}{Mm} \cos \omega t. \tag{35}$$

Remembering that  $\delta$  is small and assuming that  $z_m$  changes very little in many  $\omega$ -cycles and avoiding resonance ( $\omega = \omega_p$ ) (or invoking a viscous term),

$$\delta \approx e \frac{M+m}{Mm} \frac{dE}{dz} z_m \frac{\cos \omega t}{\omega^2 - \omega_p^2} \tag{36}$$

the usual equation for a driven system with a resonant frequency  $\omega_p$ . Note also that  $\delta$  changes phase above and below resonance. Now we have

$$\ddot{z}_m + \frac{e^2}{mM} \left( \frac{dE}{dz} \right)^2 \frac{z_m \cos^2 \omega t}{\omega^2 - \omega_p^2} = 0. \tag{37}$$

This is another Mathieu equation;

$$\frac{dz_m}{d(\omega t)^2} + \frac{1}{2} \frac{e^2}{mM} \left( \frac{dE}{dz} \right)^2 \frac{1}{\omega^2 (\omega^2 - \omega_p^2)} (1 + \cos 2(\omega t)) z_m = 0, \tag{38}$$

with

$$\theta_0 = \frac{1}{2} \left[ \frac{e}{(mM)} \frac{1}{2} \frac{dE}{dz} \frac{1}{\omega^2} \right]^2 \frac{1}{1 - \omega_p^2/\omega^2} \quad \text{and} \quad \theta_1 = \theta_0/2.$$

At this point it is useful to examine the nature of the solutions of the Mathieu equation close to the origin ( $\theta_0 = \theta_1 = 0$ ) of the so-called Mathieu stability diagram.<sup>30</sup> Essentially, the situation is as shown in Figure 3. The dividing line between the stable and unstable

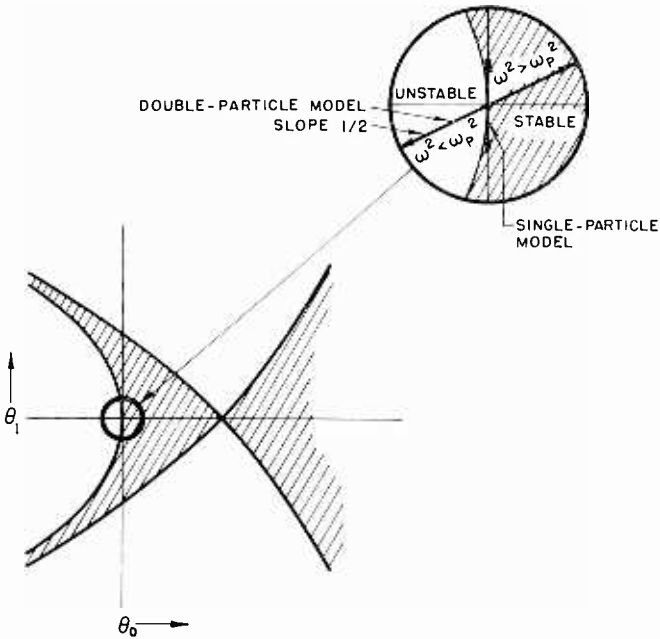


Fig. 3—Mathieu stability chart, showing region near the origin. Stable region (bounded solution) shaded.

regions is shown as is the characteristic of the solution to the single blob made with  $\theta_0 = 0$  which is always stable (i.e., bounded) for small  $\theta_1$ . This two-blob case corresponds to the line  $\theta_1 = \theta_0/2$  and is stable for  $\theta_0 > 0$  and unstable for  $\theta_0 < 0$ . Since all the other terms in  $\theta_0$  are positive, this means that the solution is stable for  $\omega > \omega_p$  and unstable for  $\omega < \omega_p$ .

For  $1 \gg \theta_0 > 0$  ( $\omega > \omega_p$ )

$$z_m = z_0 \cos(\theta_0^{1/2} \omega t) \left[ 1 + \frac{\theta_0}{4} \cos 2\omega t + \frac{\theta_0^2}{128} \cos 4\omega t + \dots \right] \quad (39a)$$

For  $|\theta_0| \ll 1$ ,  $\theta_0 < 0$  ( $\omega < \omega_p$ )

$$z_m = z_0 \cosh (\theta_0 \frac{1}{2} \omega t) \left[ 1 + \frac{\theta_0}{4} \cos 2\omega t + \frac{\theta_0^2}{128} \cos 4\omega t + \dots \right] \quad (39b)$$

where  $z = 0$  at  $t = 0$ . In this model  $E$  is proportional to  $z_m$ , so that for  $\omega^2 \gg \omega_p^2$  the gradient field approach applies with

$$\langle \ddot{z} \rangle = - \frac{q^2}{mM} \frac{1}{\omega^2} \frac{1}{4} \nabla E^2,$$

i.e., as if to a fictitious particle of mass equal to the geometric mean of the masses.

Note that this combined acceleration is more effective (by the ratio  $M/m$ ) than the effect on the heavy particles alone. The large excursion amplitude of the electrons means that they “see” a greater field difference and so they drag the ions along with them much faster than the ions would go if left to their own devices. When  $\omega_p > \omega$  the acceleration is reversed in sign and for  $\omega^2 \ll \omega_p^2$  the magnitude depends mainly on  $\omega_p^2$ . The more general formula for  $\mathbf{E} \parallel \nabla E^2$  becomes

$$\langle \ddot{z} \rangle = - \frac{q^2}{4mM} \frac{1}{\omega^2 - \omega_p^2} \nabla E^2 \quad (40)$$

except at resonance, when damping processes must be considered.

The idea that for  $\mathbf{E} \parallel \nabla E^2$  the plasma will move towards strong fields at low frequencies is not really strange, since it is the familiar phenomena of dielectrophoresis.<sup>29</sup> At the limit of d-c for example, the gradient in the field means that part of the blob is in a stronger field than the other and so pulls harder and the blob travels towards the strong field region.

At frequencies above resonance, the phase of the separation motion is reversed, inertial rather than separation energy is dominant, and the plasma, like a pendulum, finds its motion in anti-phase with the driving field, so the strong field region ejects the plasma more vigorously than the weak field. The single-blob case corresponds to  $\omega_p \rightarrow 0$ , so that all frequencies are above the plasma frequencies and motion is towards the field minima.

### $\mathbf{E} \perp \nabla E^2$

Does this resonance affect the  $\mathbf{E} \perp \nabla E^2$  arrangement? There is an effect, but it is minor. We have

$$\ddot{x}_e = -\frac{e}{m} E_x \cos \omega t, \quad \ddot{x}_i = +\frac{e}{M} E_x \cos \omega t, \quad (41)$$

so

$$\dot{x}_e = -\frac{e}{m} \frac{E_x}{\omega} \sin \omega t, \quad \dot{x}_i = +\frac{e}{M} \frac{E_x}{\omega} \sin \omega t. \quad (42)$$

We assume no charge separation effects in the  $x$  direction because we apply this analysis to cases where  $E_x \perp \nabla n$ , since in high-density cases  $\nabla E^2$  will be mostly the result of  $\nabla n$  and hence parallel to it.

$$\begin{aligned} \ddot{z}_e &= -\frac{e}{m} \dot{x}_e B_y - \frac{M}{m+M} \omega_p^2 (z_e - z_i); \\ \ddot{z}_i &= \frac{e}{M} \dot{x}_i B_y + \frac{m}{m+M} \omega_p^2 (z_e - z_i), \end{aligned} \quad (43)$$

and, as before,

$$B_y = -\frac{1}{\omega} \frac{\partial E_x}{\partial z} \sin \omega t.$$

If we eliminate  $\omega_p^2$  as before and write  $z_m$  and  $\delta$  as before, then

$$z_m = -\frac{1}{4} \frac{e^2}{mM} \frac{1}{\omega^2} \frac{\partial E_x^2}{\partial z} (1 - \cos 2\omega t) \quad (44)$$

$$\langle \ddot{z}_m \rangle = -\frac{1}{4} \frac{e^2}{mM} \frac{1}{\omega^2} \frac{\partial E_x^2}{\partial z} \quad (45)$$

and the  $z_m$  motion is just that of a composite particle of mass  $(mM)^{1/2}$ . For  $\delta$  we have

$$\ddot{\delta} + \frac{1}{4} e^2 \left( \frac{1}{m^2} - \frac{1}{M^2} \right) \frac{1}{\omega^2} \frac{\partial E_x^2}{\partial z} (1 - \cos 2\omega t) + \omega_p^2 \delta \left( \frac{m+M}{m+M} \right) = 0, \quad (46)$$

or for  $M \gg m$ ,

$$\ddot{\delta} + \frac{1}{4\omega^2} \left( \frac{e}{m} \right)^2 \frac{\partial E^2}{\partial z} (1 - \cos 2\omega t) + \omega_p^2 \delta = 0, \quad (46a)$$

with the forcing solution

$$\delta = -\frac{1}{4\omega^2} \left( \frac{e}{m} \right)^2 \frac{\partial E^2}{\partial z} \left( \frac{1}{\omega_p^2} - \frac{1}{\omega_p^2 - 4\omega^2} \cos 2\omega t \right). \quad (47)$$

Thus there is a  $\delta$ -resonant effect at  $\omega = \omega_p/2$ , which is to be expected<sup>4</sup> from the  $2\omega$  variation of  $z$  in the single particle model. At the resonant frequency this resonance might be noticed as some instability or oscillation effect, but its effect on the average gradient field action is negligible.

Hence from the two-blob model it can be said that for a plasma without a d-c magnetic field, the gradient field formula works for  $\mathbf{E}_\perp \nabla E^2$  for all frequencies, but for  $\mathbf{E}_\parallel \nabla E^2$  the convenient formula is that of Equation (40). Essentially, if we divide  $\nabla E^2$  into  $\nabla_\parallel E^2$  and  $\nabla_\perp E^2$ , where  $\parallel$  and  $\perp$  refer to parallel and perpendicular to the electric field, we have for the standing-wave system

$$\langle \dot{\mathbf{r}} \rangle = -\frac{1}{4} \frac{q^2}{mM} \frac{1}{\omega^2} \left( \nabla_\perp E^2 + \frac{\nabla_\parallel E^2}{1 - \omega_p^2/\omega^2} \right). \quad (48)$$

#### COMPLETE ANALYSIS

Fairly complete standing-wave analyses have been made by Weibel<sup>4</sup> and Boot<sup>1</sup> for a particular case—that of a cylindrical plasma in an infinite cylinder with a circular symmetric wave guide mode at cutoff (to ensure no complications due to  $z$  variation) at frequencies far below the plasma frequency at the center. Cushing<sup>19</sup> has also produced a somewhat sketchy analysis for the one-dimensional or slab case, apparently unaware of Self's<sup>28</sup> unpublished work. The approach had been indicated earlier by Weibel.<sup>4</sup> Weibel's analysis is without doubt the most thorough, and the difficulties involved in going from a "blob" model to an actual hot plasma made up of particles which do not stay in any given volume are neatly treated. (Ref. 4, p. 66). In all these analyses the applied field is perpendicular to  $\nabla E^2$  and  $\nabla n$  and so the parallel gradient field difficulties are not encountered.

The extension to include the plasma effect on the field is made as follows. By essentially thermodynamic arguments we know that the equilibrium distribution of a gas of particles which are governed by a Hamiltonian ( $H$ ) with a scalar pressure (justified by the low magnetic field) is given by

$$n = n_0 \exp(-H/kT) = n_0 \exp(-\phi/kT) \exp(-mv^2/2kT). \quad (49)$$

From the two-blob model, buttressed by Weibel's arguments, we can write, for the time-averaged potential for ions and electrons,

$$\begin{aligned}\phi_i &= \left( eV_s + \frac{e^2}{4M} \frac{(E^2 - E_M^2)}{\omega^2} \right), \\ \phi_e &= \left( -eV_s + \frac{1}{4} \frac{e^2}{m} \frac{(E^2 - E_M^2)}{\omega^2} \right),\end{aligned}\quad (50)$$

where  $V_s$  is the separation potential due to the space charge; we write

$$\frac{1}{4} \frac{e^2}{m} \frac{(E^2 - E_M^2)}{\omega^2}$$

as potential since, due to  $\nabla E^2$  alone,

$$m \langle \ddot{\mathbf{r}} \rangle = -\frac{m}{4} \omega^2 \left( \frac{e}{m} \right)^2 \nabla E^2,$$

and  $E_M^2$  is an arbitrary constant.

If one neglects charge separation, then  $n_e \approx n_i$ , and

$$\begin{aligned}n_r \approx n_i \approx (n_e n_i)^{\frac{1}{2}} &\approx n_0 \exp \left[ -\frac{e^2 (E^2 - E_M^2)}{8\omega^2 kT} \left( \frac{1}{m} + \frac{1}{M} \right) \right] \\ &\approx n_0 \exp \left[ -\frac{1}{2} \frac{e^2 (E^2 - E_M^2)}{m kT} \frac{1}{4\omega^2} \right].\end{aligned}\quad (51)$$

In addition, we have the well-known wave equation for the plasma including the dielectric effect of the plasma, which really means that now we consider the r-f field produced by collective motion of the electrons, neglected in our single particle treatment. This use of the plasma dielectric coefficient is justified since  $E$  is perpendicular to  $\nabla n$ , by symmetry. The equation is

$$(\nabla \cdot \nabla) \mathbf{E} + \frac{\omega^2}{C^2} \left( 1 - \frac{\omega_p^2}{\omega^2} \right) \mathbf{E} = 0, \quad (52)$$

where  $\omega_p^2 = n_e e^2 / \epsilon_0 m$  and  $1 - \omega_p^2 / \omega^2$  is the usual plasma dielectric coefficient. This is

$$(\nabla \cdot \nabla) \mathbf{E} + \frac{\omega^2}{C^2} \left\{ 1 - \frac{\omega_{pM}^2}{\omega^2} \left[ \exp \left( -\frac{1}{8\omega^2} \frac{e^2(E^2 - E_M^2)}{mkT} \right) \right] \right\} \mathbf{E} = 0. \quad (53)$$

Here  $\omega_{pM}^2$  corresponds to the electron density at a point, so that  $E_M^2$  corresponds to a maximum in  $n_e$  where  $E = E_M$ . Usually (but not necessarily<sup>27,28</sup>) the field is zero at the density maxima and so one chooses one of these as a reference point. This can also be written as

$$(\nabla \cdot \nabla) \mathbf{E} + \frac{\omega^2}{C^2} \left\{ 1 - \frac{\omega_{pM}^2}{\omega^2} \left[ \exp \left( -\frac{\omega_{pM}^2}{\omega^2} \frac{\epsilon_0(E^2 - E_M^2)}{8n_0kT} \right) \right] \right\} \mathbf{E} = 0. \quad (53a)$$

This equation is solved numerically for cylindrical, planar or other geometries and  $n$  is then calculated. For the one-dimensional case, at least, it is easily shown that the sum of the electromagnetic and plasma energy densities is constant.

$$\frac{1}{2} \epsilon_0 \mathbf{E} \cdot \mathbf{E}^* + \frac{1}{2} \mu_0 \mathbf{H} \cdot \mathbf{H}^* + (n_e + n_i) kT = \text{constant}.$$

As expected, for  $\omega_p^2 \gg \omega^2$  the result is a fairly sharp plasma boundary and the plasma appears as a high dielectric coefficient substance, so the radiation pressure effect on a (dielectric) reflector is a useful concept to apply. The analysis can also give estimates of leakage rate to a boundary, since the density never quite reaches zero for nonzero values of  $T$  and finite values of the other parameters, and one can simply use the normal diffusion equation with the density value at the  $E = E_{\text{max}}$  positions.<sup>4</sup>

The limits on the analysis are essentially that the amplitude of motion parallel to  $\nabla n$  be not too large compared with the  $\nabla E^2$ , which is essentially the same as saying that  $(\mathbf{E} \cdot \nabla) \mathbf{E}$  or  $(\mathbf{v} \cdot \nabla) \mathbf{v}$  terms are small. For the planar case this implies that

$$\left( \frac{e}{m} \right)^2 \frac{1}{4\omega^2(\omega_p^2 - \omega^2)} \frac{\partial^2 E^2}{\partial x^2} \ll 1.$$

In the cylindrical case the criterion

$$\left(\frac{e}{m}\right)^2 \frac{1}{4\omega^4} \frac{1}{r} \frac{\partial E^2}{\partial r} \ll 1$$

has been shown by Weibel<sup>4</sup> to be the proper limit. For interesting cases, the energy limit of application of the theory is much lower for cylindrical geometry than for the planar case because the radius  $r$  in the cylindrical case is usually very small. Weibel<sup>5</sup> has criticized Boot's<sup>1</sup> practical calculations on this score.

When the analysis is applied to a spherical system,<sup>9,18</sup> different degenerate modes must be superimposed at the same frequency to stop the escape at vector field singularities (in this case zeroes) which exist on simply connected surfaces. This means that symmetry assumptions cannot be made and the calculations are very difficult.

At this point it seems appropriate to tidy up the confusion that surrounds the idea of gradient-field action and the radiation pressure concept. Essentially the terms are the microscopic and macroscopic ways of looking at the same effect. Radiation pressure gives a pressure from macroscopic conservation of momentum. One looks at the field momentum on either side of some region and calculates the pressure required to account for the reflection or absorption of momentum, without calculating how the reflection or absorption occurred. The gradient field approach means the study of the particle motions and their effects to give a complete solution. In fact, the reflection or absorption of field momentum is *always* a gradient field effect, and the effect on the electrons in the reflector or absorber is transmitted to the body by the space-charge separation or dipole forces and the resultant force on positive ions or centers in the body. The concept of radiation pressure is only appropriate to the  $\mathbf{E} \perp \nabla E^2$  case, since a wave propagates (and can exert a pressure) only perpendicular to  $E$ . Radiation pressure is not a useful concept for  $\mathbf{E} \parallel \nabla E^2$  systems since propagation must then be parallel to the surface: one might have to consider a surface wave effect.

Another point of confusion is the fact that the  $\nabla E^2$  effect varies as  $1/\omega^2$  while radiation pressure is independent of frequency. This apparent contradiction is resolved if the frequency behaviour of an  $\mathbf{E} \perp \nabla E^2$  slab system is followed. At high frequencies there is little confinement and little reflection and both vary as  $1/\omega^2$

$$R = \frac{1 - \left(1 - \frac{\omega_p^2}{\omega^2}\right)^{1/2}}{1 + \left(1 - \frac{\omega_p^2}{\omega^2}\right)^{1/2}} \approx \frac{1}{4} \frac{\omega_p^2}{\omega^2} \quad (\text{for } \omega^2 \gg \omega_p^2)$$

where  $R$  is the magnitude of the reflection coefficient for a lossless plasma slab (see Figure 4).

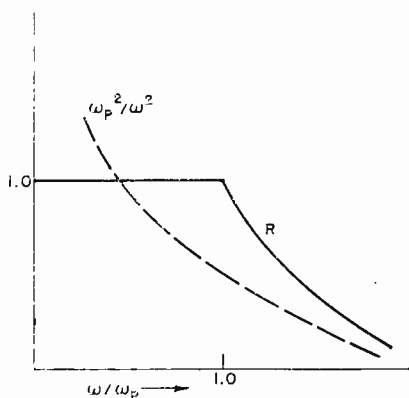


Fig. 4—Variation of reflection coefficient ( $R$ ) and  $\omega_p^2/\omega^2$  with normalized frequency ( $\omega/\omega_p$ ).

As the frequency is lowered  $R$  becomes unity at  $\omega = \omega_p$  and the slab reflects perfectly. From there on the reflection and hence the “radiation pressure” on the slab does not vary with decreasing frequency. On the other hand, the  $\nabla E^2$  effect varies as  $1/\omega^2$ , down until the concept is no longer applicable. The confusion comes from not recognizing the fact that the plasma is not a slab but a fluid. Its boundary is not sharp, but as the frequency is lowered the boundary becomes sharper and  $\nabla E^2$  increases. When the density is greater than that corresponding to  $\omega$  (i.e., the critical density), the lossless plasma with a gradual boundary is a perfect reflector, but is not perfectly confined. The “leak rate” is such that its logarithm varies as  $1/\omega^2$  and this is continually reduced as  $\omega$  is lowered and the gradient steepened. (See Figure 5, illustrating a one-dimensional system.)

The situation is a little like putting a porous stopper in a hole in a water pipe: as soon as the hole is more or less filled the water in the pipe “sees” a reflector; outside the pipe the leak rate is reduced indefinitely by adding more material to the plug.

#### *Effect of a Strong D-C Magnetic Field*

To begin with we will neglect space-charge effects in the analysis and discuss them again at the end of this section. In general, the equations resemble Mathieu equations but are usually worse, and it

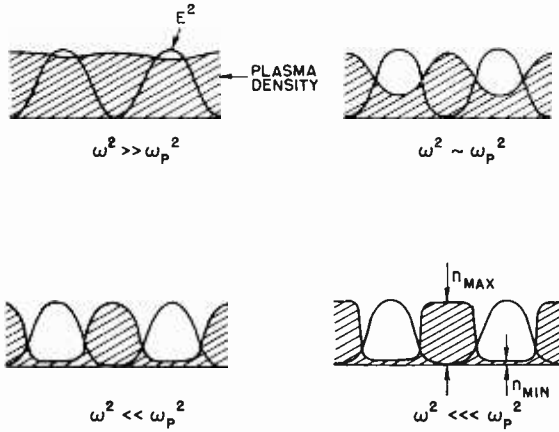


Fig. 5a—Behaviour of one-dimensional standing wave plasma confinement system for constant normalized electric field  $\left(\frac{1}{8} \frac{\epsilon_0 E_{max}^2}{n_{max} kT}\right)^{\frac{1}{2}}$  and varying frequency.

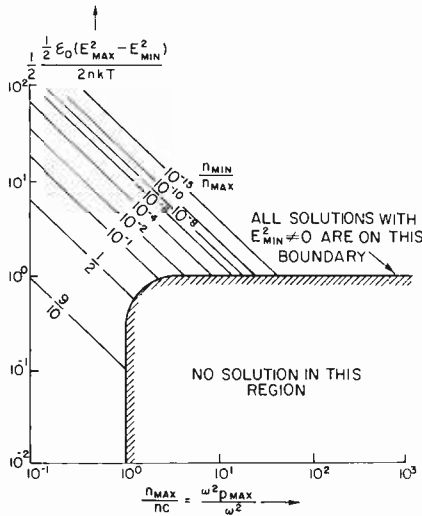


Fig. 5b—Relative minimum density ( $n_{min}/n_{max}$ ) as a function of normalized field and frequency ( $\omega/\omega_{pmax}$ ) or density  $n_{max}/n_c$ .

$$\frac{n_{min}}{n_{max}} = \exp\left(-\frac{n_{max}}{n_c} \frac{\epsilon_0 (E_{max}^2 - E_{min}^2)}{8n_{max} kT}\right)$$

Boundary Equation

$$\frac{n_{max}}{n_c} = -\ln\left(1 - \frac{n_{max}}{n_c} \frac{\epsilon_0 (E_{max}^2 - E_{min}^2)}{8n_{max} kT}\right) \left(\frac{\epsilon_0 (E_{max}^2 - E_{min}^2)}{8n_{max} kT}\right)^{-1}$$

requires ruthless simplification and approximation to obtain any simple results.

We can distinguish two cases for  $\mathbf{E} \parallel \nabla E^2$ ,  $\mathbf{B}$  parallel to  $\mathbf{E}$  and  $\nabla E^2$  (a trivial case since there is no effect) and  $\mathbf{B}$  perpendicular to  $\mathbf{E}$  and  $\nabla E^2$ . For  $\mathbf{E} \perp \nabla E^2$ ,  $\mathbf{B}$  can have three directions, parallel to  $\mathbf{E}$ ,  $\nabla E^2$  and the r-f magnetic field (i.e., perpendicular to both  $\mathbf{E}$  and  $\nabla E^2$ ). The simple linear model will be used again.

### $\mathbf{E} \parallel \nabla E^2$

For  $\mathbf{B} \parallel \mathbf{E}$ ,  $\nabla E^2$ , there is no motion across  $B$ ; therefore it has no effect and the situation is as if there were no magnetic field.

For  $\mathbf{B} \perp \mathbf{E}$ ,  $\nabla E^2$ , taking the magnetic field along the  $x$  axis and  $\mathbf{E}$ ,  $\nabla E^2$  along the  $z$  axis, we have

$$\begin{aligned}\ddot{z} &= \frac{q}{m} \left( E + z \frac{dE}{dz} \right) \cos \omega t - \dot{y} \frac{q}{m} B, \\ \ddot{y} &= -\dot{z} \frac{q}{m} B,\end{aligned}\tag{55}$$

with the particle at the origin for  $t=0$ .

The simplest way to begin is to note that by a strong magnetic field we mean (among other things) that  $\omega_b = |q/mB| \gg \omega$ , and here we can consider the electric field to vary slowly in time. This suggests that we consider first the problem with  $\omega = 0$ , the well-known crossed-fields case, but with a uniform electric field gradient.

For  $\dot{z}$  and  $\dot{x}$  both zero at  $t=0$ , the standard solution for a uniform field ( $dE/dz=0$ ) is

$$z = \frac{E}{(q/m)B^2} \left( 1 - \cos \frac{q}{m} Bt \right) = \frac{q}{m} \frac{E}{\omega_b^2} (1 - \cos \omega_b t),\tag{56a}$$

$$y = \frac{E}{B} t - \frac{q}{m} \frac{E}{\omega_b^2} \sin \omega_b t.\tag{56b}$$

Figure 6 shows the motion for a heavy positive and light negative particle. If  $dE/dz \neq 0$  but  $\omega_b^2 > (q/m)(dE/dz)$  then we have, for  $dE/dz = \text{constant}$ ,

$$z = \frac{q}{m} \frac{E}{\omega_b^2} \left[ 1 - \frac{q}{m} \frac{dE}{dz} \frac{1}{\omega_b^2} \right]^{-1} \left[ 1 - \cos \left( \omega_b \left[ 1 - \frac{q}{m} \frac{dE}{dz} \frac{1}{\omega_b^2} \right]^{\frac{1}{2}} t \right) \right]\tag{57a}$$

$$y = \frac{E}{B} t \left[ 1 - \frac{q}{m} \frac{dE}{dz} \frac{1}{\omega_b^2} \right]^{-1} - \left| \frac{q}{m} \right| \frac{E}{\omega_b^2} \left[ 1 - \frac{q}{m} \frac{dE}{dz} \frac{1}{\omega_b^2} \right]^{-3/2} \sin \left( \omega_b \left[ 1 - \frac{q}{m} \frac{dE}{dz} \frac{1}{\omega_b^2} \right]^{1/2} t \right) \quad (57b)$$

and we consider the motion to be drifting ellipses rather than the usual

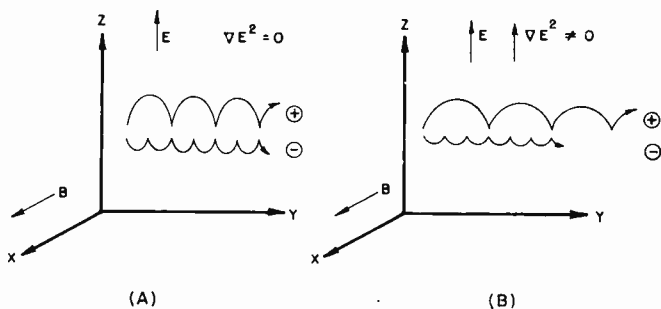


Fig. 6—Single-particle (positive and negative) motions for  $\mathbf{E} \parallel \nabla E^2$  and  $\mathbf{B} \perp \nabla E^2$ , with (A)  $\nabla E^2 = 0$ , (B)  $\nabla E^2 \neq 0$  and d-c electric field.

circles. If we consider  $(q/m)(dE/dz) \ll \omega_b^2$ , i.e.,

$$\frac{1}{\omega^2} \left( \frac{q}{m} \right)^2 \frac{dE^2}{dz} \ll \frac{\omega_b^2}{\omega^2},$$

$$\frac{qE}{m\omega^2}$$

this implies that the fractional drift/cycle in the nonmagnetic case (this drift is taken to be small anyway) is much less than  $\omega_b^2/\omega^2$  which we take to be large by our idea of a strong field. There results, with  $\langle \dot{y} \rangle_{\omega_b}$  meaning time-averaged over  $t = 2\pi/\omega_b$

$$\langle \dot{y} \rangle_{\omega_b} = \frac{E}{B \left( 1 - \frac{q}{m} \frac{dE}{dz} \frac{1}{\omega_b^2} \right)} \approx \frac{E}{B} \left( 1 + \frac{q}{m} \frac{dE}{dz} \frac{1}{\omega_b^2} \right). \quad (58)$$

We now say that

$$E = E \cos \omega t \text{ and } \frac{\partial E}{\partial z} = \frac{\partial E}{\partial z} \cos \omega t$$

(this is the essence of the slowly varying field concept) to give

$$\begin{aligned} \langle \dot{y} \rangle_{\omega} &= \left\langle \frac{E}{B} \cos \omega t \left[ 1 + \left( \frac{q}{m} \frac{dE}{dz} \frac{1}{\omega_b^2} \right) \cos \omega t \right] \right\rangle_{\omega} \\ &= \frac{1}{2} \left( \frac{q}{m} \right) \frac{E}{B \omega_b^2} \frac{dE}{dz} = \frac{1}{4} \frac{q}{|q|} \frac{1}{\omega_b^3} \left( \frac{q}{m} \right)^2 \frac{dE^2}{dz} \quad (59) \\ &= \frac{1}{\frac{q}{m} B} \left( \frac{\omega^2}{\omega_b^2} \right) \frac{1}{4\omega^2} \frac{dE^2}{dz} \end{aligned}$$

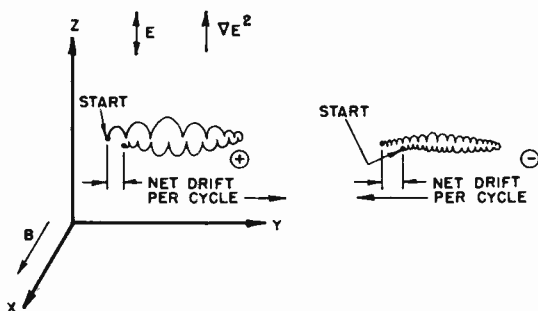


Fig. 7—Single-particle motions (positive and negative) for slow ( $\omega \ll \omega_b$ ) variation in  $E$ , with  $\mathbf{E} \parallel \nabla E^2$  and  $\mathbf{B} \perp \nabla E^2$ .

There is no acceleration, but there is a constant average velocity drift in the  $y$  direction which is in opposite directions for opposite charge signs. The particle motions for a heavy positive and light negative particle are sketched in Figure 7. The reason for the drift is the imbalance between the positive and negative parts of the  $\omega$ -cycle, since the particle travels into stronger fields over one half cycle than the other. Since the imbalance produces motion perpendicular to  $\nabla E^2$  the effect is not cumulative and a steady perpendicular flow is the result. (The situation is like the action of a magnetic field in converting an  $\mathbf{E}$ -directed acceleration into an  $\mathbf{E} \times \mathbf{B}$  drift.)

Thus we see that there is no average force in the  $z$  direction and hence no confinement. As we relax the  $\omega_b^2 \gg \omega^2$  and let  $\omega_b^2 \rightarrow 0$ , we gradually recover the zero magnetic field case with  $z$  acceleration, but the calculations for the intermediate case are quite horrible.

$$\mathbf{E} \perp \nabla E^2$$

For  $\mathbf{B} \parallel \nabla \times \mathbf{E}$  (i.e., parallel to r-f magnetic field) both the d-c and r-f magnetic fields are perpendicular to  $\mathbf{E}$  and  $\nabla E^2$ , and the problem remains two dimensional with all the motion in the  $x$ - $z$  plane.

$$\begin{aligned} \ddot{x} &= \frac{q}{m} \left( E + z \frac{dE}{dz} \right) \cos \omega t - \dot{z} \frac{q}{m} B, \\ \ddot{z} &= -\frac{\dot{x}}{\omega} \frac{q}{m} \frac{dE}{dz} \sin \omega t + \dot{x} \frac{q}{m} B. \end{aligned} \quad (60)$$

This equation is not readily separable because of the mixture of implicit and explicit time-dependent terms, so the only course is to ignore one of the awkward terms (both of them are second-order) at the outset. Ignoring the  $\dot{x} dE/dz$  term gives a periodic  $z$  and  $x$  motion, but ignoring the  $z dE/dz$  term gives a cumulative motion due to  $\dot{x} dE/dz \sin \omega t$ , as in the case with no magnetic field. The calculation for the latter is as follows. Put

$$\begin{aligned} \ddot{x} &= \frac{q}{m} E \cos \omega t - \dot{z} \frac{q}{m} B, \\ \ddot{z} &= -\frac{\dot{x}}{\omega} \frac{q}{m} \frac{dE}{dz} \sin \omega t + \dot{x} \frac{q}{m} B. \end{aligned} \quad (61)$$

Hence

$$\ddot{x} + \omega_b^2 \left( 1 - \frac{1}{\omega} \frac{1}{B} \frac{dE}{dz} \sin \omega t \right) \dot{x} = \frac{q}{m} E \sin \omega t, \quad (62)$$

a Mathieu equation in  $\dot{x}$  with a forcing term. If we assume

$$\frac{1}{\omega} \frac{1}{B} \frac{dE}{dz} = \frac{q}{m} B \frac{1}{\omega^2} \left( \frac{q}{m} \right)^2 \frac{\partial E^2}{\partial z} \ll 1,$$

essentially the same assumption as before, i.e., that  $\omega_b \gg \omega$  and that the gradient field action is considered as a small perturbation, then

$$\dot{x} \approx -\frac{\omega}{\omega_b^2} \frac{q}{m} E \frac{\sin \omega t}{(1 - \omega^2/\omega_b^2)}. \quad (63)$$

Thus

$$\ddot{z} \approx -\frac{\omega}{\omega_b^2(1 - \omega^2/\omega_b^2)} \frac{q}{m} E \sin \omega t \left( \frac{q}{m} B - \frac{q}{m} \frac{dE}{dz} \sin \omega t \right), \quad (64)$$

so

$$\langle \ddot{z} \rangle \approx \frac{1}{4} \left( \frac{\omega^2}{\omega_b^2} \right) \frac{1}{\omega^2} \left( \frac{q}{m} \right)^2 \frac{dE^2}{dz}. \quad (65)$$

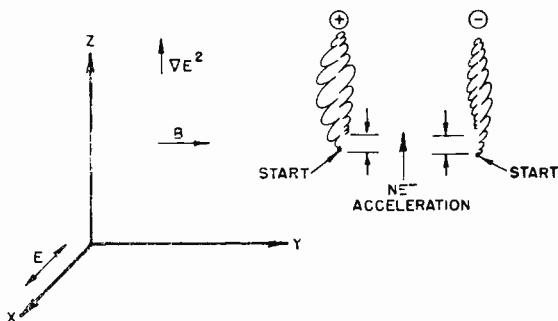


Fig. 8—Single-particle motion for  $\mathbf{E} \perp \nabla E^2$  and  $\mathbf{B} \perp$  (i.e.,  $\mathbf{B}$  parallel to  $\mathbf{B}_{rf}$ ), and  $\omega \ll \omega_b$ .

(We drop the  $\omega^2/\omega_b^2$  term in the denominator which might imply that the solution was applicable when the  $\omega_b \gg \omega$  condition was not fulfilled.) The motion is shown in Figure 8. Thus, for high magnetic field parallel to the r-f magnetic field the perpendicular-gradient-field effect acts in the opposite direction and is reduced by  $\omega^2/\omega_b^2$  from the zero-magnetic-field case. Essentially the high magnetic field reverses the phase of the  $x$ -motion to produce average acceleration in the opposite direction in a manner strongly reminiscent of the space-charge action in the parallel-gradient-field case. The reason is the same; one is considering a system above and below resonance (here  $\omega_b$  rather than  $\omega_p$  is the resonant frequency).

**B||E**

Unlike the  $\mathbf{E}||\nabla E^2$  case, putting the magnetic field parallel to the electric field does produce an effect. One must go to three dimensions and the equations are

$$\begin{aligned}\ddot{x} &= \frac{q}{m} \left( E + z \frac{dE}{dz} \right) \cos \omega t, \\ \ddot{y} &= \frac{q}{m} B, \\ \ddot{z} &= -\frac{\dot{x}}{\omega} \frac{q}{m} \frac{dE}{dz} \sin \omega t - \dot{y} \frac{q}{m} B.\end{aligned}\quad (66)$$

Neglecting the third-order terms in the  $\ddot{x}$  equation gives

$$\ddot{x} = \frac{q}{m} E \cos \omega t, \quad \dot{x} = \frac{1}{\omega} \frac{q}{m} E \sin \omega t, \quad (67)$$

$$\ddot{y} = \ddot{z} \frac{q}{m} B = \frac{q}{m} B \left[ -\frac{\dot{x}}{\omega} \left( \frac{q}{m} \right) \frac{dE}{dz} \sin \omega t - \dot{y} \frac{q}{m} B \right], \quad (68)$$

$$\begin{aligned}\ddot{y} + \omega_b^2 \dot{y} &= -\frac{q}{m} B \frac{1}{c^2} \left( \frac{q}{m} \right)^2 \frac{dE}{dz} \sin^2 \omega t \\ &= -\frac{1}{4} \frac{q}{m} B \frac{1}{c^2} \left( \frac{q}{m} \right)^2 \frac{dE^2}{dz} (1 - \cos 2\omega t).\end{aligned}$$

The particular solution is

$$\dot{y} = \frac{1}{4} \frac{q}{m} B \frac{1}{\omega^2} \left( \frac{q}{m} \right)^2 \frac{dE^2}{dz} \frac{1}{\omega_b^2} \left[ \frac{\cos 2\omega t}{(1 - 4\omega^2/\omega_b^2)} - 1 \right], \quad (69)$$

so that

$$\langle \dot{y} \rangle = -\frac{q}{m} \frac{1}{B} \frac{1}{4\omega^2} \left( \frac{q}{m} \right)^2 \frac{dE^2}{dz}. \quad (70)$$

The  $\dot{z}$  solution proves to be purely periodic. The trajectories are shown in Figure 9. Just as in the magnetic field effect on the  $\mathbf{E}||\nabla E^2$  case, with  $\mathbf{B} \perp \nabla E^2$ , the result is a  $y$ -drift rather than acceleration, in

opposite direction for oppositely charged particles, although the sign of the drift in the reverse of the  $\mathbf{E} \parallel \nabla E^2$  case.\*

$\mathbf{B} \parallel \nabla E^2$

The last case is when the d-c field is parallel to  $\nabla E^2$  and would correspond to a magnetic field parallel to the plasma density gradient.

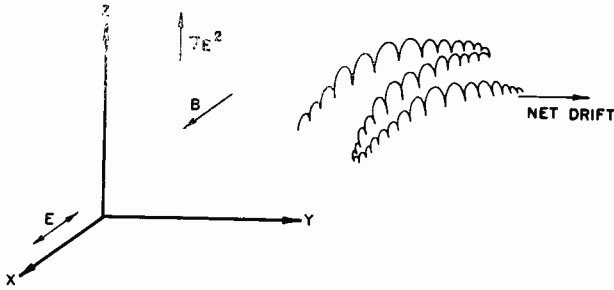


Fig. 9—Single-particle motion  $\mathbf{E} \perp \nabla E^2$ ,  $\mathbf{B} \parallel \mathbf{E}$ ,  $\omega \ll \omega_b$ .

The equations are

$$\begin{aligned} \ddot{x} &= \frac{q}{m} \left( E + \frac{z dE}{dz} \right) \cos \omega t + \dot{y} \frac{q}{m} B, \\ \ddot{y} &= -\dot{x} \frac{q}{m} B, \\ \ddot{z} &= -\dot{x} \frac{1}{\omega} \frac{q}{m} \frac{dE}{dz} \sin \omega t. \end{aligned} \tag{71}$$

As before

$$\ddot{x} + \omega_b^2 \dot{x} = -\omega \frac{q}{m} E \sin \omega t, \tag{72}$$

so

$$\dot{x} = -\frac{\omega}{\omega_b^2} \frac{q}{m} \frac{E \sin \omega t}{1 - \omega^2/\omega_b^2},$$

\* According to Weibel (Second meeting, Plasma Physics Division, American Physical Society, November, 1960) experiments and Vlasov equation calculations indicate that this system can improve theta pinch stability.

and

$$\ddot{z} = \frac{1}{\omega_b^2 - \omega^2} \left( \frac{q}{m} \right)^2 E \frac{dE}{dz} \sin^2 \omega t, \quad (73)$$

$$\langle \ddot{z} \rangle = \left( \frac{\omega}{\omega_b} \right)^2 \frac{1}{4\omega^2} \left( \frac{q}{m} \right)^2 \frac{dE^2}{dz} \frac{1}{1 - (\omega/\omega_b)^2}. \quad (74)$$

This is the same acceleration as for  $\mathbf{B} \parallel \nabla \times \mathbf{E}$  ( $B_{rf}$ ) (Figure 8) but the trajectories are different, as shown in Figure 10.

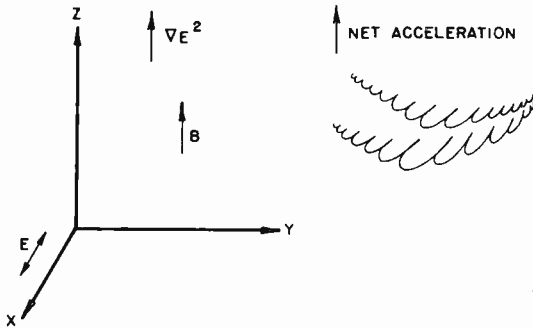


Fig. 10—Single-particle motion  $\mathbf{E} \perp \nabla E^2$ ,  $\mathbf{B} \parallel \nabla E^2$ ,  $\omega \ll \omega_b$ .

The net result of this simplified analysis is that a strong magnetic field will either reverse the acceleration and reduce it by the ratio  $(\omega^2/\omega_b^2)$  or produce a steady flow at right angles to  $\nabla E^2$  in opposite directions for opposite charge signs except for  $\mathbf{B} \parallel \nabla E^2 \parallel \mathbf{E}$ , when the effect is nil.

Now, however, we come to the fly in the ointment. The previous analysis applied to cases where  $\omega_b \gg \omega$ , a condition which is unlikely to hold for ions. Also, the results might be applied only when the particle motion is relatively small compared with the spatial gradients, another condition the ions will violate because of their large Larmor radius (e.g., for a 20-kilovolt deuteron with  $B = 10^5$  gauss, the ion Larmor radius is .23 centimeter).

Hence it seems that, because a relatively full trajectory analysis would be needed, the prospects of deriving an average potential in the sense of Equation (50) are not bright. Even if such a potential could be derived, so that the equilibrium density (neglecting space charge) could be written in terms of the field, the wave equation for

$\mathbf{E}_\perp \nabla n$  no longer has the relatively simple form of Equation (53), but is an equation using the dielectric tensor  $\{\mathbf{K}\}$ , defined for a uniform d-c magnetic field.<sup>31</sup>

$$(\nabla \cdot \nabla) \mathbf{E} + \frac{\epsilon^2}{C^2} \{\mathbf{K}\} \cdot \mathbf{E} = 0, \tag{75}$$

$$[(\nabla \cdot \nabla) \mathbf{E} = - \nabla \times \nabla \times \mathbf{E} + \nabla (\nabla \cdot \mathbf{E})].$$

Unlikely as it seems, this equation can be put into a simple wave equation form for a very special case, considered cursorily by Dow and Knechtli.<sup>28</sup> This simple case is a one-dimensional system with the uniform d-c magnetic field parallel to that dimension and circularly polarized standing waves.

Let us begin by calculating the confinement potential in the sense of Equation (50) and, because we have introduced a longitudinal magnetic field, the derivation of the  $\nabla E^2$  acceleration will have to be altered. Instead of Equation (1) (neglecting losses) we have

$$\ddot{\mathbf{r}} = \frac{q}{m} \mathbf{E}_\perp e^{j\omega t} + \frac{q}{m} \dot{\mathbf{r}} \times (\mathbf{B} + \mathbf{B}_\perp e^{j\omega t}), \tag{76}$$

where  $\mathbf{E}_\perp$  and  $\mathbf{B}_\perp$  are the r-f fields restricted to be perpendicular to  $\mathbf{B}$ , the d-c magnetic field.

As before, the first-order motion is

$$\dot{\mathbf{r}}_\perp = \frac{q}{m} \mathbf{E}_\perp e^{j\omega t} + \frac{q}{m} \dot{\mathbf{r}} \times \mathbf{B}.$$

If we neglect the  $\omega_b$  time variation (since it can give no average effect if  $\omega_b$  and  $\omega$  are incommensurable) we have

$$\left( j\omega + \frac{q}{m} \mathbf{B} \times \right) \dot{\mathbf{r}} = \frac{q}{m} \mathbf{E}_\perp e^{j\omega t}.$$

Operating on both sides with  $(j\omega - (q/m) \mathbf{B} \times)$  gives

$$\dot{\mathbf{r}}_\perp = \frac{\left( j\omega - \frac{q}{m} \mathbf{B} \times \right)}{\omega_b^2 - \omega^2} \frac{q}{m} \mathbf{E}_\perp e^{j\omega t}, \tag{77}$$

where  $\omega_b = |qB/m|$  as before.

The acceleration parallel to  $\mathbf{B}$  is given by

$$\dot{\mathbf{r}}_{\perp} = \frac{q}{m} \dot{\mathbf{r}}_{\perp} \times \mathbf{B}_{\perp} e^{j\omega t} = \left(\frac{q}{m}\right)^2 \left[ \frac{\left(j\omega - \frac{q}{m} \mathbf{B} \times\right)}{\omega_b^2 - \omega^2} \mathbf{E}_{\perp} e^{j\omega t} \right] \times \mathbf{B}_{\perp} e^{j\omega t},$$

$$\langle \dot{\mathbf{r}}_{\parallel} \rangle = \frac{1}{2} \left(\frac{q}{m}\right)^2 \frac{1}{\omega_b^2 - \omega^2} \operatorname{Re} \left[ j\omega \mathbf{E}_{\perp} \times \left(\frac{\nabla \times \mathbf{E}_{\perp}^*}{j\omega}\right) - \left(\frac{q}{m} \mathbf{B} \times \mathbf{E}_{\perp}\right) \times \left(\frac{\nabla \times \mathbf{E}_{\perp}^*}{j\omega}\right) \right]$$

where we have used  $\mathbf{B}_{\perp}^* = \frac{\nabla \times \mathbf{E}_{\perp}^*}{j\omega}$ .

In this case  $(\mathbf{E}_{\perp} \cdot \nabla) \mathbf{E}_{\perp}^* = 0$ , so from Equations (12) and (13)

$$\langle \dot{\mathbf{r}}_{\parallel} \rangle = \frac{1}{2} \left(\frac{q}{m}\right)^2 \frac{1}{\omega_b^2 - \omega^2} \left[ \frac{1}{2} \nabla (\mathbf{E}_{\perp} \cdot \mathbf{E}_{\perp}^*) - \frac{1}{\omega} \frac{q}{m} (\mathbf{B} \times \mathbf{E}_{\perp}) \times (\nabla \times \mathbf{E}_{\perp}^*) \right] \quad (78)$$

For a linearly polarized wave the second term vanishes and we obtain the same result as Equation (74). (This can also be obtained by a suitable combination of right and left circularly polarized modes.)

The interesting cases are the circularly polarized waves, where we can write

$$\mathbf{E}_{\perp} = \frac{E}{\sqrt{2}} (\mathbf{i}_x \mp j\mathbf{i}_y),$$

where the upper sign gives a clockwise rotation of polarization looking along  $\mathbf{B}$  (a wave which will give cyclotron resonance with negative particles) and the lower sign gives counterclockwise (or positive cyclotron) rotation. The root-two factor means that  $|\mathbf{E}_{\perp}| = E$ , a convenience for comparison and computation of energy. Then we have

$$\frac{1}{\omega} \frac{q}{m} \mathbf{B} \times \mathbf{E}_{\perp} = \frac{q}{m} \frac{B}{\omega} \frac{E}{\sqrt{2}} (\mathbf{i}_y \pm j\mathbf{i}_x)$$

and

$$\nabla \times \mathbf{E}_\perp^* = \frac{1}{\sqrt{2}} \frac{\partial E}{\partial z} (\mathbf{i}_y \mp j \mathbf{i}_x).$$

So that for cyclotron waves

$$\langle \ddot{\mathbf{r}} \rangle_\mp = \frac{1}{2} \left( \frac{q}{m} \right)^2 \frac{1}{\omega_b^2 - \omega^2} \left[ \frac{1}{2} \frac{\partial E^2}{\partial z} \mp \frac{q}{m} \cdot \frac{B}{\omega} \cdot \frac{2}{2} E \frac{\partial E}{\partial z} \right].$$

If we note that  $qB/m\omega = \pm \omega_b$  for positive and negative charges, this becomes

$$\langle \ddot{\mathbf{r}} \rangle_+ = -\frac{1}{4} \left( \frac{q}{m} \right)^2 \frac{1}{\omega^2} \frac{1}{1 \pm \omega_b/\omega} \nabla E^2, \tag{78a}$$

(positive particles)

$$\langle \ddot{\mathbf{r}} \rangle_- = -\frac{1}{4} \left( \frac{q}{m} \right)^2 \frac{1}{\omega^2} \frac{1}{1 \mp \omega_b/\omega} \nabla E^2. \tag{78b}$$

(negative particles)

(In passing it should be noted that Dow and Knechtli,<sup>25</sup> in their Appendix B, consider some waves (Equations 2.1(b), (c), 2.2(b) and the counterclockwise, out-of-phase  $\mathbf{E}_\perp$  and  $\mathbf{B}_\perp$ ) which do not satisfy Maxwell's equations. There are in fact, for standing waves, and single particles, only the one linear and two circular modes considered here.)

Let us now write Equations (78a) and (78b) specifically for an electron and a positive ion.

$$\langle \ddot{\mathbf{r}}_e \rangle = -\frac{1}{4} \left( \frac{q}{m} \right)^2 \frac{1}{\omega^2} \frac{1}{1 \mp \omega_b/\omega} \nabla E^2, \tag{79a}$$

$$\langle \ddot{\mathbf{r}}_i \rangle = -\frac{1}{4} \left( \frac{q}{M} \right)^2 \frac{1}{\omega^2} \frac{1}{1 \pm \Omega_b/\omega} \nabla E^2, \tag{79b}$$

where  $\Omega_b = |eB/M|$  and  $\omega_b = |eB/m|$  for ions and electrons, respectively.

If we follow the reasoning of Equations (49) to (51) with this  $\nabla E^2$  effect, neglecting, as before, the direct  $\nabla E^2$  effect on the ions as being of order  $m/M$ , we have

$$n_c \approx n_i \approx n_0 \exp \left( - \frac{e^2 (E^2 - E_M^2)}{8\omega^2 m k T} \frac{1}{1 \pm \omega_b/\omega} \right). \quad (80)$$

With a standing-wave system in which  $E = 0$  at the density maxima (field nodes), we take  $E_M^2 = 0$ ,

$$\omega_{pM}^2 = \frac{n_M e^2}{\epsilon_0 m},$$

where  $n_M$  is the maximum density (which is at the nodes).

$$\frac{n}{n_M} = \exp \left( - \frac{\omega_{pM}^2}{\omega^2} \frac{1}{1 \mp \omega_b/\omega} \frac{\epsilon_0 E^2}{8n_M k T} \right). \quad (81)$$

Now it can be readily shown<sup>31</sup> that the wave Equation (75) of a circularity polarized wave propagating parallel to the magnetic field reduces to

$$\frac{\partial^2 E}{\partial z^2} + \frac{\omega^2}{C^2} \left[ 1 - \frac{\omega_p^2}{\omega^2} \frac{1}{1 \mp \omega_b/\omega} \right] E = 0,$$

where  $\omega_p = ne^2/(\epsilon_0 m)$  corresponding to the local density. Substituting Equation (81) this becomes

$$\frac{\partial^2 E}{\partial z^2} + \frac{\omega^2}{C^2} \left[ 1 - \frac{\omega_{pM}^2}{\omega^2} \frac{1}{1 \mp \omega_b/\omega} \exp \left( \frac{-\omega_{pM}^2}{\omega^2} \frac{1}{1 \mp \omega_b/\omega} \frac{\epsilon_0 E^2}{8n_M k T} \right) \right] E = 0. \quad (82)$$

Now, for  $\omega_b > \omega$ , which will be the case for interesting frequencies and fields, the upper (electron cyclotron) sign gives an effect which concentrates the particles at field maxima, and furthermore for  $\omega_b > \omega$  the dielectric coefficient is always positive, thus sharp gradients will not be produced. Hence the useful mode to consider is the lower sign corresponding to the counterclockwise or ion cyclotron wave. For this wave

$$\frac{\partial^2 E_i}{\partial z^2} + \frac{\omega^2}{C^2} \left[ 1 - \frac{\omega_{pM}^2}{\omega^2} \frac{1}{1 + \omega_b/\omega} \exp \left( \frac{-\omega_{pM}^2}{\omega^2} \frac{1}{1 + \omega_b/\omega} \frac{\epsilon_0 E^2}{8n_M k T} \right) \right] E_i = 0, \quad (83)$$

where here the subscript on  $E$  reminds us that it is the ion wave we consider.

The interesting point is that this is just Equation (53a) all over again (in one dimension) with  $\omega_{pM}^2/\omega^2$  replaced by  $(\omega_{pM}^2/\omega^2)/(1 + \omega_b/\omega)$ ; the numerical solutions obtained by quadratures<sup>19,28</sup> for Equation (53a) can be applied directly and Figure 5 referred to, with the appropriate change of variable. As before for sharp boundaries we must have

$$\frac{\omega_{pM}^2}{\omega^2} \frac{1}{1 + \omega_b/\omega} \gg 1.$$

For  $\omega_b/\omega \gg 1$  the circularly polarized ion wave in the magnetic field case is a factor  $\omega/\omega_b$  less effective in confinement than for  $\omega_b = 0$ , but  $\omega_b/\omega$  better than the linear case for  $\omega_b/\omega \gg 0$ . Actually the superposition, valid for the single particle, would lead to two coupled wave equations with generally incommensurable periods so that the total linear wave solution would be only quasi-periodic.

More complicated geometries are not considered here since we cannot neglect charge separation ( $\nabla \cdot \mathbf{E} \neq 0$ ) and neither the confinement potential nor the wave equation are tractable.

General conclusions from trajectory analysis and potentials may prove incorrect if not checked against actual wave equation solutions. As an example of this, it is easy to deduce from the elementary dipole model of a dielectric (equivalent to  $\omega$  much less than resonance) that the body force should be towards strong fields even at ordinary radio frequencies. Yet from radiation pressure arguments one knows that there is a surface pressure (which is usually much more than the total body force) in the reverse direction to account for the momentum of the reflected wave. (The answer to the paradox is that the surface effects in the transition region have to be included.) Perhaps the interest in time-average acceleration effects in plasmas will also pave the way to a better understanding of all forces in dielectrics (not just the surface layer) a subject whose study seems often to have produced more heat than light.

#### EXPERIMENTAL AND PRACTICAL CONSIDERATIONS

While theoreticians have been busy thinking of fusion applications, some experimental work and analysis have been done.

Boot<sup>1</sup> (but see also Weibel<sup>5</sup>) and Dow<sup>25</sup> have analyzed the skin effect losses, which seem to be high. The general impression is that,

apart from other difficulties, skin effect alone will probably preclude large-scale r-f confinement of very hot (thermonuclear) plasmas, but that critical regions may be plugged with r-f field systems. Confinement of cooler plasmas should not encounter skin-effect problems.

The primary low-frequency limit is the small-signal concept used in the analysis<sup>5</sup> (see discussion following Equation (53a)). Another effect considered by Dow<sup>25</sup> is the outward ambipolar flow of the plasma as the field goes through zero. If the frequency is too low, a considerable loss of plasma may occur while the field is nearly zero.

Essentially, it can be stated that the loss is small when

$$\left( \frac{l/\lambda}{V_{ion}/C} \right)^2 \gg 1 \quad \text{or} \quad \left( \frac{fl}{V_{ion}} \right)^2 \gg 1,$$

where  $l$  is a characteristic apparatus dimension,  $\lambda$  the free-space r-f wavelength, and  $f$  the frequency,  $C$  is the velocity of light and  $V_{ion}$  is the average thermal velocity of the ions. For a system size comparable with the wavelength, then the limitation is that the plasma be nonrelativistic (which has been assumed already), so the limit can only be important if the system is small compared with the wavelength.

One elegant and relatively inexpensive experiment has been carried on by Butler *et al*<sup>9</sup> at the Argonne National Laboratory. This consists essentially of suspending an easily deformable conductor representing the nearly spherical plasma in a cavity, measuring the resonant frequency, and then making a deformation in the conductor and measuring the resonant frequency again. It can be readily shown that the field in an enclosure acts to reduce the resonant frequency since radiation pressure expands a cavity and so lowers the resonant frequency. Hence if a deformation lowers the resonant frequency the deformation can be said to be one which the field assists, and, of course, vice versa. In this way a physical relaxation can be carried out to find the sort of shape a plasma will take on due to the gradient field. Two points arise. The first is that the modes must be such that  $E$  is never normal to the boundary, i.e., only tangential  $E$  ( $E \approx 0$  at the plasma boundary itself) are permitted since otherwise the  $\mathbf{E} \parallel \nabla E^2$  analysis applies and the field would pull the plasma apart. The second is that plasma reflection is not exactly the same as conductor (viscous) reflection. Furthermore, d-c magnetic-field effects cannot be included.

The effects on electrons alone have been demonstrated by ejecting or preventing the entry of electrons into high power cavities and by a curious magnetron effect.<sup>2</sup> More-direct plasma experiments consist essentially of allowing a discharge to partly fill a cavity, increasing

the cavity power and studying the mechanism of the plasma either by its detuning effect<sup>16</sup> or by direct probe measurements. (See also Ref. (3)). Definite results have not been published yet, beyond the bare fact that r-f power in the cavity tends to exclude the plasma, with no reference to d-c magnetic field.<sup>16</sup> Evidently, numerical checks with theory, without a d-c magnetic field, followed by experiments with a magnetic field would be most desirable.

#### ERRORS IN NORMAL-FIELD ANALYSES

In connection with containment in a system with a normal field (e.g.,  $TM_{011}$  mode,  $\mathbf{E} \cdot \nabla n \neq 0$  and  $\mathbf{E} \cdot \nabla E^2 \neq 0$ ) Hall<sup>22</sup> and Dow<sup>25</sup> have produced a conclusion which is exactly opposite to the correct one. The correct result, as shown above, is that for  $\mathbf{E} \parallel \nabla E^2$  confinement is produced for  $\omega_p^2 < \omega^2$  and dispersion for  $\omega_p^2 > \omega^2$ . The opposite conclusion results first, at low densities, from an incorrect assumption that because a sharp plasma boundary will not be produced at low density, there is no confinement. There is confinement, but the density variation is gradual and can be approximately calculated at very low densities ( $\omega_p^2 \ll \omega^2$ ) by neglecting the dielectric and charge effects and using  $\nabla E^2$  equilibrium equation and the original unmodified field distribution rather than Equation (52). At densities where the  $\omega_p^2 \ll \omega^2$  condition does not hold, the problem becomes complicated, but at  $\omega_p^2 > \omega^2$  the charge-separation effects due to the radial field result in dispersion rather than confinement of the plasma. The wrong high-density effect results from using the continuity of radial field and the usual plasma dielectric coefficient. This zero surface charge argument cannot be used for a field component which produces noticeable charge-separation effects, which is the case for  $\omega_p^2 > \omega^2$  and  $\mathbf{E} \parallel \nabla n$ , and in any case the dielectric coefficient only applies when  $\mathbf{E} \perp \nabla n$ , which is not the case here. For a sharp slab this normal field penetrates to the approximate charge separation and distance given roughly by

$$\delta = \frac{\epsilon_0 E}{en_e} = \frac{e}{m} \frac{E}{\omega_p^2} = 1.76 \times 10^{11} E / \omega_p^2 \text{ meters (mks units),}$$

rather than to the "skin depth"  $C/\omega_p$  (a concept applicable when  $\mathbf{E} \perp \nabla n$ ).

#### CONCLUSIONS

The main points can be summarized as follows. When there is no d-c magnetic field the gradient field phenomenon is a direct result of

the second-order motion of charged particles in a standing-wave system and tends to concentrate the particles at field minima. When plasma rather than single particles are considered, the gradient field concept can be used directly, together with the thermodynamic equilibrium state equation and Maxwell's equations, provided the electric field is everywhere perpendicular to  $\nabla n$  (and  $\nabla E^2$ ), and hence results from the r-f Lorentz force. When there is an electric field parallel to the density gradient, it acts to confine or disperse the plasma as frequency is above or below the local plasma frequency. For very low

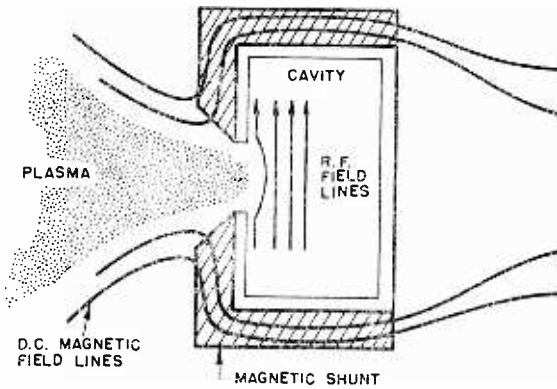


Fig. 11—Possible use of magnetic shield with r-f confinement.

plasma densities ( $\omega_p^2 \ll \omega^2$ ) the alteration of the field by the plasma can be ignored and the solution calculated directly from the field configuration without a plasma. For plasma densities somewhat less than the critical density, the equations for the mixed-system equilibrium are complicated, and for high plasma densities there is confinement only for the pure perpendicular ( $E \perp \nabla n$ ,  $E \perp \nabla E^2$ ) systems. For the pure perpendicular system the motion of radiation pressure gives a good idea of the results.

The qualitative experimental results so far obtained tend to confirm these ideas, but detailed and numerical results have not been published.

More analysis should be devoted to the  $\nabla E^2$  systems with modest values of d-c magnetic field, which, if strong ( $\omega_p^2 > \omega^2$ ) is expected to reduce the r-f confinement action. If this effect is as serious as expected from simple electron arguments, the gradient-field confinement will only prove useful in reducing the leak rate from critical (e.g., cusp) regions in fusion plasma systems when the d-c magnetic field is  $\parallel \nabla E^2$ . Even then the magnetic field may have to be reduced to a tolerable level in the r-f field region (see Figure 11). In any case

the gradient field effect should still be quite useful in controlling diffusion in medium- and low-energy systems<sup>3</sup> without resorting to d-c magnetic fields.

It should be emphasized that the treatment given here assumes the plasma particles to move short distances in an r-f period due to their random velocity. When this assumption cannot be used, the Vlasov or Boltzmann equation should be employed.

#### ACKNOWLEDGMENTS

It is a pleasure to thank G. A. Swartz, H. W. Lorber, and M. Glicksman of RCA Laboratories, Princeton, N. J. for interesting discussions and to acknowledge the support of RCA Astro-Electronics Division for some of the early analysis. (Some of the RCA experimental work has recently appeared in the literature.<sup>34-36</sup>)

#### APPENDIX -- SIMPLIFIED MICROSCOPIC CONCEPTION OF RADIATION PRESSURE

Few, if any, texts give a simple microscopic (i.e., particle) exposition of radiation pressure although the other dielectric and conductor effects are usually explained in this way (see, for instance, Jenkins and White,<sup>33</sup> pp. 476, 569).

For conductors, the main point to note is that it is the viscous ( $\nu$ ) term which dominates at radio-frequencies (for silver,  $\nu \approx 2.74 \times 10^{13}$  cps) so that it is the drag effect which drives the free electrons deeper into the metal and the space-charge coupling with the uncovered positive charge which pulls the solid metal after the electrons. One must exercise care in applying this picture to known solutions such as waveguides, and realize that while no  $E$  tangent to the surface appears, because of the assumption of "infinite" conductivity, there is such a component; it need not be calculated since we are only interested in the viscous current flow, which can be obtained from induction as  $\mathbf{J} = \mathbf{i}_n \times \mathbf{H}$ , where  $\mathbf{i}_n$  is a unit vector normal to the surface. Then the average force on each electron is

$$\langle \mathbf{f}_c \rangle = \frac{1}{2} \frac{\mathbf{J} \cdot \mathbf{J}^*}{(ne)^2} \cdot \frac{\nu}{\omega} \frac{1}{2} \frac{\partial \theta_r}{\partial x_n} \mathbf{i}_n = \frac{1}{2} \mathbf{v} \cdot \mathbf{v}^* \frac{\nu}{\omega} \frac{d\theta_r}{dx_n} \mathbf{i}_n,$$

where the  $\partial \theta_r / \partial x_n$  is calculated from a consistent-field or a potential formulation which also gives  $n_c$  as a function of  $x_n$ . In near-perfect conducting guides and cavities, the other effect,  $\nabla E_n^2$  (which acts

inward), is very small indeed, since  $\nabla E_n^2$  approaches zero as the boundary conductivity tends to infinity.

In low-loss dielectrics the electrons are bound, hence the problem of collective space charge does not arise and the problem then becomes one of dealing with a surface layer which is responsible for the radiation pressure on the dielectric; bulk effects may come from standing waves.

In absorbers, the viscous term is dominant but, unlike a conductor, the material is more or less matched to free space. This may involve many artifices such as quarter-wave absorbing plates, roughness (i.e., multiple scattering) effects etc., but the basic ideas remain the same. Hence the effects of radiation pressure and gradient field which have been discussed for plasmas really apply generally to radio-wave radiation pressure on materials with free electrons. For higher frequencies, of course, this simple picture breaks down and one enters the domain of atomic physics and quantum mechanics.

#### References

<sup>1</sup> H. A. H. Boot, S. A. Self, and R. B. R-Shersby-Harvie, "Containment of a Fully-Ionized Plasma by Radio-Frequency Fields," *Journal of Electronics and Control*, Vol. 4, p. 434, May, 1958.

<sup>2</sup> H. A. H. Boot and R. B. R.-S.-Harvie, "Charged Particles in a Non-Uniform Radio-Frequency Field," *Nature*, Vol. 180, p. 1187, November 30, 1957.

<sup>3</sup> S. A. Self and H. A. H. Boot, "The Effect of Field Configuration on Gas Discharge Breakdown in Microwave Cavities at Low Pressure," *Journal of Electronics and Control*, Vol. 6, p. 527, June, 1959.

<sup>4</sup> E. S. Weibel, *The Plasma in a Magnetic Field*, (ed. R. Landshoff) Stanford Univ. Press, Stanford, Calif., 1958.

<sup>5</sup> E. S. Weibel, "A Note on the Confinement of a Plasma by R. F. Fields," *Journal of Electronics and Control*, Vol. 5, p. 435, November, 1958.

<sup>6</sup> E. S. Weibel, "On the Confinement of a Plasma by Magnetostatic Fields," *Physics of Fluids*, Vol. 2, p. 52, January-February, 1959.

<sup>7</sup> M. U. Clauser and E. S. Weibel, "Radiation Pressure Confinement, The Shock Pinch and Feasibility of Fusion Propulsion," *Proceedings of the Second United Nations International Conference on the Peaceful Uses of Atomic Energy*, Vol. 32, p. 161 (Paper 1774 USA), United Nations, Geneva, 1958.

<sup>8</sup> F. B. Knox, "A Method of Heating Matter of Low Density to Temperatures in the Range  $10^5$  to  $10^{10}$  K," *Aust. Jour. Phys.*, Vol. 10, p. 565, 1957.

<sup>9</sup> J. W. Butler, A. J. Hatch, and A. J. Ulrich, "Radio-Frequency Thermonuclear Machines," *Proceedings of the Second United Nations International Conference on the Peaceful Uses of Atomic Energy*, Vol. 32, p. 324 (Paper 350 USA), United Nations, Geneva, 1958.

- <sup>10</sup> A. V. Gaponov and M. A. Miller, "Potential Wells for Charged Particles in a High-Frequency Electromagnetic Field," *Soviet Physics JETP*, Vol. 7, p. 168, July, 1958 (*ZETF*, Vol. 34, p. 242, January, 1958).
- <sup>11</sup> A. V. Gaponov and M. A. Miller, "Use of Moving High-Frequency Potential Wells for the Acceleration of Charged Particles," *Soviet Physics JETP*, Vol. 7, p. 515, September, 1958 (*ZETF*, Vol. 34, p. 751, March, 1958).
- <sup>12</sup> M. A. Miller, "Reflection of Electrons from a High-Frequency Potential Barrier," *Soviet Physics JETP*, Vol. 8, p. 206, January, 1959 (*ZETF*, Vol. 35, p. 299, July, 1958).
- <sup>13</sup> M. A. Miller, "Several Possibilities Associated with the Separation of Charged Particles in an Inhomogeneous High-Frequency Electromagnetic Field," *Soviet Physics JETP*, Vol. 8, p. 561, March, 1959 (*ZETF*, Vol. 35, p. 809, September, 1958).
- <sup>14</sup> G. V. Gordeev and A. I. Gubanov, "Acceleration of a Plasma in a Magnetic Field," *Soviet Physics, Technical Physics, ZTF*, Vol. 3, p. 1880, September, 1958.
- <sup>15</sup> B. B. Kadomtsev and S. I. Braginsky, "Stabilization of Plasma by Nonuniform Magnetic Fields," *Proceedings of the Second United Nations International Conference on the Peaceful Uses of Atomic Energy*, Vol. 32, p. 233 (Paper 2212 USSR), United Nations, Geneva, 1958.
- <sup>16</sup> A. A. Vedenov and five others, "Thermal Insulation and Confinement of Plasma with a High-Frequency Electromagnetic Field," *Proceedings of the Second United Nations International Conference on the Peaceful Uses of Atomic Energy*, Vol. 32, p. 239 (Paper 2501 USSR), United Nations, Geneva, 1958.
- <sup>17</sup> G. A. Askar'yan, "Acceleration of Charged Particles in Running or Standing Electromagnetic Waves," *Soviet Physics JETP*, Vol. 9, p. 430, August, 1959 (*ZETF*, Vol. 36, p. 619, February, 1959).
- <sup>18</sup> V. V. Yankov, *Soviet Physics JETP*, Vol. 10, p. 158 (*ZETF*, Vol. 37, p. 224, 1960-59); "Behavior of a Conducting Gaseous Sphere in a Quasi-Stationary Electromagnetic Field," *Soviet Physics JETP*, Vol. 9, p. 388, August, 1959 (*ZETF*, Vol. 36, p. 560, February, 1959).
- <sup>19</sup> V. Cushing and M. S. Sodha, "Confinement of Plasma by Standing Electromagnetic Wave," *Physics of Fluids*, Vol. 2, p. 494, September-October, 1959; Errata, Vol. 3, p. 142, January-February, 1960.
- <sup>20</sup> C. M. Haaland, "Confinement of Charged Particles by Plane Electromagnetic Waves in Free Space," *Phys. Rev. Letters*, Vol. 4, p. 111, February 1, 1960.
- <sup>21</sup> R. F. Wuerker, H. Shelton, and R. V. Langmuir, "Electrodynamic Containment of Charged Particles," *Jour. Appl. Phys.*, Vol. 30, p. 342; R. F. Wuerker, H. M. Goldenberg, and R. V. Langmuir, "Electrodynamic Containment of Charged Particles by Three-Phase Voltages," p. 441, March, 1959.
- <sup>22</sup> R. B. Hall, "Electromagnetic Containment of Charged Particles," *MIT Quarterly Progress Report* 51, p. 10, October 15, 1958.
- <sup>23</sup> R. B. Hall, "A Limitation of RF Confinement," *MIT Quarterly Progress Report* 54, p. 31, July 15, 1959.
- <sup>24</sup> C. K. Birdsall and A. J. Lichtenberg, "Traveling Wave Focusing for Plasma Containment," *Phys. Rev. Letters*, Vol. 3, p. 163, August 15, 1959.

<sup>25</sup> D. G. Dow and R. C. Knechtli, "Plasma Containment by r.f. and d.c. Field Combinations," *Journal of Electronics and Control*, Vol. 7, p. 316, October, 1959 (Hughes Res. Rep. 123).

<sup>26</sup> J. W. Butler, "Stability of Electromagnetic Plasma Confinement in Spherical Geometry," *Proceedings of the Fourth International Conference on Ionization Phenomena in Gases*, Vol. 2, p. 620, North-Holland Publishing Co., Amsterdam, 1960.

<sup>27</sup> S. A. Self, "Comments on 'Confinement of Plasma by Standing Electromagnetic Wave,'" *Physics of Fluids*, Vol. 3, p. 488, May-June, 1960.

<sup>28</sup> S. A. Self, "Plasma Containment in One Dimension by a Plane-Polarized Wave," *S.E.R.L. Tech. Memo.* 393, 1958.

<sup>29</sup> H. A. Pohl, "Some Effects of Nonuniform Fields on Dielectrics," *Jour. Appl. Phys.*, Vol. 29, p. 1182, August, 1958.

<sup>30</sup> N. W. McLachlan, *Theory and Application of Mathieu Functions*, Oxford Univ. Press, London, 1951.

<sup>31</sup> M. P. Bachynski, I. P. Shkarofsky, and T. W. Johnston, *Plasmas and the Electromagnetic Field*, McGraw-Hill Book Co., New York, N. Y. (in press).

<sup>32</sup> G. Toraldo di Francia, *Electromagnetic Waves*, (esp. introduction) Interscience Publishers, Inc., New York, N. Y., 1955.

<sup>33</sup> F. Jenkins, H. White, *Fundamentals of Optics*, McGraw-Hill Inc., New York, N. Y., 1950.

<sup>34</sup> G. D. Gordon, "Plasma Acceleration in an R-F Field Gradient — Theory," *Bull. Amer. Phys. Soc.*, Vol. 5, p. 350, 1960.

<sup>35</sup> H. W. Lorber and T. T. Reboul, "Plasma Acceleration in an R-F Field Gradient — Experimental," *Bull. Amer. Phys. Soc.*, Vol. 5, p. 351, 1960.

<sup>36</sup> G. A. Swartz, T. T. Reboul, G. D. Gordon, and H. W. Lorber, "Plasma Acceleration in an R-F Field Gradient," *Physics of Fluids*, Vol. 3, pp. 973-976, 1960.

# RCA TECHNICAL PAPERS†

Third Quarter, 1960

Any request for copies of papers listed herein should be addressed to the publication to which credited.

"Absolutely Stable Hybrid Coupled Tunnel-Diode Amplifier," J. J. Sie, <i>Proc. I.R.E.</i> (July) (Correspondence) .....	1960
"Calculating Bandwidths for Matching Networks," H. B. Yin, <i>Electronic Industries</i> (July) .....	1960
"Circuit to Plot the Temperature Dependence of the Dielectric Constant $\epsilon$ and the Inverse Dielectric Constant $1/\epsilon$ ," H. Roetschi, <i>Rev. Sci. Instr.</i> (July) (Notes) .....	1960
"A Developmental Tricolor Vidicon Having a Multiple-Electrode Target," P. K. Weimer, S. Gray, C. W. Beadle, H. Borkan, S. A. Ochs, and H. C. Thompson, <i>Trans. I.R.E. PGED</i> (July) .....	1960
"The Effect of Parasitic Diode Elements on Traveling-Wave Parametric Amplification," D. Fleri and J. Sie, <i>Proc. I.R.E.</i> (July) (Correspondence) .....	1960
"Lightweight Very-Wide-Band Integral Package TWT'S," C. L. Cuccia, <i>Microwave Jour.</i> (July) .....	1960
"A Method for Broad-Banding Synchronism in Traveling-Wave Parametric Devices," H. Boyet and D. Fleri, <i>Proc. I.R.E.</i> (July) (Correspondence) .....	1960
"Millimeter Wave Generation by Parametric Methods," G. H. Heilmeier, <i>Proc. I.R.E.</i> (July) (Correspondence) .....	1960
"A New Digital Computer System for Commercial Data Processing," J. A. Brustman, <i>Trans. I.R.E. PGIE</i> (July) .....	1960
"New Helix-Support Method for Traveling-Wave Tubes," D. J. Blattner and F. E. Vaccaro, <i>Trans. I.R.E. PGED</i> (July) .....	1960
"A Parametric Subharmonic Oscillator Pumped at 34.3 KMC," A. H. Solomon and F. Sterzer, <i>Proc. I.R.E.</i> (July) (Correspondence) .....	1960
"Saturation of Photocurrent with Light Intensity," R. H. Bube, <i>Jour. Appl. Phys.</i> (July) (Letters to the Editor) .....	1960
"Single-Diode Parametric Up-Converter with Large Gain-Bandwidth Product," R. Pettai, B. Bossard, and S. Weisbaum, <i>Proc. I.R.E.</i> (July) (Correspondence) .....	1960
"Skin Effect in Semiconductors," A. H. Frei and Coauthor, <i>Proc. I.R.E.</i> (July) .....	1960
"A Small-Signal Field Theory Analysis of Crossed-Field Amplifiers Applicable to Thick Beams," B. Hershenov, <i>Trans. I.R.E. PGED</i> (July) .....	1960
"Superconducting Contacts," J. I. Pankove, <i>Trans. I.R.E. PGED</i> (July) .....	1960
"Transient Behavior of Aperture Antennas," C. Polk, <i>Proc. I.R.E.</i> (July) .....	1960
"Portable Radio Uses Drift-Field Transistors," R. A. Santilli and H. Thanos, <i>Electronics</i> (July 8) .....	1960
"Automatic Test Equipment Checks Missile Systems," D. B. Dobson and L. L. Wolff, <i>Electronics</i> (July 15) .....	1960
"GaAs Reactance Generates Millimeter Waves," G. H. Heilmeier, <i>Electronics</i> (July 15) .....	1960
"Photoemission from Si Induced by an Internal Electric Field," R. E. Simon and W. E. Spicer, <i>Phys. Rev.</i> (July 15) .....	1960

† Report all corrections or additions to RCA Review, RCA Laboratories, Princeton, N. J.

- "The Compatibility Problem in Single-Sideband Transmission," K. H. Powers, *Proc. I.R.E.* (August) ..... 1960
- "Directional Antennas for Television Broadcasting," G. H. Brown, *Trans. I.R.E. PGB* (August) ..... 1960
- "Field Induced Photoemission and Hot-Electron Emission from Germanium," R. E. Simon and W. E. Spicer, *Jour. Appl. Phys.* (August) (Letters to the Editor) ..... 1960
- "New Triode-Pentode for Hi-Fi," W. Austin, *Electronics World* (August) (Letters from Our Readers) ..... 1960
- "The Reflected-Beam Kinescope," H. B. Law and E. G. Ramberg, *Proc. I.R.E.* (August) ..... 1960
- "Remote Control of TV Microwave Equipment," J. B. Bullock, *Trans. I.R.E. PGB* (August) ..... 1960
- "The Reversal of the Spontaneous Polarization in Guanidine Aluminium Sulfate Hexahydrate," E. Fatuzzo, *Helvetica Physica Acta* (August) ..... 1960
- "A Special Effects Amplifier for Non-Composite or Composite, Monochrome or Color Television Signals," R. C. Kennedy, *Trans. I.R.E. PGB* (August) ..... 1960
- "The System Iridium-Tellurium," E. F. Hockings and J. G. White, *Jour. Phys. Chem.* (August) ..... 1960
- "Paramagnetic Resonance of  $V^{4+}$  in  $TiO_2$ ," H. J. Gerritsen and H. R. Lewis, *Phys. Rev.* (August 1) ..... 1960
- "Design of Mobile Receivers with Low-Plate-Potential Tubes," C. Gonzalez and R. J. Nelson, *Electronics* (August 19) ..... 1960
- "Apparatus for the Measurement of the Thermal Diffusivity of Solids at High Temperatures," B. Abeles, G. D. Cody, and D. S. Beers, *Jour. Appl. Phys.* (September) ..... 1960
- "Chromium-Doped Titania as a Maser Material," H. J. Gerritsen, S. E. Harrison, and H. R. Lewis, *Jour. Appl. Phys.* (September) ..... 1960
- "A Compatible Stereophonic System for the AM Broadcast Band," J. Avins, L. A. Freedman, F. R. Holt, J. H. O'Connell, J. O. Preisig, and R. N. Rhodes, *RCA Review* (September) ..... 1960
- "A Description of the Tunnel Diode and its Applications," J. W. Wentworth, *Trans. I.R.E. PGB* (September) ..... 1960
- "Design Consideration for Grid-Controlled Electron Guns for Pulsed Traveling-Wave Tubes," H. J. Wolkstein, *RCA Review* (September) ..... 1960
- "The Design of Varactor Diodes," J. Hilibrand and C. F. Stocker, *RCA Review* (September) ..... 1960
- "Determination of the Capacitance, Inductance, and Characteristic Impedance of Rectangular Lines," T. S. Chen, *Trans. I.R.E. PGMTT* (September) ..... 1960
- "Evaluation and Control of Diffused Impurity Layers in Germanium," H. S. Veloric and W. J. Greig, *RCA Review* (September) ..... 1960
- "Evaluation of Aircraft Steering Displays," A. Z. Weisz, J. I. Elkind, B. C. Pierstorff, and L. T. Sprauge, *Trans. I.R.E. PGHFE* (September) ..... 1960
- "The Magnetic Field and Flux Distributions in a Periodic Focusing Stack for Traveling-Wave Tubes," M. J. Schindler, *RCA Review* (September) ..... 1960
- "Mathematical and Experimental Studies of a Wide-Band Vertically Polarized Antenna," P. Foldes, *Trans. I.R.E. PGAP* (September) ..... 1960
- "A Note of Caution on the Square-Law Approximation to an Optimum Detector," J. J. Buszgang and W. L. Mudgett, *Trans. I.R.E. PGIT* (September) (Correspondence) ..... 1960
- "The Oscillistor—New Type of Semiconductor Oscillator," R. D. Larrabee and M. C. Steele, *Jour. Appl. Phys.* (September) .. 1960

"Photovoltaic Effect Derived from the Carnot Cycle," A. Rose, <i>Jour. Appl. Phys.</i> (September) .....	1960
"Radio Relaying by Reflection from the Sun," D. J. Blattner, <i>Trans. I.R.E. PGCS</i> (September) .....	1960
"The Reliability of Transistors in Battery Portable Radio Receivers," R. M. Cohen, <i>Trans. I.R.E. PGRC</i> (September) .....	1960
"Slow-Wave Structures for Electrostatically Focused High-Power Traveling-Wave Tubes," E. F. Belohoubek, <i>RCA Review</i> (September) .....	1960
"Space-Charge Effects in Ultra-Low-Noise Electron Guns," J. Berghammer, <i>RCA Review</i> (September) .....	1960
"Thermal Conversion in n-Type GaAs," J. J. Wysocki, <i>Jour. Appl. Phys.</i> (September) (Letters to the Editor) .....	1960
"Transformation of Impedances Having a Negative Real Part and the Stability of Negative Resistance Devices," B. Rosen, <i>Proc. I.R.E.</i> (September) (Correspondence) .....	1960
"A Transistorized Portable Magnetic Film Recording Channel," C. E. Hittle, M. Rettinger, and K. Singer, <i>Jour. S.M.P.T.E.</i> (September) .....	1960
"Vapor Pressure Data for Some Common Gases," R. E. Honig and H. O. Hook, <i>RCA Review</i> (September) .....	1960
"Photoconductivity in Gallium Sulfo-Selenide Solid Solutions," R. H. Bube and E. L. Lind, <i>Phys. Rev.</i> (September 1) .....	1960
"The BMEWS Automatic Monitoring System," E. L. Danheiser and M. Korsen, <i>I.R.E. Wescon Convention Record, Part 6, Air Traffic Control; Military Electronics; Reliability</i> .....	1960
"Fresnel Region Boresight Methods," A. J. Bogush, Jr., <i>I.R.E. Wescon Convention Record, Part 1, Antennas; Microwave Theory and Techniques</i> .....	1960
"A Packaged Micromodule Laboratory for Industry," D. T. Levy, <i>I.R.E. Wescon Convention Record, Part 3, Microminiaturization; Semiconductor Devices and Tubes</i> .....	1960
"Tunnel Diode Microwave Oscillators with Milliwatt Power Outputs," D. E. Nelson and F. Sterzer, <i>I.R.E. Wescon Convention Record, Part 1, Antennas; Microwave Theory and Techniques</i> .....	1960

## AUTHORS



KARL DREYER received the Bachelor of Science degree from the Cooper Union in 1929 and the graduate degree of Chemical Engineer in 1934. He joined RCA at Harrison, N. J. as a receiving-tube development engineer in 1929. During 1944 and 1945, he was assigned to the International Division of RCA on an overseas project. In 1946 he transferred to the Lancaster plant. He is currently Senior Engineer in the Vacuum Engineering Department of the Electron Tube Division at Lancaster. His major assignment is responsibility for engineering the vacuum vessels for both Stage I and Stage II of the

Model C-Stellarator. Mr. Dreyer is a Senior Member of the Institute of Radio Engineers.

ROBERT D. GOLD (See *RCA Review*, Vol. XXI, No. 1, June 1960, p. 294.)

TUDOR W. JOHNSTON received the B.S. degree in engineering physics from McGill University, Montreal, in 1953, and the Ph.D. degree from the University of Cambridge, England, in 1958. While at Trinity College, Cambridge, he investigated the dynamics of magnetically-focused electron beams from magnetically-shielded electron guns, including nonlaminar effects and ion phenomena. He participated in VHF FM relay development at the RCA Victor Company, Ltd., Montreal, and on his return from England, joined the Microwave Laboratory of the RCA Victor Research Laboratories in Montreal. He has collaborated in an analysis of the ion diode rocket and general electrical rocket characteristics, but his chief work is in electron beam and electromagnetic wave interaction with plasmas, and plasma physics in general. Dr. Johnston is a member of Phi Epsilon Alpha.



JOHN T. MARK received the B.S. degree in Electrical Engineering from Valparaiso Technical Institute in 1950. Prior to that time, he had served with the Army Airways Communications System during World War II, and worked for Sylvania Electric Products, Inc., and several radio broadcast stations. He joined the Electron Tube Division of the Radio Corporation of America in Lancaster, Pa., in 1950, and is presently working on the design and construction of the vacuum systems for the Model C-Stellarator. Mr. Mark is a Member of the Institute of Radio Engineers, the IRE Professional

Group on Electron Devices, and the American Vacuum Society.

CHARLES W. MUELLER received the B.S. degree in electrical engineering from the University of Notre Dame in 1934 and the S.M. degree in electrical engineering from the Massachusetts Institute of Technology in 1936. From 1936 to 1938 Dr. Mueller was associated with Raytheon Production Corporation. In the fall of 1938, he returned to the Massachusetts Institute of Technology where he continued his studies and received the degree of Sc.D. in Physics in 1942. While at the Massachusetts Institute of Technology, Dr. Mueller worked on a government contract on the development of gas-filled special-purpose tubes for counting operations. From 1942 to the present he has been a member of the RCA Laboratories where he has been engaged in research on high-frequency receiving tubes, secondary electron emission phenomena, and solid-state devices. Dr. Mueller did the pioneering development that lead to the commercial production of alloy transistors. Dr. Mueller is a Fellow of the Institute of Radio Engineers, a member of the American Physical Society and Sigma Xi. He was the 1946-1947 chairman of the Princeton Section of the I.R.E.



LEON S. NERGAARD received the B.S. degree in Electrical Engineering from the University of Minnesota in 1927, the M.S. degree from Union College in 1930, and the Ph.D. degree from the University of Minnesota in 1935. From 1927 to 1930, he was in the research laboratory and vacuum-tube engineering department of the General Electric Company; from 1930 to 1933 a teaching assistant in the department of physics at the University of Minnesota; from 1933 to 1942 in the research and development laboratory of the RCA Manufacturing Company; and since 1942 at RCA Laboratories in Princeton, N. J.

Dr. Nergaard is a Member of Sigma Xi and the American Association for the Advancement of Science, and a Fellow of the Institute of Radio Engineers and the American Physical Society.

STEFAN A. OCHS obtained the B.S. degree in mechanical engineering from Columbia University in 1943. After serving in the U.S. Army from 1944 to 1946, he did graduate work in physics at Columbia and received the A.M. degree in 1949 and the Ph.D. degree in 1953. From 1950 to 1951 he taught physics at the City College of New York. He received an A.E.C. Pre-doctoral Fellowship for the year 1951-1952. In 1952 he joined RCA Laboratories, where he has been engaged in research on television camera tubes. Dr. Ochs is a member of Sigma Xi and of the Institute of Radio Engineers.



# RCA REVIEW

*a technical journal*

RADIO AND ELECTRONICS  
RESEARCH • ENGINEERING

---

## INDEX

---

VOLUME XXI

---

### TABLE OF CONTENTS

#### March

	PAGE
Simultaneous Signal Separation in the Tricolor Vidicon .....	3
H. BORKAN	
Ringling in Horizontal-Deflection and High-Voltage Television Circuits .....	17
T. MURAKAMI	
The Influence of Magnetic Tape on the Field of a Recording Head ..	45
E. DELLA TORRE	
Nonlinear Theory of a Velocity-Modulated Electron Beam with Finite Diameter .....	53
F. PASCHKE	
A Frequency-Locked Grid-Controlled Magnetron .....	75
C. L. CUCCIA	
Theoretical and Experimental Study of Wide-Band Paraboloid Antenna with Central-Reflector Feed .....	94
P. FOLDES AND S. G. KOMLOS	
Improved Antennas of the Rhombic Class .....	117
E. A. LAPORT AND A. C. VELDHUIS	
Measurement of Semiconductor Properties through Microwave Absorption .....	124
R. D. LARRABEE	
Application of the Sampling Function to Circuit Analysis of Modulators and Demodulators using Diodes .....	130
A. FELLER	

#### June

The Stratoscope I Television System .....	151
L. E. FLORY, G. W. GRAY, J. M. MORGAN, AND W. S. PIKE	

	PAGE
High-Voltage Electron Extraction from an Arc-Discharge Plasma ..	170
K. G. HERNQVIST	
Absolute Spectral Response Characteristics of Photosensitive Devices	184
R. W. ENGSTROM	
A Low-Wattage Planar Cathode .....	191
T. N. CHIN	
Microminiature Multichannel Pulse-Position-Modulation System Incorporating Transistor-Magnetic-Core Circuitry .....	199
H. KIHN, R. J. KLENSCH, AND A. H. SIMON	
Parametric Amplification, Power Control, and Frequency Multiplication at Microwave Frequencies Using Cyclotron-Frequency Devices .....	228
C. L. CUCCIA	
Determination of the Impurity Distribution in Junction Diodes from Capacitance-Voltage Measurements .....	245
J. HILIBRAND AND R. D. GOLD	
Sine-Squared Pulses in Television System Analysis .....	253
R. KENNEDY	
A New Miniature Beam-Deflection Tube .....	266
M. B. KNIGHT	
<b>September</b>	
A Compatible Stereophonic System for the AM Broadcast Band ....	299
J. AVINS, L. A. FREDMAN, F. R. HOLT, J. H. O'CONNELL, J. O. PREISIG AND R. N. RHODES	
Vapor Pressure Data for Some Common Gases .....	360
R. E. HONIG AND H. O. HOOK	
Space-Charge Effects in Ultra-Low-Noise Electron Guns .....	369
J. BERGHAMMER	
Slow-Wave Structures for Electrostatically Focused High-Power Traveling-Wave Tubes .....	377
ERWIN F. BELOHOUBEK	
Design Consideration for Grid-Controlled Electron Guns for Pulsed Traveling-Wave Tubes .....	389
H. J. WOLKSTEIN	
The Magnetic Field and Flux Distributions in a Periodic Focusing Stack for Traveling-Wave Tubes .....	414
MAX J. SCHINDLER	
Evaluation and Control of Diffused Impurity Layers in Germanium ..	437
H. S. VELORIC AND W. J. GREIG	
The Design of Varactor Diodes .....	457
J. HILIBRAND AND C. F. STOCKER	
<b>December</b>	
Amplification—Modern Trends, Techniques and Problems .....	485
L. S. NERGAARD	
The Ultra-High-Vacuum System for the C-Stellarator .....	508
K. DREYER AND J. T. MARK	

	PAGE
High-Frequency Varactor Diodes .....	547
C. W. MUELLER AND R. D. GOLD	
A Plug-Type Image Orthicon Target .....	558
S. A. OCHS	
Time-Averaged Effects on Charged Practicles in A-C Fields .....	570
T. W. JOHNSTON	

## AUTHORS, VOLUME XXI

	ISSUE	PAGE
Avins, J. (Coauthor)—“A Compatible Stereophonic System for the AM Broadcast Band” .....	Sept.	299
Belohoubek, E. F.—“Slow-Wave Structures for Electrostatically Focused High-Power Traveling-Wave Tubes” ....	Sept.	377
Berghammer, J.—“Space-Charge Effects in Ultra-Low-Noise Electron Guns” .....	Sept.	369
Borkan, H.—“Simultaneous Signal Separation in the Tricolor Vidicon” .....	Mar.	3
Chin, T. N.—“A Low-Wattage Planar Cathode” .....	June	191
Cuccia, C. L.—“A Frequency-Locked Grid-Controlled Magnetron” .....	Mar.	75
“Parametric Amplification, Power Control, and Frequency Multiplication at Microwave Frequencies Using Cyclotron-Frequency Devices” .....	June	228
Della Torre, E.—“The Influence of Magnetic Tape on the Field of a Recording Head” .....	Mar.	45
Dreyer, K. (Coauthor)—“The Ultra-High-Vacuum System for the C-Stellarator” .....	Dec.	508
Engstrom, R. W.—“Absolute Spectral Response Characteristics of Photosensitive Devices” .....	June	184
Feller, A.—“Application of the Sampling Function to Circuit Analysis of Modulators and Demodulators using Diodes” .....	Mar.	130
Flory, L. E. (Coauthor)—“The Stratoscope I Television System” .....	June	151
Foldes, P. (Coauthor)—“Theoretical and Experimental Study of Wide-Band Paraboloid Antenna with Central-Reflector Feed” .....	Mar.	94
Freedman, L. A. (Coauthor)—“A Compatible Stereophonic System for the AM Broadcast Band” .....	Sept.	299
Gold, R. D. (Coauthor)—“Determination of the Impurity Distribution in Junction Diodes from Capacitance-Voltage Measurements” .....	June	245
(Coauthor)—“High-Frequency Varactor Diodes” .....	Dec.	547
Greig, W. J. (Coauthor)—“Evaluation and Control of Diffused Impurity Layers in Germanium” .....	Sept.	437
Gray, G. W. (Coauthor)—“The Stratoscope I Television System” .....	June	151
Hernqvist, K. G.—“High-Voltage Electron Extraction from an Arc-Discharge Plasma” .....	June	170
Hilibrand, J. (Coauthor)—“The Design of Varactor Diodes” .....	Sept.	457
(Coauthor)—“Determination of the Impurity Distribution in Junction Diodes from Capacitance-Voltage Measurements” .....	June	245